

# Journal of Mechanics of Materials and Structures

Special issue on  
**Peridynamic Theory**

Volume 10, No. 5

December 2015



# JOURNAL OF MECHANICS OF MATERIALS AND STRUCTURES

[msp.org/jomms](http://msp.org/jomms)

Founded by Charles R. Steele and Marie-Louise Steele

## EDITORIAL BOARD

|                 |   |
|-----------------|---|
| ADAIR R. AGUIAR | University of São Paulo at São Carlos, Brazil   |
| KATIA BERTOLDI  | Harvard University, USA                         |
| DAVIDE BIGONI   | University of Trento, Italy                     |
| YIBIN FU        | Keele University, UK                            |
| IWONA JASIUK    | University of Illinois at Urbana-Champaign, USA |
| C. W. LIM       | City University of Hong Kong                    |
| THOMAS J. PENCE | Michigan State University, USA                  |
| DAVID STEIGMANN | University of California at Berkeley, USA       |

## ADVISORY BOARD

|               |   |
|---------------|---|
| J. P. CARTER  | University of Sydney, Australia                 |
| D. H. HODGES  | Georgia Institute of Technology, USA            |
| J. HUTCHINSON | Harvard University, USA                         |
| D. PAMPLONA   | Universidade Católica do Rio de Janeiro, Brazil |
| M. B. RUBIN   | Technion, Haifa, Israel                         |

**PRODUCTION** [production@msp.org](mailto:production@msp.org)

SILVIO LEVY Scientific Editor

Cover photo: Wikimedia Commons

---

See [msp.org/jomms](http://msp.org/jomms) for submission guidelines.


---

JoMMS (ISSN 1559-3959) at Mathematical Sciences Publishers, 798 Evans Hall #6840, c/o University of California, Berkeley, CA 94720-3840, is published in 10 issues a year. The subscription price for 2015 is US\$565/year for the electronic version, and \$725/year (+\$60, if shipping outside the US) for print and electronic. Subscriptions, requests for back issues, and changes of address should be sent to MSP.

---

JoMMS peer-review and production is managed by EditFLOW<sup>®</sup> from Mathematical Sciences Publishers.

PUBLISHED BY

 **mathematical sciences publishers**  
nonprofit scientific publishing

<http://msp.org/>

© 2015 Mathematical Sciences Publishers

## PREFACE

This special issue contains contributions that were invited on the occasion of the Peridynamic Theory symposium held at the 17th U.S. National Congress on Theoretical and Applied Mechanics (USNCTAM) at Michigan State University in June, 2014.

One theme of these papers is exploiting the potential of peridynamics in contemporary technology, particularly by including multiple physical effects and applying it to nanoscale mechanics. The paper by Turner, Val Bloemen Waanders, and Parks develops an inverse method to determine heterogeneous nonlocal material properties from experimental data, including digital image correlation (DIC). Wildman and Gazonas couple peridynamic mechanics with a model for electrical conduction and Joule heating to simulate fracture caused by high voltage dielectric breakdown. Application of peridynamics to friction and wear at the nanoscale is demonstrated in the paper by Ebrahim, Steigmann, and Komvopoulos.

Another general theme of the special issue is making peridynamic mechanics more practical as a general analysis tool for applications involving fracture. The paper by Mitchell, Silling, and Littlewood describes a new material model within peridynamics that helps avoid difficulties due to the nonlocal nature of the theory in treating free surfaces. With the goal of applying peridynamics only within a small subregion of a large structure where damage is expected, Silling, Littlewood, and Seleson investigate techniques for varying the peridynamic horizon within a model, including application to local-nonlocal coupling. In a related paper elsewhere in this journal (DOI 10.2140/jomms.2015.10.167), Oterkus and Madenci describe a specialization of peridynamics to anti-plane shear and torsion, resulting in a considerable simplification over the full 3D equations.

These papers reflect a sample of the broad spectrum of research on the peridynamic theory ongoing around the world.

STEWART SILLING  
Sandia National Laboratories  
OLAF WECKNER  
The Boeing Company  
*Guest Editors*





## A POSITION-AWARE LINEAR SOLID CONSTITUTIVE MODEL FOR PERIDYNAMICS

JOHN A. MITCHELL, STEWART A. SILLING AND DAVID J. LITTLEWOOD

A position-aware linear solid (PALS) peridynamic constitutive model is proposed for isotropic elastic solids. The PALS model addresses problems that arise, in ordinary peridynamic material models such as the linear peridynamic solid (LPS), due to incomplete neighborhoods near the surface of a body. Improved model behavior in the vicinity of free surfaces is achieved through the application of two influence functions that correspond, respectively, to the volumetric and deviatoric parts of the deformation. The model is position-aware in that the influence functions vary over the body and reflect the proximity of each material point to free surfaces. Demonstration calculations on simple benchmark problems show a sharp reduction in error relative to the LPS model.

### 1. Introduction

The peridynamic theory of solid mechanics allows for great flexibility in the development of constitutive models. In contrast to classical, local models, which rely on a kinematic description of material deformation at a point such as the deformation gradient, material models in the peridynamic theory determine pairwise force densities based on the deformations of a nonlocal family of neighboring material points [Silling 2000; Silling and Lehoucq 2010; Madenci and Oterkus 2014]. This enrichment of kinematic information greatly expands the range of possible constitutive laws. Peridynamic material models developed to date fall into one of three categories: bond-based, ordinary state-based, and non-ordinary state-based. Bond-based peridynamic models determine the pairwise force density that acts between two material points based only on the histories of those points (e.g., initial and current positions). The prototype microelastic brittle material model was the first peridynamic constitutive law to appear in the literature [Silling 2000]. This model served as the foundation for a subsequently developed bond-based plasticity model [Macek and Silling 2007]. The state-based theory for peridynamic constitutive models represents a significant generalization of the bond-based approach [Silling et al. 2007]. The theory of peridynamic states allows for constitutive models in which pairwise force densities are functions of not only the material points in question, but also the full set of material points within the nonlocal neighborhoods of those material points. State-based constitutive models in which pairwise force densities act in the direction of the corresponding bond in the deformed configuration are referred to as *ordinary* state-based models. Examples include the linear peridynamic solid (LPS) [Silling et al. 2007] and the plasticity and viscoelasticity models developed by Mitchell [2011a; 2011b]. The third class of material models, non-ordinary state-based, is comprised of constitutive models in which pairwise force densities are not restricted to act in the bond direction. The correspondence model approach, in which classical

---

*Keywords:* peridynamics, PALS, ordinary state, lps, surface effects, elastic model, nonlocal, integral equations.

(local) constitutive models are adapted for use within peridynamics, falls into this category [Silling et al. 2007; Foster et al. 2010; Tupek and Radovitzky 2014].

This study concerns the development of an ordinary, state-based constitutive model that improves upon the performance of the material models currently available in the literature. The primary motivation is the undesirable behavior of certain peridynamic material models in the vicinity of free surfaces. This difficulty appears, for example, in a peridynamic simulation of a uniaxial tension test, illustrated in Figure 1, using the LPS constitutive model and the mesh-free discretization approach of Silling and Askari [2005]. In this simulation, the displacements at the end portions of the bar are prescribed, and the forces on the grips,  $G_y$ , are computed, along with the engineering strain in the gauge,  $\epsilon$ . The Young's modulus may then be computed as

$$E = G_y / A_g \epsilon,$$

where  $A_g$  is the undeformed cross-sectional area of the bar in the vicinity of the gauge. The expected value of Young's modulus is the slope of the green curve in Figure 2. Modern three-dimensional finite element codes can accurately reproduce the Young's modulus in a simulation of the uniaxial tension test for a linear elastic material. However, a typical three-dimensional peridynamic simulation using the LPS material model predicts the red curve in Figure 2. The difference in slope between the two curves shows that the peridynamic model under-predicts the load on the grips for a given value of strain. The LPS material parameters are calibrated for points in the interior of a body and do not take into account whether a point is near a boundary [Silling et al. 2007]. Due to the nonlocality of the peridynamic equations, the LPS material model becomes inaccurate at points near a free surface. Here, some of the peridynamic bonds that would be present in the interior are missing (Figure 3). Because bonds are missing, they do not contribute to the net force on the cross-section of the gauge, hence the total force is under-predicted. While this effect manifests for a number of constitutive models, it is not present for all models; correspondence models are an exception because missing bonds are compensated for by the shape tensor  $K$ .

The under-prediction of force at material points near a free surface is often referred to as the *surface effect* in peridynamics. This effect presents a practical difficulty in applying bond-based models and ordinary state-based models such as the LPS. Approaches for mitigating the surface effect have been proposed by Kilic, Macek and Silling, and Mitchell. Following a bond-based approach, Kilic [2008] proposed a position-aware correction that is computed iteratively for each material point. Macek and Silling [2007] developed a position-aware force normalization that scales the stiffness of points near a surface using a ratio of eigenvalues from local  $3 \times 3$  stiffness matrices, where eigenvalues are computed (with the same material properties) for points near a free surface and on the interior. Mitchell [2013] developed a position-aware scaling of moduli for the LPS model, but its efficacy was found to be somewhat sensitive to complex surface geometries.

The present study proposes an alternative approach to peridynamic constitutive modeling in which model parameters at a point reflect the point's location within the body, removing the need for auxiliary surface correction techniques. This position-aware approach is a significant departure from previously developed constitutive models in that the constitutive model parameters are linked directly with the geometry of the body. The position-aware linear solid (PALS) model presented herein is an extension of the LPS model that substantially reduces the surface effect. This is accomplished by introducing

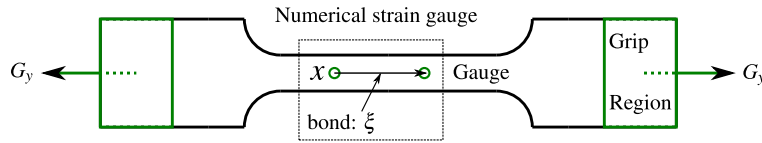


**Figure 1.** Uniaxial tension test schematic.

influence functions that are calibrated according to the bulk elastic properties at each material point, resulting in influence functions that differ for points near a free surface and points on the interior of the body. Identification of the influence functions for each point in the body is accomplished by solving a constrained minimization problem. Determination of the influence functions within a computational simulation does not require an iterative process and is instead achieved through the solution of a linear system of equations.

The present work is unique with respect to the construction and use of position-aware influence functions. As very recently pointed out by Bessa, Foster, Belytschko and Liu [Bessa et al. 2014], only constant-valued influence functions have been studied. Apparently, the two exceptions are the study by Seleson and Parks [2011] and the approach for incorporating classical damage models into state-based peridynamics by Tupek, Rimoli, and Radovitzky [Tupek et al. 2013]. Seleson and Parks used influence functions to establish relationships between bond-based and state based peridynamics models and did not consider position-aware influence functions. Influence functions developed by Tupek et al. are a product of a Gaussian and a binary valued function (0 or 1) depending upon the state of damage between two points defining a bond; this is somewhat position-aware but not in a way related to the present work.

An outline of the paper is as follows. An overview of peridynamic theory and the LPS model are given in Section 2, including calibration of the LPS parameters in the interior of a body. The influence

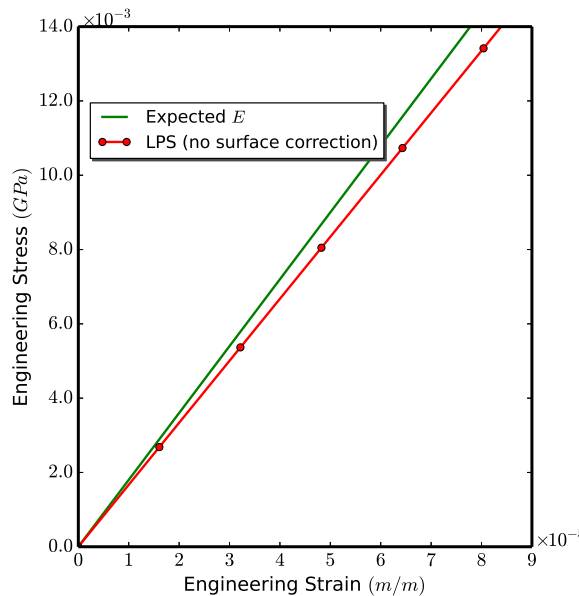


**Figure 2.** The LPS model under-predicts the Young’s modulus in a model of the uniaxial tension test.

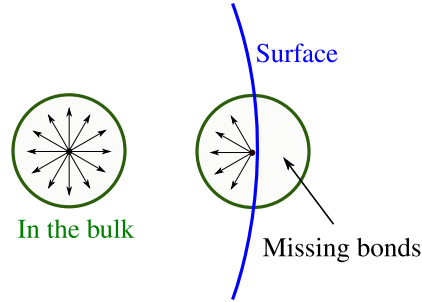


**Figure 3.** Schematic of missing peridynamic bonds.

functions used in the PALS model are derived in Section 3, followed by the formulation of the PALS force state in Section 4. The selection and usage of *matching deformations* required by the PALS model are discussed in Section 5. Section 6 presents example calculations demonstrating the efficacy of the PALS model in reducing the surface effect. Results and conclusions are given in Section 7.

## 2. Introduction to peridynamics and the LPS model

The peridynamic theory of solid mechanics [Silling 2000; Silling et al. 2007; Silling and Lehoucq 2010] is an extension of classical continuum mechanics theory [Bonet and Wood 1997]. The peridynamics extension permits discontinuities in displacements by replacing the stress divergence in the momentum equation with a volume integral

$$\rho(\mathbf{x})\ddot{\mathbf{y}}(\mathbf{x}, t) = \int_{\mathcal{B}} \mathbf{f}(\mathbf{x}', \mathbf{x}, t) dV_{\mathbf{x}'} + \mathbf{b}(\mathbf{x}, t), \quad (1)$$

where  $\mathbf{y}(\mathbf{x})$  is the current position vector of a material point  $\mathbf{x}$  at time  $t$ ,  $\rho$  is mass density in the undeformed body  $\mathcal{B}$ ,  $\mathbf{f}$  is a pairwise bond force density per unit volume,  $\mathbf{b}$  is the usual body force density, and  $\mathbf{x}'$  is an arbitrary material point within the neighborhood  $\mathcal{H}_{\mathbf{x}}$  of the point  $\mathbf{x}$ . In this section, the state-based theory of peridynamics [Silling 2000; Silling et al. 2007; Silling and Lehoucq 2010] is reviewed with emphasis on ordinary state-based constitutive models of relevance to this paper.

A *bond* vector is defined by

$$\boldsymbol{\xi} = \mathbf{x}' - \mathbf{x}, \quad 0 < |\boldsymbol{\xi}| \leq \delta,$$

where  $\delta$  is the *horizon* of the material. Conceptually,  $\delta$  is a relevant length scale and defines a spherical neighborhood  $\mathcal{H}_{\mathbf{x}}$ ; it represents the maximum distance for nonlocal interactions in the material model. Material points within the neighborhood  $\mathcal{H}_{\mathbf{x}}$  are referred to as the *family* of  $\mathbf{x}$ . It will be assumed throughout this paper that  $\delta$  is independent of  $\mathbf{x}$ .

In formulating peridynamic material models, it is convenient to use mathematical objects called *states*, which are mappings from bonds in a family to some other quantity. Vector states map bonds to vectors, and scalar states map bonds to scalars. An example of the notation used for states is as follows. The value of a vector state  $\underline{\mathbf{A}}$ , at the material point  $\mathbf{x}$  and time  $t$ , operating on a bond  $\boldsymbol{\xi}$ , is given by

$$\underline{\mathbf{A}}[\mathbf{x}, t](\boldsymbol{\xi}), \quad \mathbf{x} \in \mathcal{B}, \quad \boldsymbol{\xi} \in \mathcal{H}_{\mathbf{x}}.$$

The deformed image of a bond  $\xi = \mathbf{x}' - \mathbf{x}$  is given by the *deformation state*  $\underline{\mathbf{Y}}$ :

$$\begin{aligned}\underline{\mathbf{Y}}[\mathbf{x}, t](\xi) &= \mathbf{y}(\mathbf{x}', t) - \mathbf{y}(\mathbf{x}, t) \\ &= (\mathbf{x}' + \mathbf{u}(\mathbf{x}', t)) - (\mathbf{x} + \mathbf{u}(\mathbf{x}, t)),\end{aligned}\quad (2)$$

where  $\mathbf{u}$  is the displacement field. Further information on peridynamic states is given in [Silling et al. 2007].

The following scalar states are useful in material modeling:

- The *undeformed bond length state*  $\underline{x}$ :

$$\underline{x}(\xi) = |\xi|.$$

- The *deformed bond length state*  $|\underline{\mathbf{Y}}|$ :

$$|\underline{\mathbf{Y}}|(\xi) = |\underline{\mathbf{Y}}(\xi)|. \quad (3)$$

- The *extension state*  $\underline{e}$ :

$$\underline{e}(\xi) = |\underline{\mathbf{Y}}|(\xi) - \underline{x}(\xi). \quad (4)$$

In this paper, scalar states are underlined and written using italics, such as  $\underline{e}$ ; vector states are written using bold and underlined, as in  $\underline{\mathbf{Y}}$ .

This paper is concerned with state-based constitutive models in which the pairwise bond force density per unit volume  $\mathbf{f}(\mathbf{x}', \mathbf{x}, t)$  in (1) is given by

$$\mathbf{f}(\mathbf{x}', \mathbf{x}, t) = \underline{\mathbf{T}}[\mathbf{x}, t](\mathbf{x}' - \mathbf{x}) - \underline{\mathbf{T}}[\mathbf{x}', t](\mathbf{x} - \mathbf{x}'). \quad (5)$$

The vector state  $\underline{\mathbf{T}}[\mathbf{x}]$  is called the *force state*. In (5),  $\mathbf{f}$  contains contributions from the force states at both  $\mathbf{x}$  and  $\mathbf{x}'$  (that is, both  $\underline{\mathbf{T}}[\mathbf{x}, t]$  and  $\underline{\mathbf{T}}[\mathbf{x}', t]$ ).

In *ordinary* state-based constitutive models, the vector force state is always parallel to the deformed bond vector and written as

$$\underline{\mathbf{T}}(\xi) = \underline{t}(\xi) \underline{\mathbf{M}}(\xi), \quad (6)$$

where  $\underline{t}$  is a scalar state called the *scalar force state*, and  $\underline{\mathbf{M}}$  is a vector state that produces unit vectors parallel to the deformed bond:

$$\underline{\mathbf{M}}(\xi) = \frac{\underline{\mathbf{Y}}(\xi)}{|\underline{\mathbf{Y}}|(\xi)}. \quad (7)$$

It is assumed that deformed material points do not overlap, that is,  $\underline{\mathbf{Y}}(\xi) \neq \mathbf{0}$  for all  $\xi$ .

A *simple* material model in state-based peridynamics gives the force state as a function of the deformation state and is written  $\underline{\mathbf{T}}(\underline{\mathbf{Y}}, \mathbf{x})$ . The  $\mathbf{x}$  in this expression accounts for possible heterogeneity. All the material models considered in this paper are simple. The PALS model is inherently heterogeneous since its parameters depend on position, in particular the proximity to a free surface.

In an ordinary state-based material model, the direction of the bond force is always given by (7). Therefore, the material model is fully specified by scalar force state:  $\underline{t}(\underline{\mathbf{Y}}, \mathbf{x})$ .

The LPS model, which serves as the foundation for development of the PALS model, is summarized below.

Define the *dot product* of two scalar states  $\underline{a}$  and  $\underline{b}$  by

$$\underline{a} \bullet \underline{b} = \int_{\mathcal{K}_x} \underline{a}(\underline{\xi}) \underline{b}(\underline{\xi}) dV_{\underline{\xi}}.$$

Let  $D = 1, 2, 3$  be the number of dimensions. The *weighted volume*  $m$  and the *dilatation*  $\theta$  are scalars used in the decomposition of the extension state  $\underline{e}$  into volumetric and deviatoric parts:

$$m = (\underline{\omega x}) \bullet \underline{x}, \quad (8)$$

$$\theta = \frac{D}{m} (\underline{\omega x}) \bullet \underline{e}, \quad (9)$$

where  $\underline{\omega}$  is a scalar state called the *influence function* [Silling et al. 2007]. A key element of the constitutive model developed in this paper is the additive decomposition of the scalar extension state (4) into spherical and deviatoric parts given by

$$\underline{e} = \underline{e}^i + \underline{\varepsilon}, \quad (10)$$

where the *spherical extension state*  $\underline{e}^i$  is defined by

$$\underline{e}^i = \theta \underline{x} / D. \quad (11)$$

Using the above quantities, the *deviatoric extension state*  $\underline{\varepsilon}$  is constructed as

$$\underline{\varepsilon} = \underline{e} - \theta \underline{x} / D. \quad (12)$$

All of the above quantities are dependent on  $\mathbf{x}$  and  $\underline{Y}$ , but these dependencies are omitted from the notation for simplicity.

The scalar force state for the LPS model is derived from an elastic energy functional  $W$  of the form

$$W(\theta, \underline{\varepsilon}) = \frac{1}{2} \kappa \theta^2 + \frac{1}{2} \alpha \underline{\varepsilon} \bullet \underline{\omega \varepsilon}, \quad (13)$$

where  $\kappa$  is the bulk modulus and  $\alpha$  is a constant. This implies that  $\underline{t}$  is decomposed into scalar volumetric and deviatoric force states:

$$\underline{t} = \underline{t}^i + \underline{t}^d, \quad (14)$$

where

$$\underline{t}^i = \frac{\partial W}{\partial \theta} \frac{\partial \theta}{\partial \underline{e}^i}, \quad \underline{t}^d = \frac{\partial W}{\partial \underline{\varepsilon}}. \quad (15)$$

Here, the notation  $\partial/\partial \underline{a}$ , where  $\underline{a}$  is a state, refers to the Fréchet derivative [Silling et al. 2007]. The Fréchet derivative of a scalar-valued function  $\psi$  of a state  $\underline{a}$  has the property that, for a differential change  $d\underline{a}$ ,

$$d\psi = \frac{\partial \psi}{\partial \underline{a}} \bullet d\underline{a}. \quad (16)$$

Although geometrically nonlinear, the LPS model is a peridynamic analogue of Hooke's law for isotropic materials. For points  $\mathbf{x}$  in the interior of the body, equating the elastic energy density from the LPS material with the strain energy density from the local theory leads to the calibration (for  $D = 3$ )

$$\alpha = 15\mu/m,$$

where  $\mu$  is the conventional shear modulus from the local theory and  $m$  is given by (8). The above relation for  $\alpha$  is inaccurate for points near a free surface. Experience with the LPS model in complex geometries suggests that a simple correction to  $\alpha$  near free surfaces [Mitchell 2013] is not general enough, motivating the PALS model.

Using (15), the scalar force state for the LPS model takes the form

$$\underline{t} = \frac{D\kappa\theta}{m}\underline{\omega x} + \alpha\underline{\omega\varepsilon}. \tag{17}$$

Observe that the scalar force state contains independent terms that depend on either the isotropic or deviatoric part of the extension state.

An important side note relates to the use of (9) and (12) for cases when  $D = 1$  or  $2$ ; conditions of uniaxial stress and plane stress are local concepts which do not precisely exist in peridynamics, although practical and useful analogies exist. In particular, (9) and (12) remain valid for these and other conditions although care must be taken with respect to the choice of material parameters. The correct parameters are found by assuming appropriate homogeneous deformations and equating the local energy density with the peridynamic energy density.

### 3. PALS model and selection of influence functions

The PALS concept proposed in this paper is a kinematic correction to the dilatation and deviatoric extension states and circumvents the surface effect under a wide range of conditions. It also helps to reduce errors introduced by spatial discretizations.

The basic idea is to introduce a set of constraints and associated Lagrange multipliers which force the dilatation and deviatoric extension states to reproduce a set of predetermined deformations called *matching deformations*. Using this set of matching deformations, two linear problems (one for dilatation and one for deviatoric extension) are defined for each point; the solution to these linear problems gives two sets of Lagrange multipliers that determine the influence functions  $\underline{\omega}(\xi)$  and  $\underline{\sigma}(\xi)$ . In general, these influence functions are unique for each material point within the body; they determine the dilatation and deviatoric extension state for any deformation; importantly, they reflect the position and proximity of the point to free surfaces. Both  $\underline{\omega}$  and  $\underline{\sigma}$  depend on  $\mathbf{x}$ , although this dependence is omitted from the notation in the following discussion.

In the remainder of this article, the following linear approximation to the extension state will be used:

$$\underline{e}(\xi) = \frac{\xi \cdot \underline{U}(\xi)}{|\xi|}, \quad \underline{U}(\xi) = \underline{Y}(\xi) - \xi \quad \text{for all } \xi \in \mathcal{H}_x. \tag{18}$$

The vector state  $\underline{U}$  is called the *displacement state*.

In the PALS model, the elastic energy density at a point  $\mathbf{x}$  is defined by

$$W(\theta, \underline{\varepsilon}) = \frac{1}{2}\kappa\theta^2 + \mu(\underline{\sigma\varepsilon}) \bullet \underline{\varepsilon}, \tag{19}$$

where  $\mu$  is the shear modulus and  $\underline{\varepsilon}$  is defined in (12);  $\underline{\sigma}$  is a new influence function called the *deviatoric influence function*. The dilatation  $\theta$  is defined using the extension state  $\underline{e}$  by

$$\theta = (\underline{\omega x}) \bullet \underline{e}, \tag{20}$$

where  $\underline{\omega}$  is normalized such that the weighted volume  $m$  used in the LPS is not needed (that is,  $m = D$ ). The new influence function  $\underline{\omega}$  is constructed starting from a given influence function  $\underline{\omega}^0$  which is arbitrary. Typically, one assumes that  $\underline{\omega}^0$  follows some convenient dependence on bond length such as a constant or a Gaussian.

Assume that a set of displacement gradient tensors  $\mathbf{H}^1, \mathbf{H}^2, \dots, \mathbf{H}^K$  are given — these are the *matching deformations*. The new influence function  $\underline{\omega}$  is constructed as a best approximation to  $\underline{\omega}^0$  subject to constraints which ensure the dilatation for each of the matching deformations is reproduced exactly;  $\underline{\omega}$  is determined such that the dilatation induced by each  $\mathbf{H}^k$  and evaluated using (18) and (20) equals the trace of the matching deformation  $\mathbf{H}^k$ . Note that there are no symmetry requirements on the matching deformations; this will become even more apparent in the construction of the deviatoric influence function.

Assume that a scalar state  $\underline{\omega}^0$  is given, and let  $\lambda^1, \lambda^2, \dots, \lambda^K$  be Lagrange multipliers — one for each matching deformation  $\mathbf{H}^k$ . To find  $\underline{\omega}$ , define a functional  $I$  by

$$I(\underline{\omega}, \lambda^1, \dots, \lambda^K) = \frac{1}{2}(\underline{\omega} - \underline{\omega}^0) \bullet (\underline{\omega} - \underline{\omega}^0) - \sum_{k=1}^K \lambda^k [(\underline{\omega} \underline{x}) \bullet \underline{e}^k - \text{trace } \mathbf{H}^k], \quad (21)$$

where the linear extension states  $\underline{e}^k$  (see (18)) are defined using the matching deformations  $\mathbf{H}^k$  by

$$\underline{e}^k \langle \underline{\xi} \rangle = \frac{\underline{\xi} \cdot (\mathbf{H}^k \underline{\xi})}{|\underline{\xi}|} \quad \text{for all } \underline{\xi} \in \mathcal{H}_x. \quad (22)$$

It is required that  $I$  be stationary with respect to  $\underline{\omega}$  and  $\lambda^1, \dots, \lambda^K$ . Taking the first variation of  $I$  leads to

$$\delta I = \frac{\partial I}{\partial \underline{\omega}} \bullet \delta \underline{\omega} + \sum_{k=1}^K \frac{\partial I}{\partial \lambda^k} \delta \lambda^k, \quad (23)$$

where  $\partial I / \partial \underline{\omega}$  denotes the Fréchet derivative of  $I$  with respect to  $\underline{\omega}$ . Observe that, for a given  $k$ ,  $1 \leq k \leq K$ ,

$$\frac{\partial I}{\partial \lambda^k} = 0 \quad \Rightarrow \quad (\underline{\omega} \underline{x}) \bullet \underline{e}^k = \text{trace } \mathbf{H}^k, \quad (24)$$

which means the state  $\underline{\omega}$  exactly reproduces the dilatations in the matching deformations. Furthermore, referring to the first term on the right-hand side of (21), this  $\underline{\omega}$  approximates the desired  $\underline{\omega}^0$  in the least squares sense. Evaluating the Fréchet derivative of the right-hand side of (21) with respect to  $\underline{\omega}$  gives

$$\frac{\partial I}{\partial \underline{\omega}} = 0 \quad \Rightarrow \quad \underline{\omega} = \underline{\omega}^0 + \sum_{k=1}^K \lambda^k \underline{x} \underline{e}^k. \quad (25)$$

This relation reveals the structure of  $\underline{\omega}$ : it differs from  $\underline{\omega}^0$  by a linear combination of the states  $\underline{x} \underline{e}^k$ ,  $k = 1, 2, \dots, K$ . To evaluate the  $\lambda^k$  explicitly, impose the  $K$  requirements from the matching deformations using (25):

$$\begin{aligned} \text{trace } \mathbf{H}^k &= (\underline{\omega} \underline{x}) \bullet \underline{e}^k = \left[ \left( \underline{\omega}^0 + \sum_{n=1}^K \lambda^n \underline{x} \underline{e}^n \right) \underline{x} \right] \bullet \underline{e}^k \\ &= (\underline{\omega}^0 \underline{x}) \bullet \underline{e}^k + \sum_{n=1}^K \lambda^n (\underline{x} \underline{e}^n) \bullet (\underline{x} \underline{e}^k), \quad k = 1, 2, \dots, K. \end{aligned} \quad (26)$$



This is a nonhomogeneous linear algebraic system with unknowns  $\lambda^1, \lambda^2, \dots, \lambda^K$ . The solution to this system, together with (25), provides the desired influence function  $\underline{\omega}$  within a constant scale factor  $c$ . For consistency with the decomposition of the extension state (see (10)–(12))  $c$  is chosen so that

$$(c\underline{\omega}\underline{x}) \bullet \underline{x} = D. \quad (27)$$

Now consider the deviatoric part of the strain energy. In the PALS model, as in the LPS model, this is treated by summing the energies in the deviatoric bond extensions. Motivated by the stored elastic energy density function in (19), it is convenient to express the deviatoric contribution in terms of the *total shear* defined by

$$\gamma = (\underline{\sigma}\underline{\varepsilon}) \bullet \underline{\varepsilon}, \quad (28)$$

thus, from (19),

$$W = \frac{1}{2}\kappa\theta^2 + \mu\gamma. \quad (29)$$

Recall that, in the classical theory, for any displacement gradient  $\mathbf{H}$ ,

$$W = \frac{1}{2}\kappa\theta^2 + \mu \text{trace}[\text{dev sym } \mathbf{H}]^T [\text{dev sym } \mathbf{H}]. \quad (30)$$

The deviatoric tensor in this expression is the deviatoric strain tensor:

$$\epsilon^d = \text{dev sym } \mathbf{H}, \quad \epsilon_{ij}^d = \frac{1}{2}(H_{ij} + H_{ji}) - \frac{H_{kk}\delta_{ij}}{D}. \quad (31)$$

Combining (28)–(30) provides the requirement on  $\underline{\sigma}$  that, for any of the matching deformations  $\mathbf{H}^k$ ,

$$(\underline{\sigma}\underline{\varepsilon}^k) \bullet \underline{\varepsilon}^k = \text{trace}[\text{dev sym } \mathbf{H}^k]^T [\text{dev sym } \mathbf{H}^k]. \quad (32)$$

Suppose a reference influence function  $\underline{\sigma}^0$  is given. Proceeding as with the dilatational contribution, define a functional  $N(\underline{\sigma}, \tau^1, \dots, \tau^K)$  by

$$N(\underline{\sigma}, \tau^1, \dots, \tau^K) = \frac{1}{2}(\underline{\sigma} - \underline{\sigma}^0) \bullet (\underline{\sigma} - \underline{\sigma}^0) - \sum_{k=1}^K \tau^k [(\underline{\sigma}\underline{\varepsilon}^k) \bullet \underline{\varepsilon}^k - \gamma^k], \quad (33)$$

where  $\tau^1, \tau^2, \dots, \tau^K$  are Lagrange multipliers,

$$\gamma^k := \text{trace}[\text{dev sym } \mathbf{H}^k]^T [\text{dev sym } \mathbf{H}^k], \quad (34)$$

and

$$\underline{\varepsilon}^k = \underline{e}^k - (\text{trace } \mathbf{H}^k)\underline{x}/D. \quad (35)$$

The influence function  $\underline{\sigma}$  and the associated Lagrange multipliers are found by taking the first variation of (33):

$$\delta N = \frac{\partial N}{\partial \underline{\sigma}} \bullet \delta \underline{\sigma} + \sum_{k=1}^K \frac{\partial N}{\partial \tau^k} \delta \tau^k. \quad (36)$$

Requiring  $N$  to be stationary,

$$\frac{\partial N}{\partial \tau^k} = 0 \quad \Rightarrow \quad (\underline{\sigma}\underline{\varepsilon}^k) \bullet \underline{\varepsilon}^k = \gamma^k \quad (37)$$

and

$$\frac{\partial N}{\partial \underline{\sigma}} = 0 \quad \Rightarrow \quad \underline{\sigma} = \underline{\sigma}^0 + \sum_{k=1}^K \tau^k \underline{\varepsilon}^k \underline{\varepsilon}^k. \quad (38)$$

This leads to the following nonhomogeneous linear algebraic system with unknowns  $\tau^k$ :

$$\gamma^k = (\underline{\sigma}^0 \underline{\varepsilon}^k) \bullet \underline{\varepsilon}^k + \sum_{n=1}^K \tau^n (\underline{\varepsilon}^n \underline{\varepsilon}^n) \bullet (\underline{\varepsilon}^k \underline{\varepsilon}^k), \quad k = 1, 2, \dots, K. \quad (39)$$

When taken with (38), the  $\tau^n$  values that solve this system give the  $\underline{\sigma}$  states for the PALS model at a given point  $\mathbf{x}$ .

Except for the interior of the body, where the neighborhood  $\mathcal{H}_{\mathbf{x}}$  does not intersect with the free surface,  $\lambda^n$  and  $\tau^n$  depend on  $\mathbf{x}$ . Because this calibration varies from point to point, the model is *position aware*. In summary, the PALS model is calibrated at each  $\mathbf{x}$  by the following steps:

- (1) Define initial guesses for  $\underline{\omega}^0$  and  $\underline{\sigma}^0$ .
- (2) Choose  $K$  linearly independent displacement gradient tensors  $\mathbf{H}^1, \dots, \mathbf{H}^K$ . (In three dimensions, we choose  $K = 6$  because there are at most 6 linearly independent strain tensors.)
- (3) Solve the  $K \times K$  linear algebraic system given by (26) for  $\lambda^1, \dots, \lambda^K$ .
- (4) Find  $\underline{\omega}$  from (25) and normalize according to (27).
- (5) Solve the  $K \times K$  linear algebraic system given by (39) for  $\tau^1, \dots, \tau^K$ .
- (6) Find  $\underline{\sigma}$  from (38).

In general, values of  $\underline{\omega}(\xi)$  and  $\underline{\sigma}(\xi)$  may be negative for some bonds in the family. This is acceptable and does not lead to material instability, since it does not necessarily imply imaginary wave speeds [Silling and Lehoucq 2010].

In a computational implementation, it is sufficient to evaluate and store the  $2K$  Lagrange multipliers (for each node in the discretization) at the start of a run and, on the fly, compute influence functions as they are needed. This uses less memory (but requires more floating point operations) than saving influence function values on each bond for every point. The cost of evaluating one of the two PALS model influence functions is very similar to the cost of evaluating the LPS model influence function, although it requires retrieval and use of  $K$  Lagrange multiplier values for each point.

The cost/benefit analysis of using the PALS model is problem-dependent and relates to the domain geometry and the ratio of surface area to volume. Since peridynamics is fundamentally oriented towards fracture, it is likely that surface effects increase as new surfaces are created with each fracture. If bonds are broken during a simulation, the PALS model influence functions should be recomputed subject to a cost/benefit analysis which is beyond the scope of this paper. Simple engineering demonstration calculations later in this paper were chosen which highlight the degree to which surface effects can degrade the LPS model; in these cases the PALS model substantially reduces the surface effect.

#### 4. PALS scalar force state

In the preceding section, the influence functions  $\underline{\omega}$  and  $\underline{\sigma}$  were determined. Now we evaluate the bond forces using these influence functions. Recall that the strain energy density is given by (19).

The scalar force state  $\underline{t}$  is found from the Fréchet derivative of  $W$  with respect to  $\underline{e}$ :

$$\underline{t} = \frac{\partial W}{\partial \underline{e}}.$$

To evaluate  $\underline{t}$  explicitly, consider a change in the elastic energy density due to a small change  $\underline{\Delta e}$  in the extension state and use (16):

$$\frac{\partial W}{\partial e} \bullet \underline{\Delta e} = \underline{t} \bullet \underline{\Delta e}. \tag{40}$$

Using (12), (19), and (20) for the PALS stored elastic energy density  $W$ , the change  $\Delta W$  is explicitly evaluated as

$$\begin{aligned} \underline{t} \bullet \underline{\Delta e} = \Delta W &= \kappa \theta \underline{\omega x} \bullet \underline{\Delta e} + 2\mu \underline{\sigma \varepsilon} \bullet \left( \underline{\Delta e} - \frac{\Delta \theta x}{D} \right) \\ &= \left[ \left( \kappa \theta - \frac{2\mu}{D} \underline{\sigma \varepsilon} \bullet x \right) \underline{\omega x} + 2\mu \underline{\sigma \varepsilon} \right] \bullet \underline{\Delta e}. \end{aligned} \tag{41}$$

From this, the scalar force state  $\underline{t}$  is directly identified as

$$\underline{t} = \left( \kappa \theta - \frac{2\mu}{D} (\underline{\sigma x}) \bullet \underline{\varepsilon} \right) \underline{\omega x} + 2\mu \underline{\sigma \varepsilon}. \tag{42}$$

The term involving  $(\underline{\sigma x}) \bullet \underline{\varepsilon}$  appears because different influence functions  $\underline{\omega}$  and  $\underline{\sigma}$  are used for the dilatational and deviatoric terms in the elastic energy density. If  $\underline{\omega} \equiv \underline{\sigma}$ , then this term vanishes, as in the LPS model. The (vector) force state is found from (6).

### 5. Matching deformations

The PALS model development in Section 3 was generic with respect to the use of specific matching deformations  $\mathbf{H}^1, \mathbf{H}^2, \dots, \mathbf{H}^K$ . In this section, a sample set of matching deformations is provided. The matching deformations provided here were used in the example problems described in the next section; they are expected to provide good results in general, although alternative choices are possible. When  $D = 3$  (three dimensions), the local theory strain tensor has 6 independent components, hence we choose  $K = 6$  matching deformations. The strain components will be denoted  $XX, YY, ZZ, XY, XZ, YZ$ . The matching deformations (shown below) represent three deformations for uniaxial strain and three for simple shear:

$$\mathbf{H}^1 = \begin{bmatrix} XX & 0 & 0 \\ 0 & 0 & 0 \\ 0 & 0 & 0 \end{bmatrix}, \quad \mathbf{H}^2 = \begin{bmatrix} 0 & 0 & 0 \\ 0 & YY & 0 \\ 0 & 0 & 0 \end{bmatrix}, \quad \mathbf{H}^3 = \begin{bmatrix} 0 & 0 & 0 \\ 0 & 0 & 0 \\ 0 & 0 & ZZ \end{bmatrix}, \tag{43}$$

$$\mathbf{H}^4 = \begin{bmatrix} 0 & XY & 0 \\ XY & 0 & 0 \\ 0 & 0 & 0 \end{bmatrix}, \quad \mathbf{H}^5 = \begin{bmatrix} 0 & 0 & XZ \\ 0 & 0 & 0 \\ XZ & 0 & 0 \end{bmatrix}, \quad \mathbf{H}^6 = \begin{bmatrix} 0 & 0 & 0 \\ 0 & 0 & YZ \\ 0 & YZ & 0 \end{bmatrix}. \tag{44}$$

Let  $(a, b, c)$  be components of a bond vector  $\xi$  and let  $|\xi|$  denote its length. It is convenient to set the magnitudes of the strain components  $XX, \dots, YZ$  all equal to the same small positive number  $\Delta$ . Using (18), the extension states  $\underline{e}^k$  are computed, one for each matching deformation:

$$\underline{e}^1 = \frac{\Delta a^2}{|\xi|}, \quad \underline{e}^2 = \frac{\Delta b^2}{|\xi|}, \quad \underline{e}^3 = \frac{\Delta c^2}{|\xi|}, \quad \underline{e}^4 = \frac{2ab\Delta}{|\xi|}, \quad \underline{e}^5 = \frac{2ac\Delta}{|\xi|}, \quad \underline{e}^6 = \frac{2bc\Delta}{|\xi|}. \tag{45}$$

These extension states are used to form the symmetric  $6 \times 6$  matrix associated with the linear problems defined in (26) and (39). Entries in the matrix are evaluated using a quadrature scheme that is consistent

with the discretized form of the momentum equation. For example, if the mesh-free approach of Silling and Askari [2005] is employed, then dot products between state  $\underline{a}$  and  $\underline{b}$  are approximated by

$$\underline{a} \cdot \underline{b} = \int_{\mathcal{H}_x} \underline{a}(\underline{\xi}) \underline{b}(\underline{\xi}) dV_{\xi} \approx \sum_j \underline{a}_j \underline{b}_j V_j,$$

where  $j$  is a node number,  $V_j$  is its associated volume in the undeformed configuration, and  $\underline{a}_j$  and  $\underline{b}_j$  denote the value of the states  $\underline{a}$  and  $\underline{b}$  acting on the  $j$ -th bond (associated with node  $j$ ).

In the remainder of this section, specific details are given for dilatation and shear. For the matching deformations given above, components of the right-hand side vector associated with the linear problems are given. It is shown that the Lagrange multipliers,  $\lambda^k$  and  $\tau^k$  are independent of  $\Delta$  (magnitude of the strain components implied by the matching deformations).

**5.1. Dilatation influence function.** As a starting point for computing the dilatation influence function  $\underline{\omega}$  at a point, a reference influence function  $\underline{\omega}^0$  is assumed to be given. Then, using the definitions for  $\underline{e}^n$  defined in (45), it is helpful to define a scaled set of states  $\hat{\underline{e}}^n$  as

$$\underline{e}^n = \frac{\Delta \hat{\underline{e}}^n}{|\underline{\xi}|}. \quad (46)$$

Using this expression for the matching states, the linear problem defined in (26) is written as

$$\Delta^2 \sum_{k=1}^K (\hat{\underline{e}}^n \cdot \hat{\underline{e}}^k) \lambda^k = \text{trace}(\mathbf{H}^n) - \Delta \underline{\omega}^0 \cdot \hat{\underline{e}}^n, \quad (47)$$

where  $K = 6$  equations are generated by  $n = 1, 2, \dots, K$ . Because each  $\mathbf{H}^n$  is proportional to the applied deformation  $\Delta$ , the Lagrange multipliers  $\lambda^n$  are inversely proportional to  $\Delta$ . The linear problem in (47) can be rewritten as

$$\Delta^2 [K_{\lambda}] \{\lambda\} = \Delta \{\hat{R}\}, \quad (48)$$

where  $[K_{\lambda}]$  denotes the  $6 \times 6$  matrix implied by (26) and (47),  $\{\lambda\}$  denotes the unknown array of six Lagrange multiplier values, and  $\{\hat{R}\}$  denotes the right-hand side array of components defined in (47). Solving the scaled system gives the Lagrange multipliers as

$$\{\lambda\} = \{\hat{\lambda}\} / \Delta,$$

where  $\{\hat{\lambda}\} = [K_{\lambda}]^{-1} \{\hat{R}\}$ . Based upon the matching deformations ((43) and (44)) and the corresponding extension states given in (45), the dilatation influence function takes the form

$$\underline{\omega} = \underline{\omega}^0 + \sum_{k=1}^K \hat{\lambda}^k \hat{\underline{e}}^k = \underline{\omega}^0 + \hat{\lambda}^1 a^2 + \hat{\lambda}^2 b^2 + \hat{\lambda}^3 c^2 + 2\hat{\lambda}^4 ab + 2\hat{\lambda}^5 ac + 2\hat{\lambda}^6 bc. \quad (49)$$

As a final step, the above influence function is normalized according to (27).

**5.2. Deviatoric influence function.** The procedure used to compute the deviatoric Lagrange multipliers is analogous to the procedure for computing the dilatation Lagrange multipliers. The deviatoric Lagrange multipliers are computed using the linear problem defined in (39). Using the matching deformations provided in this section, the deviatoric extension states  $\underline{\varepsilon}^k$  defined in (35) take the following specific form:

$$\underline{\varepsilon}^1 = \underline{e}^1 - \frac{1}{3}\Delta|\xi|, \quad \underline{\varepsilon}^2 = \underline{e}^2 - \frac{1}{3}\Delta|\xi|, \quad \underline{\varepsilon}^3 = \underline{e}^3 - \frac{1}{3}\Delta|\xi|, \quad \underline{\varepsilon}^4 = \underline{e}^4, \quad \underline{\varepsilon}^5 = \underline{e}^5, \quad \underline{\varepsilon}^6 = \underline{e}^6. \quad (50)$$

Observe that the matching deviatoric extension states vary linearly with  $\Delta$  so that a set of scaled deviatoric extension states can be defined as  $\underline{\varepsilon}^k = \Delta \hat{\underline{\varepsilon}}^k$ . The linear problem in (39) can be rewritten as

$$\Delta^4[K_\tau]\{\tau\} = \Delta^2\{\hat{R}\}. \quad (51)$$

Solving the scaled system gives the Lagrange multipliers as

$$\{\tau\} = \{\hat{\tau}\}/\Delta^2,$$

where  $\{\hat{\tau}\} = [K_\tau]^{-1}\{\hat{R}\}$ . Based upon the matching deformations ((43) and (44)) and the corresponding extension states given in (50), the deviatoric influence function takes the form

$$\underline{\sigma} = \underline{\sigma}^0 + \sum_{k=1}^K \hat{\tau}^k \hat{\underline{\varepsilon}}^k \hat{\underline{\varepsilon}}^k, \quad (52)$$

where  $\underline{\sigma}^0$  is the given reference influence function.

## 6. Demonstration calculations

Computational simulation results are presented below for the purpose of comparing the performance of the PALS model against the LPS model. Results for a beam in tension, a hollow cylinder subjected to torsional loading, and a tensile test simulation for material characterization are given. The simulations were carried out using the *Peridigm* [Parks et al. 2012; Peridigm 2014] code following the mesh-free method of Silling and Askari [2005]. All demonstration calculations are three-dimensional and results were obtained by solving the momentum equation under conditions of static equilibrium. The *Cubit* code [Cubit 2014] was utilized to generate the discretization, and the *Paraview* code [ParaView 2014] was used for visualization of results. For further discussion of the numerical solution procedure, see [Silling and Askari 2005] and [Littlewood  $\geq$  2015].

**6.1. Square beam in tension.** This demonstration calculation is a simpler version of the tensile test described in the introduction (Section 1). A known/measured value for Young’s modulus  $E$  is given and a simple peridynamics calculation is conducted to recover  $E$  and verify the efficacy of the PALS model. In this calculation (schematic shown in Figure 4), one end of the beam is fixed while the other end has a prescribed small displacement  $u_0$ ; Dirichlet boundary conditions are applied to the end sections (shown in green) as  $u(z) = zu_0/L$ , where  $z$  is an axial coordinate with an origin  $z = 0$  centered in one of the green sections. The equilibrium solution for the displacement field is computed and reaction forces  $P$  are calculated as a post-processing step. From elementary mechanics of materials, the reaction force is

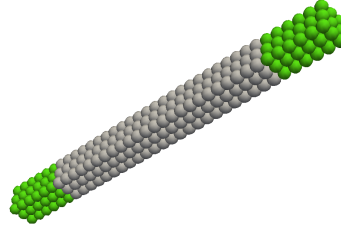


**Figure 4.** Schematic of square beam for verification of Young's modulus.

related to the applied displacement and geometric properties of the beam:

$$P = \frac{AE}{L} u_0, \quad (53)$$

where  $A = b^2$  denotes the cross-sectional area of the beam, and  $L$  denotes the length of the beam. Material and geometric properties used for these calculations are given in Tables 1 and 2. The horizon parameter  $\delta = 3.1h$  was used, where  $h = b/n$  is the mesh spacing, and  $n$  is the number of nodes along one axis of the cross-section. Graphical results for these calculations are shown in Figure 5. Error in the effective value of Young's modulus (slope of the stress-strain curve) is shown in Table 3 for a few different numerical mesh discretizations. The table gives results for two types of initial influence functions:

- Constant:

$$\underline{\omega}^0(\xi) = \underline{\sigma}^0(\xi) = 1.$$

- Gaussian:

$$\underline{\omega}^0(\xi) = \underline{\sigma}^0(\xi) = G(\delta, \xi) = e^{-|\xi|^2/\delta^2}.$$

Although oscillations are observed in the PALS results shown, the PALS model errors are substantially less than those of the LPS model for all discretizations.

**6.2. Twist test.** The focus of this example is on recovering the shear modulus  $\mu$ . In this calculation,  $\mu$  is estimated by applying an angle of twist  $\phi$  to a circular hollow cylinder. A schematic of the cylinder is depicted in Figure 6; material and geometric properties used in the calculations are given in Tables 1 and 4.

Under the assumptions that every cross-section of the cylinder remains plane and undistorted and that the material remains linearly elastic, the relationship between the angle of twist  $\phi$  and the applied

| Property             | Value                  | Units                |
|----------------------|------------------------|----------------------|
| Bulk modulus: $k$    | $1.5 \times 10^{12}$   | dyne/cm <sup>2</sup> |
| Shear modulus: $\mu$ | $6.923 \times 10^{11}$ | dyne/cm <sup>2</sup> |

**Table 1.** Isotropic elastic material properties.

| Property         | Value | Units |
|------------------|-------|-------|
| Edge length: $b$ | 0.5   | cm    |
| Length: $L$      | 5.0   | cm    |

**Table 2.** Square beam geometric properties. See Figure 4.

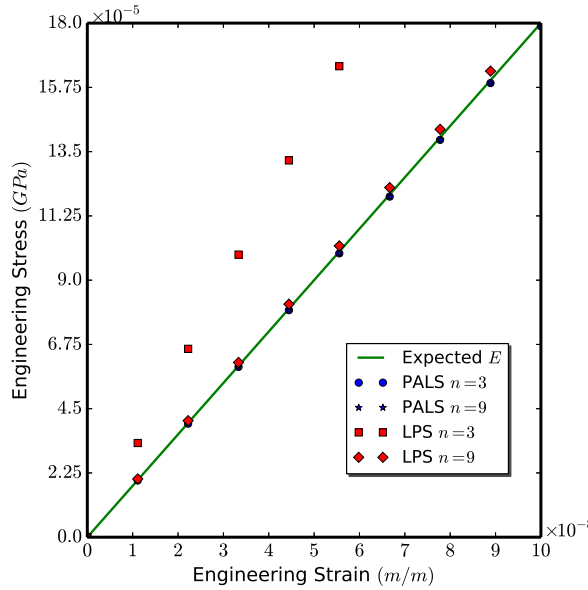


**Figure 5.** Computed stress-strain curves for the square beam in tension (Figure 4). The slope represents the effective Young’s modulus in the computational model.

torque  $T$  is

$$T = \mu J \phi / L, \tag{54}$$

where  $J$  is the area polar moment of inertia of the cross-section, and  $L$  is the length of the cylinder. Dirichlet boundary conditions are applied on points depicted in green (see Figure 6). The angles of twist applied at the ends are

$$\phi(0) = 0, \quad \phi(L) = \phi_L.$$

The expected angle of twist on any cross-section with axial position  $z$  is  $\phi(z) = z\phi_L/L$ . The computational model finds a resultant torque  $T$  from which  $\mu$  is recovered using (54). A relative error for recovery of the shear modulus  $\mu$  is computed. This error is calculated as  $(\hat{\mu} - \mu)/\mu$ , where  $\hat{\mu}$  was estimated from the PALS or LPS models using (54), and  $\mu$  is the input value given in Table 1. For these calculations, the horizon parameter  $\delta = 3.1h$  was used, where  $h = (r_o - r_i)/n$ , and  $n$  is the number of nodes through the thickness of the cylinder.

| Mesh | PALS  |  | LPS                        |   |
|------|---|--|----------------------------|---|
|      | $\underline{\omega}^0 = \underline{\sigma}^0 = 1$ | $\underline{\omega}^0 = \underline{\sigma}^0 = G(\delta, \xi)$ | $\underline{\omega}^0 = 1$ | $\underline{\omega}^0 = G(\delta, \xi)$ |
| 3    | 0.00621   | 0.00621  | 0.649                      | 0.649                                   |
| 5    | 0.000686  | 0.000685   | 0.173                      | 0.173                                   |
| 7    | 0.00820   | 0.0082   | 0.0723                     | 0.0723                                  |
| 9    | 0.00595   | 0.00595  | 0.0201                     | 0.0201                                  |

**Table 3.** Relative error in the computed Young’s modulus for a beam under uniaxial tension.

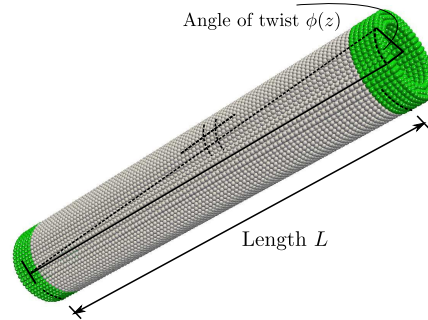


**Figure 6.** Schematic of twist test for verification of shear modulus.

Numerical results of demonstration calculations are given in Table 5 for a few different mesh discretizations. This is a particularly challenging problem because the expected solution is not a homogeneous (affine) deformation since the shear strain depends on the radial coordinate; relatedly, the local elastic energy density is independent of the axial coordinate  $z$  and varies quadratically as a function of the radial coordinate; this is shown in Figure 7 for the finest discretization,  $n = 9$ , as listed Table 5. The PALS model influence functions were computed at each point using affine matching deformations, so good results are not guaranteed by this particular choice of matching deformations. Nevertheless, the PALS model continues to show a significant reduction in error with respect to the LPS model. Better accuracy with the PALS model would be expected for thinner walled tubes, since the deformation would more closely approximate simple shear.

Several additional points are made with respect to Figure 7. This plot shows the spatial variation of the elastic energy density for any cross-section along the axis of the cylinder. Each color bar is scaled using the local analytic minimum and maximum values. Tick labels on color bars for LPS and PALS are the minimum and maximum values computed while tick labels for the local analytic calculation are the

| Property            | Value | Units |
|---------------------|-------|-------|
| Inner radius: $r_i$ | 0.667 | cm    |
| Outer radius: $r_o$ | 1.0   | cm    |
| Length $L$          | 5.0   | cm    |

**Table 4.** Twist test geometric parameters.

| Mesh | PALS  |  | LPS                        |   |
|------|---|--|----------------------------|---|
|      | $\underline{\omega}^0 = \underline{\sigma}^0 = 1$ | $\underline{\omega}^0 = \underline{\sigma}^0 = G(\delta, \xi)$ | $\underline{\omega}^0 = 1$ | $\underline{\omega}^0 = G(\delta, \xi)$ |
| 3    | 0.097   | 0.097  | 0.303                      | 0.276                                   |
| 5    | 0.056   | 0.056  | 0.168                      | 0.158                                   |
| 7    | 0.040   | 0.040  | 0.131                      | 0.121                                   |
| 9    | 0.026   | 0.026  | 0.117                      | 0.107                                   |

**Table 5.** Relative error in the computed shear modulus  $\mu$  for the twist test example.



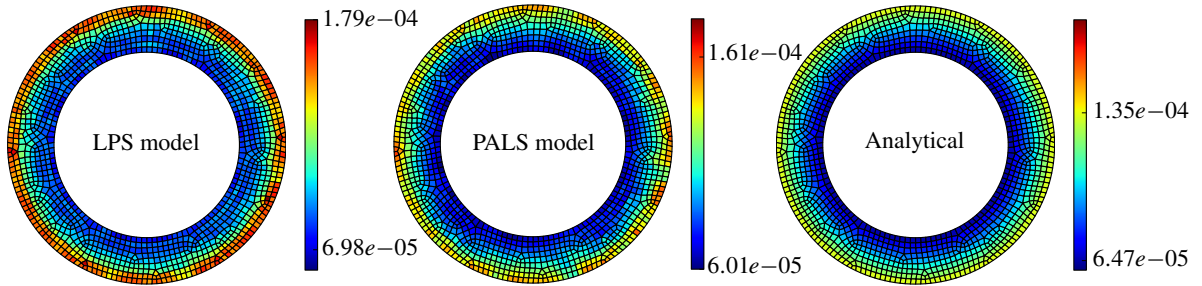


**Figure 7.** Elastic energy density for twist test calculation using LPS and PALS;  $\underline{\omega}^0 = \underline{\sigma}^0 = G(\delta, \xi)$ .

exact minimum and maximum values. As shown, the PALS model resolves the spatial variation of the energy density better than the LPS model. As previously mentioned, these calculations were done using *Peridigm* [Parks et al. 2012; Peridigm 2014]; in preparation for running *Peridigm*, the geometry of the domain is first discretized (in this case with hexahedra); for each hexahedron an equivalent peridynamic nodal volume is created and located at its centroid; although the plots in Figure 7 show a quadrilateral discretization (which corresponds to a cross-sectional view of hexahedra), this is only for plotting convenience. All calculations were fully 3D using the mesh-free method [Silling and Askari 2005].

**6.3. Tension test.** As a final demonstration calculation, the PALS model is applied to the motivation problem described in Section 1 (see Figure 1). A full three-dimensional model of the specimen was used. Improved accuracy in reproducing  $E$  using the PALS model, compared with the LPS model, is shown in Figure 8.

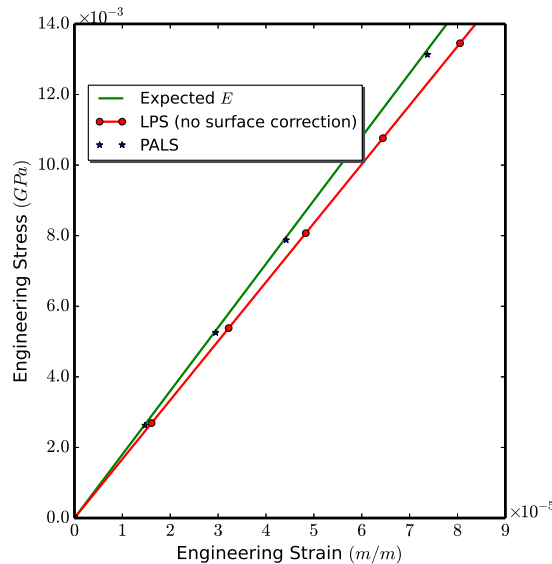


**Figure 8.** Stress-strain curve for a full 3D peridynamic model of the uniaxial tension test with PALS and LPS; both on the same discretization.

## 7. Summary and conclusions

A new position aware linear solid (PALS) model for peridynamics was introduced. The PALS model is an ordinary-state-based peridynamics constitutive model that addresses inaccuracies in previous models, most notably the linear peridynamic solid (LPS) [Silling et al. 2007], due to the surface effect [Mitchell 2013]. The PALS model addresses problems that arise due to missing bonds (see Figure 3) near the surface of a peridynamic body. Using this new model, simple benchmark calculations demonstrate large reductions in the surface effect. Although the development given in the present paper is for linear elastic materials, work currently in progress suggests that previously developed plasticity and viscoelasticity models [Mitchell 2011a; 2011b] can be extended to include some aspects of the PALS approach.

## Acknowledgements

This work was supported through a Laboratory-Directed Research and Development (LDRD) project at Sandia National Laboratories. The authors would like to thank Dan Turner, Pablo Seleson, Mike Parks, and Max Gunzburger for helpful discussions during the course of this work. Sandia is a multiprogram laboratory operated by Sandia Corporation, a Lockheed Martin Company, for the United States Department of Energy under Contract DE-AC04-94AL85000.

## References

- [Bessa et al. 2014] M. A. Bessa, J. T. Foster, T. Belytschko, and W. K. Liu, “A meshfree unification: reproducing kernel peridynamics”, *Comput. Mech.* **53**:6 (2014), 1251–1264.
- [Bonet and Wood 1997] J. Bonet and R. D. Wood, *Nonlinear continuum mechanics for finite element analysis*, Cambridge University Press, 1997. Second edition published in 2008.
- [Cubit 2014] Cubit, “Cubit mesh generation code”, 2014, <http://cubit.sandia.gov>.
- [Foster et al. 2010] J. T. Foster, S. A. Silling, and W. W. Chen, “Viscoplasticity using peridynamics”, *Int. J. Numer. Methods Eng.* **81**:10 (2010), 1242–1258.
- [Kilic 2008] B. Kilic, *Peridynamic theory for progressive failure prediction in homogeneous and heterogeneous materials*, Ph.D. thesis, University of Arizona, Tucson, AZ, 2008.
- [Littlewood  $\geq$  2015] D. J. Littlewood, “Roadmap for software implementation”, in *Handbook of peridynamic modeling*, edited by F. Bobaru et al., Chapman Hall/CRC, Boca Raton, FL. Expected publication 2015.
- [Macek and Silling 2007] R. W. Macek and S. A. Silling, “Peridynamics via finite element analysis”, *Finite Elem. Anal. Des.* **43**:15 (2007), 1169–1178.
- [Madenci and Oterkus 2014] E. Madenci and E. Oterkus, *Peridynamic theory and its applications*, Springer, New York, 2014.
- [Mitchell 2011a] J. A. Mitchell, “A nonlocal, ordinary, state-based plasticity model for peridynamics”, SAND report 2011-3166, Sandia National Laboratories, 2011, <https://cfwebprod.sandia.gov/cfdocs/CompResearch/docs/SAND2011-3166.pdf>.
- [Mitchell 2011b] J. A. Mitchell, “A non-local, ordinary-state-based viscoelasticity model for peridynamics”, SAND report 2011-8064, Sandia National Laboratories, Albuquerque, NM and Livermore, CA, 2011, <https://cfwebprod.sandia.gov/cfdocs/CompResearch/docs/SAND2011-Viscoelasticity.pdf>.
- [Mitchell 2013] J. A. Mitchell, “On the ‘DSF’ and the ‘dreaded surface effect’”, slides of presentation at Workshop on Nonlocal Damage and Failure (San Antonio, TX, 2013), Sandia National Laboratories, 2013, <https://cfwebprod.sandia.gov/cfdocs/CompResearch/docs/SAND2013-1927C.pdf>.
- [ParaView 2014] ParaView, “ParaView visualization code”, 2014, <http://www.paraview.org>.
- [Parks et al. 2012] M. L. Parks, D. J. Littlewood, J. A. Mitchell, and S. A. Silling, “Peridigm users’ guide v1.0.0”, SAND report 2012-7800, Sandia National Laboratories, September 2012, <http://www.osti.gov/scitech/servlets/purl/1055619>.

- [Peridigm 2014] J. Aidun, J. T. Foster, D. J. Littlewood, J. A. Mitchell, M. L. Parks, S. A. Silling, and D. Turner, “Peridigm”, 2014, <http://peridigm.sandia.gov>.
- [Seleson and Parks 2011] P. Seleson and M. L. Parks, “On the role of the influence function in the peridynamic theory”, *J. Multiscale Comput. Eng.* **9**:6 (2011), 689–706.
- [Silling 2000] S. A. Silling, “Reformulation of elasticity theory for discontinuities and long-range forces”, *J. Mech. Phys. Solids* **48**:1 (2000), 175–209.
- [Silling and Askari 2005] S. A. Silling and E. Askari, “A meshfree method based on the peridynamic model of solid mechanics”, *Comput. Struct.* **83**:17–18 (2005), 1526–1535.
- [Silling and Lehoucq 2010] S. A. Silling and R. B. Lehoucq, “Peridynamic theory of solid mechanics”, *Adv. Appl. Mech.* **44** (2010), 73–168.
- [Silling et al. 2007] S. A. Silling, M. Epton, O. Weckner, J. Xu, and E. Askari, “Peridynamic states and constitutive modeling”, *J. Elasticity* **88**:2 (2007), 151–184.
- [Tupek and Radovitzky 2014] M. R. Tupek and R. Radovitzky, “An extended constitutive correspondence formulation of peridynamics based on nonlinear bond-strain measures”, *J. Mech. Phys. Solids* **65** (2014), 82–92.
- [Tupek et al. 2013] M. R. Tupek, J. J. Rimoli, and R. Radovitzky, “An approach for incorporating classical continuum damage models in state-based peridynamics”, *Comput. Methods Appl. Mech. Eng.* **263** (2013), 20–26.

Received 2 Oct 2014. Revised 9 Feb 2015. Accepted 12 Mar 2015.

JOHN A. MITCHELL: [jamitch@sandia.gov](mailto:jamitch@sandia.gov)

Multiscale Science, Sandia National Laboratories, P.O. Box 5800, MS 1322, Albuquerque, NM 87185-1322, United States

STEWART A. SILLING: [sasilli@sandia.gov](mailto:sasilli@sandia.gov)

Multiscale Science, Sandia National Laboratories, P.O. Box 5800, MS 1322, Albuquerque, NM 87185-1322, United States

DAVID J. LITTLEWOOD: [djlittl@sandia.gov](mailto:djlittl@sandia.gov)

Multiscale Science, Sandia National Laboratories, PO Box 5800, MS 1322, Albuquerque, NM 87185-1322, United States



## PERIDYNAMICS ANALYSIS OF THE NANOSCALE FRICTION AND WEAR PROPERTIES OF AMORPHOUS CARBON THIN FILMS

SAYNA EBRAHIMI, DAVID J. STEIGMANN AND KYRIAKOS KOMVOPOULOS

State-based peridynamics theory was used to study the nanoscale friction and wear behavior of thin films of amorphous carbon used as protective overcoats in hard-disk drives. Numerical results of the coefficient of friction and wear depth are shown to be in good agreement with published experimental results. Although long-range forces are not considered in the analysis, the results indicate that the present approach yields fairly accurate estimates of the coefficient of friction and wear depth for films of thickness larger than 10 nm and a grid size of 1.6 nm. The results of this study demonstrate that peridynamics theory can be used to analyze various nanoscale friction and wear phenomena without being limited by the excessive computational time and convergence difficulties encountered with traditional numerical techniques, such as the finite element method.

### 1. Introduction

Thin films are used as protective overcoats in a wide range of applications where the tribological properties of proximal surfaces are of paramount importance to the functionality and endurance of mechanical components possessing contact interfaces. For example, thin films of amorphous carbon (*a*-C) play a critical role in the reliability and performance of magnetic recording devices because they protect the magnetic head and hard disk surfaces against mechanical wear during intermittent contact and inhibit corrosion of the magnetic medium of the hard disk. Because of the extremely small *a*-C film thickness and the occurrence of head-disk surface interactions at nanoscopic surface protrusions (asperities), knowledge of the nanoscale tribological and mechanical properties of thin *a*-C films is of high technological importance.

The nanomechanical/tribological properties of *a*-C films are greatly affected by the type of carbon atom hybridization and the hydrogen content. Other elements (e.g., Si, N, B, F, and O) can be added to modify the electromechanical properties of *a*-C films [Charitidis 2010]. The structure and elemental content of *a*-C films strongly depend on the intricacies of the deposition process, which controls film nucleation and growth [Lifshitz 1996; Grill 1999; Charitidis 2010]. Thus, small variations in the deposition conditions may result in vastly different film properties. In view of the time-consuming experimental techniques available for nanoscale mechanical and tribological testing of thin films, alternative approaches must be used to examine the effects of structural changes on the resulting film properties.

High contents of tetrahedral carbon atom hybridization ( $sp^3$ ) characterize the structure of *a*-C films exhibiting diamond-like behavior, whereas high contents of trigonal carbon atom hybridization ( $sp^2$ )

---

Komvopoulos is the corresponding author.

*Keywords:* state-based peridynamics, friction, wear, thin films.

generally produce graphite-like film behavior. A continuum description does not account for local differences in nanostructure [Luan and Robbins 2005], whereas molecular dynamics (MD) is limited by high computational cost, model size, and type of potential function used to describe atomic interaction [Alder and Wainwright 1959]. Therefore, nonlocal computational approaches, which are not subjected to the aforementioned restrictions, must be developed to enhance the study of the interdependence of structure and material behavior at the nanoscale.

Peridynamics [Silling 2000] is a relatively new theory which promises to bridge the material gap in computational mechanics. Peridynamics is a continuum version of MD which uses integral equations of motion to offset complexities associated with material discontinuities (e.g., defects, edges, and sharp corners) instead of the conventional partial differential equations used in classical mechanics and does not rely on *a priori* assumed defect or damage criteria (e.g., crack growth direction). Because of the mathematical simplicity and computational affordability, peridynamics has been used to analyze various computationally intense problems, such as dynamic fracture in brittle [Ha and Bobaru 2010; 2011; Bobaru and Hu 2012; Liu and Hong 2012; Lipton 2014] and composite [Askari et al. 2006; Xu et al. 2008; Kilic et al. 2009; Hu et al. 2011; 2012] materials, multiscale damage [Askari et al. 2008; Alali and Lipton 2012], and damage of nanofiber networks, including long-range effects of van der Waals forces on nanofiber deformation [Bobaru and Silling 2004; Silling and Bobaru 2005; Bobaru 2007; Bobaru et al. 2011]. Moreover, peridynamics has been used in failure analyses dealing with thin film cracking in electronic packaging [Agwai et al. 2008; 2009; 2011] and also in conjunction with atomic force microscopy and nanoindentation techniques to determine the mechanical properties of ultrathin films [Celik et al. 2009].

The objective of this study is to introduce a two-dimensional (2D) peridynamics analysis of the nanotribological behavior of thin *a*-C films. Simulation results of the coefficient of friction and depth of wear track due to a rigid (diamond) tip sliding against *a*-C films of different thickness and nanomechanical properties are presented and compared with experimental results of a previous study [Lu and Komvopoulos 2001] to validate the accuracy of the developed peridynamics models.

## 2. State-based peridynamics formulation

Peridynamics is a theory of mechanics which uses a finite number of particles to discretize a deformable solid body. Particle interaction is modeled within a predefined distance, referred to as the horizon. Because the governing equations in peridynamics are integrals of particle motion, material discontinuities and high strain gradients do not present computational obstacles. The main peridynamics approaches can be classified in bond-based and state-based formulations. Bond-based peridynamics presumes the existence of a pairwise force function between any two particles, which is independent of the deformation associated with other particles [Silling 2000] and has been developed for a Poisson's ratio of 0.33 and 0.25 for 2D and three-dimensional (3D) problems, respectively. State-based peridynamics relies on a more general theory, which uses a more comprehensive constitutive model derived based on force- and deformation-state concepts [Silling et al. 2007]. To obtain the force state at each particle, the deformation (stretching) of all bonds within the horizon of each particle are considered without assuming a specific value of the Poisson's ratio. Similarities between state-based peridynamics and continuum theory have been reported [Silling et al. 2007; Lehoucq and Silling 2008], including the convergence of state-based peridynamics to classical elasticity theory [Silling and Lehoucq 2008].

The general 3D peridynamics equation of motion is given by [Silling et al. 2007]

$$\rho(\mathbf{x}_i)\ddot{\mathbf{u}}(\mathbf{x}_i, t) = \int_{\mathcal{H}} (\underline{\mathbf{T}}[\mathbf{x}_i, t]\langle \mathbf{x}_j - \mathbf{x}_i \rangle - \underline{\mathbf{T}}[\mathbf{x}_j, t]\langle \mathbf{x}_i - \mathbf{x}_j \rangle) dV_j + \mathbf{b}(\mathbf{x}_i, t), \quad (1)$$

where  $\rho$  is the mass density,  $\mathbf{x}_i$  and  $\mathbf{x}_j$  are the position vectors of particles  $i$  and  $j$ , respectively,  $\mathbf{u}$  is the displacement field,  $\mathcal{H}$  is the domain of the spherical horizon with a radius  $\delta$ ,  $\underline{\mathbf{T}}$  is the force vector state field,  $\mathbf{b}$  is the body force density field,  $t$  is the time, and  $dV_j$  is the volume of particle  $j$ . In the present analysis, the deformable materials are assumed to be ordinary, implying that the force between two particles acts in the bond direction.

For ordinary materials, the force vector is given by [Silling et al. 2007]

$$\underline{\mathbf{T}} = \underline{t}\underline{\mathbf{M}}, \quad (2)$$

where  $\underline{t}$  is the scalar force state and  $\underline{\mathbf{M}}$  is the deformation direction vector. In the linear peridynamics solid (LPS) model, the force scalar state is defined by [Silling et al. 2007]

$$\underline{t} = \frac{3K\theta[\mathbf{x}, t]}{m[\mathbf{x}]} \underline{\omega}\langle \underline{\boldsymbol{\xi}} \rangle \underline{x}\langle \underline{\boldsymbol{\xi}} \rangle + \frac{15G}{m[\mathbf{x}]} \underline{\omega}\langle \underline{\boldsymbol{\xi}} \rangle \underline{e}^d[\mathbf{x}, t], \quad (3)$$

where  $K$  and  $G$  are the bulk and shear modulus, respectively,  $\theta$  is the dilatation,  $m$  is the weighted volume,  $\underline{e}^d$  is the deviatoric component of the extension scalar state  $\underline{e}$ , and  $\underline{\omega}$  is the influence function. These parameters can be defined, following [Silling et al. 2007], as:

$$\theta[\mathbf{x}, t] = \frac{3}{m[\mathbf{x}]} \int_{\mathcal{H}} \underline{\omega}\langle \underline{\boldsymbol{\xi}} \rangle \underline{x}\langle \underline{\boldsymbol{\xi}} \rangle \underline{e}[\mathbf{x}, t]\langle \underline{\boldsymbol{\xi}} \rangle dV, \quad (4)$$

$$m[\mathbf{x}] = \int_{\mathcal{H}} \underline{\omega}\langle \underline{\boldsymbol{\xi}} \rangle \underline{x}\langle \underline{\boldsymbol{\xi}} \rangle \underline{x}\langle \underline{\boldsymbol{\xi}} \rangle dV, \quad (5)$$

$$\underline{e}[\mathbf{x}, t]\langle \underline{\boldsymbol{\xi}} \rangle = \|\underline{\boldsymbol{\xi}} + \underline{\boldsymbol{\eta}}\| - \|\underline{\boldsymbol{\xi}}\|, \quad (6)$$

$$\underline{e}^d[\mathbf{x}, t]\langle \underline{\boldsymbol{\xi}} \rangle = \underline{e}[\mathbf{x}, t]\langle \underline{\boldsymbol{\xi}} \rangle - \underline{e}^i[\mathbf{x}, t]\langle \underline{\boldsymbol{\xi}} \rangle = \underline{e}[\mathbf{x}, t]\langle \underline{\boldsymbol{\xi}} \rangle - \frac{1}{3}\theta[\mathbf{x}, t]\underline{x}\langle \underline{\boldsymbol{\xi}} \rangle, \quad (7)$$

where  $\underline{\boldsymbol{\xi}} = \mathbf{x}_j - \mathbf{x}_i$  is the relative position vector between particles  $i$  and  $j$  in the reference configuration and  $\underline{\boldsymbol{\eta}} = \mathbf{u}(\mathbf{x}_j, t) - \mathbf{u}(\mathbf{x}_i, t)$  is the relative displacement vector between particles  $i$  and  $j$  at time  $t$ .

Because of the highly disordered structure of  $a$ -C films [Charitidis 2010], they can be modeled as isotropic materials with an influence function  $\underline{\omega}\langle \underline{\boldsymbol{\xi}} \rangle = 1/\|\underline{\boldsymbol{\xi}}\|$ , as suggested elsewhere [Parks et al. 2010].

Damage is assumed to occur when bond stretching exceeds a predefined critical stretch  $s_c$ , given by [Silling and Askari 2005; Ha and Bobaru 2011]

$$s_c = \sqrt{4\pi G_I/9E\delta}, \quad (8)$$

where  $G_I$  is the critical energy release rate corresponding to the mode I stress intensity factor  $K_I$  (i.e.,  $G_I = K_I^2/E'$ , where  $E' = E$  (plane stress) or  $E/(1 - \nu^2)$  (plane strain)). Equation (8) indicates that  $s_c$  is a function of the material properties and the characteristic length scale of the analyzed body, i.e., the horizon radius  $\delta$ .

Damage at a given material point (particle) is defined as the ratio of the number of broken bonds to the total number of bonds  $D$ . Because  $D$  assumes values between 0 (no damage) and 1 (full damage)

[Silling and Askari 2005], it can be used as a damage index to characterize the extent of material removal ( $D = 1$ ) and the evolution of permanent damage ( $0 < D < 1$ ) in the wear model.

### 3. Body discretization and computational details

To obtain a solution for the 2D version of (1), the body is discretized by a uniform grid ( $\Delta x = \Delta y$ ) and the integral is replaced by a summation including all interacting particles within the horizon of a given particle. Thus, (1) can be expressed as

$$\rho_i \ddot{\mathbf{u}}_i^n = \sum_{j=1}^{N_{\mathcal{H}}} \mathcal{F}(\mathbf{x}_i^n, \mathbf{x}_j^n, \mathbf{x}_i^{n-1}, \mathbf{x}_j^{n-1}) V_j + \mathbf{b}_i^n, \quad (9)$$

where the superscripts denote the time step and  $N_{\mathcal{H}}$  is the total number of particles interacting with the particle of interest within its horizon. Time integration of (9) using the central difference method yields the position and velocity of each particle at time step  $(n + 1)$ . The nodal area of the particles lying on the horizon boundaries is accordingly modified [Parks et al. 2008].

In addition to the force vector state obtained from (2), short-range forces are also included in the present analysis by introducing a short-range particle interaction distance

$$d_{pi} = \min\{0.9\|\mathbf{x}_p - \mathbf{x}_i\|, 1.35(r_p + r_i)\},$$

where  $\mathbf{x}_p$  and  $r_p$  are the position and radius of particle  $p$  in the vicinity of particle  $i$ , respectively, and  $r_i$  is the radius of particle  $i$ , which is set equal to one-half of the grid size (i.e.,  $r_i = \frac{1}{2}\Delta x$ ) [Parks et al. 2010]. Long-range forces may also have a strong effect on nanoscale deformation and, despite the continuum nature of peridynamics, it is possible to incorporate potential force functions from MD analysis in the force state of peridynamics [Silling and Bobaru 2005; Bobaru 2007; Bobaru et al. 2011]. However, for a separation distance of 2 nm, long-range forces reach  $\sim 10\%$  of their peak values [Bobaru 2007]. Consequently, because the grid size used in the present analysis is less than 2 nm (see Section 4 for details), long-range forces are not considered for simplicity.

### 4. Peridynamics friction and wear models

State-based peridynamics friction and wear models are presented in this section and simulation results are compared with published experimental results of the nanoscale tribological properties of thin  $a$ -C films [Lu and Komvopoulos 2001] to illustrate the validity of the developed models. A 2D analysis of the sliding process is valid provided the depth of penetration is significantly less than the width of the resulting plowing (wear) track [Komvopoulos et al. 1985]. Since in all simulation cases the ratio of the wear depth to the wear track width is less than 0.1, a 2D peridynamics analysis of the sliding friction and wear processes is justifiable. All simulations were performed with a custom-made peridynamics code written in Fortran 90/95 and executed on a Linux platform with a quad-core 2.33 GHz Intel Xeon E5345 CPU.

**4.1. Friction model.** Figure 1 schematically shows a rigid spherical tip of radius  $R$  under normal load  $P$ , which is sliding against a thin  $a$ -C film firmly attached to a thick Si substrate. Because of the high elastic modulus of diamond, in all numerical simulations the tip is modeled as rigid. The center of the tip is initially set at a distance equal to  $R - \frac{1}{2}\Delta x$  from the film surface. Short-range forces inhibit the



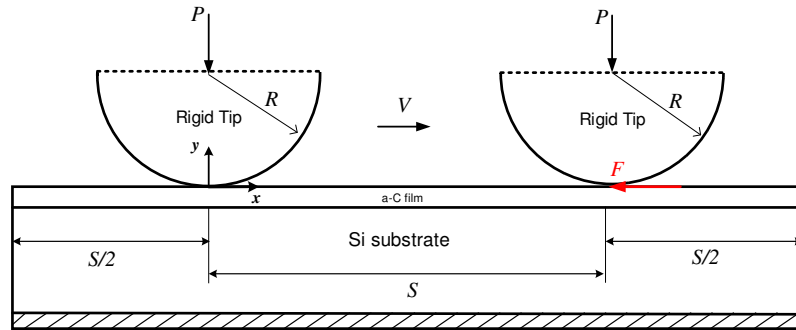


**Figure 1.** Schematic of peridynamics friction model of a spherical diamond (rigid) tip sliding at a constant velocity  $V$  against a thin  $a$ -C film, which is firmly adhered to a thick Si substrate. The tip slides from left ( $x/S = 0$ ) to right ( $x/S = 1$ ) through a total distance  $S$ . The shaded layer at the bottom of the substrate is modeled as rigid. The coefficient of friction is obtained as the ratio of the computed tangential (friction) force  $F$ , which opposes tip sliding, and the applied normal load  $P$ . The film thickness and the tip radius are not drawn to scale.

development of particle-particle distances less than  $d_{pi}$ , defined in Section 3. Both film and substrate materials are assumed to be isotropic, predominantly exhibiting brittle behavior. The elastic properties, density, and critical stretch of the Si substrate are given in Table 1, whereas the thickness, root-mean-square (rms) roughness, elastic properties, and density of all  $a$ -C films examined in this study are given

|          |                                      |                                |   |                                 |
|----------|--------------------------------------|--------------------------------|---|---------------------------------|
| Material | Elastic modulus <sup>(a)</sup> (GPa) | Poisson’s ratio <sup>(a)</sup> | Density <sup>(a)</sup> (g/cm <sup>3</sup> ) | Critical stretch <sup>(b)</sup> |
| Silicon  | 132                                  | 0.278                          | 2.329                                       | 0.01                            |

**Table 1.** Mechanical properties and critical stretch of Si substrate. <sup>(a)</sup>Ref. [Lu and Komvopoulos 2001]. <sup>(b)</sup>Ref. [Agwai et al. 2011].

| Film # | Thickness <sup>(a)</sup> (nm) | Roughness, <sup>(a)</sup> rms (nm) | Elastic modulus <sup>(a)</sup> (GPa) | Poisson’s ratio <sup>(a)</sup> | Density (g/cm <sup>3</sup> ) | # particles (film) | # particles (substrate) |
|--------|-------------------------------|------------------------------------|--------------------------------------|--------------------------------|------------------------------|--------------------|-------------------------|
| 1      | 31                            | 0.51                               | 105                                  | 0.278                          | 3.139                        | 5000 × 19          | 5000 × 606              |
| 2      | 34                            | 0.20                               | 197                                  | 0.278                          | 4.058                        | 5000 × 21          | 5000 × 604              |
| 3      | 39                            | 0.15                               | 206                                  | 0.278                          | 4.143                        | 5000 × 24          | 5000 × 601              |
| 4      | 53                            | 0.27                               | 139                                  | 0.278                          | 3.500                        | 5000 × 33          | 5000 × 592              |
| 5      | 59                            | 0.23                               | 101                                  | 0.278                          | 3.094                        | 5000 × 36          | 5000 × 589              |
| 6      | 69                            | 0.15                               | 192                                  | 0.278                          | 4.017                        | 5000 × 43          | 5000 × 582              |
| 7      | 95                            | 0.24                               | 155                                  | 0.278                          | 3.661                        | 5000 × 59          | 5000 × 566              |

**Table 2.** Thickness, roughness, elastic properties, and density of  $a$ -C films and number of film and substrate particles used in the peridynamics friction analysis. <sup>(a)</sup>Ref. [Lu and Komvopoulos 2001].

in Table 2. The film density was calculated from the relation  $\rho = 1.37 + E^{2/3}/44.65$ , where  $\rho$  and  $E$  are given in  $\text{g/cm}^3$  and GPa, respectively [Casiraghi et al. 2007]. The number of particles used to discretize the film and substrate media in each friction simulation are also given in Table 2. In all friction simulations, the tip radius is equal to  $20 \mu\text{m}$ .

To enhance the convergence, load-control sliding experiments were simulated by the following method. First, the normal load was incrementally applied using several time steps until the desired load (in the range of  $50\text{--}400 \mu\text{N}$ ) was reached. This incremental loading procedure is similar (though faster) to that used in the experimental study [Lu and Komvopoulos 2001]. Subsequently, the tip was traversed in the  $x$ -direction at a constant velocity  $V = 0.4 \mu\text{m/s}$  through a total distance  $S = 4 \mu\text{m}$ . To avoid boundary effects on the friction results, the distance of the left and right boundaries of the discretized domain from the initial ( $x/S = 0$ ) and final ( $x/S = 1$ ) tip positions was set equal to  $S/2$  (Figure 1). An adaptive dynamic relaxation (ADR) method similar to that presented in [Kilic and Madenci 2010], which was accordingly modified for state-based formulation, was used in the friction analysis. The time step in the ADR analysis of friction was set equal to  $0.01 \text{ s}$ . Artificial damping was used in the equations of particle and tip motion. For the calculation of the damping coefficient of the rigid tip, the stiffness was increased by a factor of 10 to account for the rigidity of the tip. Similar to the friction experiments reported in [Lu and Komvopoulos 2001], only elastic deformation is modeled in the friction simulations, i.e., irreversible damage such as bond breakage is not included in the friction model. The initial boundary conditions used for time integration are zero displacements and velocities in all directions at all particles and the tip center. Films of thickness larger than  $10 \text{ nm}$  are examined because the grid size is less than  $2 \text{ nm}$ . In addition, because the rms roughness of the films (in the range of  $0.15\text{--}0.51 \text{ nm}$  [Lu and Komvopoulos 2001]) is significantly smaller than the grid size, both film and substrate media are modeled as perfectly smooth.

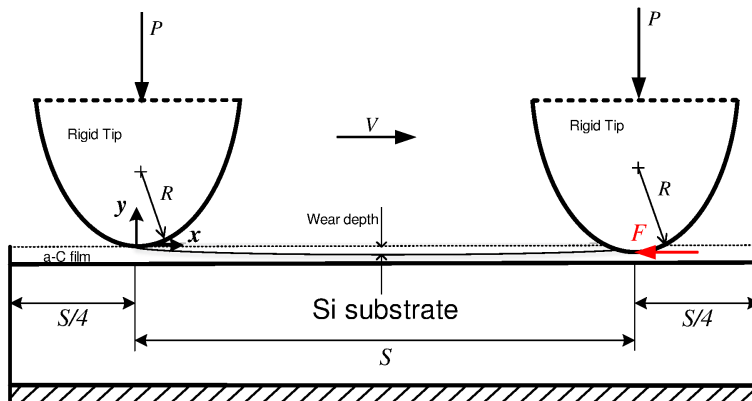


**Figure 2.** Schematic of peridynamics wear model of a sharp conospherical diamond (rigid) tip under a normal load  $P$  sliding at a constant velocity  $V$  and plowing through a thin  $a\text{-C}$  film, which is firmly attached to a thick Si substrate. The tip slides against the film surface from left ( $x/S = 0$ ) to right ( $x/S = 1$ ) through a total distance  $S$ . The shaded layer at the bottom of the substrate is modeled as rigid. The film thickness and the tip radius are not drawn to scale.

| Film # | Thickness <sup>(a)</sup><br>(nm) | Roughness, <sup>(a)</sup><br>rms (nm) | Elastic<br>modulus <sup>(a)</sup> (GPa) | Poisson's<br>ratio <sup>(a)</sup> | Density<br>(g/cm <sup>3</sup> ) | Critical<br>stretch | # particles<br>(film) | # particles<br>(substrate) |
|--------|----------------------------------|---------------------------------------|---|-----------------------------------|---------------------------------|---------------------|-----------------------|----------------------------|
| 8      | 17                               | 0.19                                  | 113                                     | 0.278                             | 3.230                           | 0.0125              | 937 × 10              | 937 × 615                  |
| 9      | 22                               | 0.18                                  | 203                                     | 0.278                             | 4.115                           | 0.0125              | 937 × 13              | 937 × 612                  |
| 10     | 10                               | 0.20                                  | 226                                     | 0.278                             | 4.317                           | 0.0125              | 937 × 6               | 937 × 619                  |

**Table 3.** Thickness, roughness, elastic properties, density, and critical stretch of *a*-C films and number of film and substrate particles used in the peridynamics wear analysis. <sup>(a)</sup>Ref. [Lu and Komvopoulos 2001].

**4.2. Wear model.** Figure 2 shows a schematic of the wear model consisting of a sharp rigid (diamond) conospherical probe with a tip radius  $R$  plowing through an *a*-C film, which is firmly attached to a thick Si substrate. After incremental loading of the probe to the desired normal load  $P = 10 \mu\text{N}$  (load-control simulations) at  $x/S = 0$ , the probe was traversed in the  $x$ -direction at a constant velocity  $V = 4 \mu\text{m/s}$  through a total distance  $S = 1 \mu\text{m}$  and was finally unloaded at  $x/S = 1$ . To avoid boundary effects on the wear results, the distance of the left and right boundaries of the discretized domain from the initial ( $x/S = 0$ ) and final ( $x/S = 1$ ) tip positions was set equal to  $S/4$ . The thickness, rms roughness, elastic properties, density, and critical stretch of the *a*-C films analyzed with the wear model and the number of particles used to discretize the film and the substrate are given in Table 3. In all wear simulations, the probe tip radius is equal to  $1 \mu\text{m}$  and the initial displacements and velocities of the tip and all particles are set equal to zero. The previously mentioned ADR technique [Kilic and Madenci 2010] with a time step of 0.001 s was also used in the wear analysis.

In the wear simulations, irreversible damage in the wake of the plowing tip comprises bond breakage. Therefore, a critical bond stretch was used to capture bond breakage. In addition to the critical bond stretch of the substrate (Table 1) and film (Table 3) materials, a conservative estimate of the critical bond stretch of the *a*-C/Si interface was obtained from (8), where  $E$  is the elastic modulus of the substrate and  $G_I$  is the strain energy release rate due to indentation of the film by a conospherical diamond indenter, which is equal to  $0.037 \text{ J/m}^2$  [Marshall and Evans 1984; Volinsky et al. 2002]. Using (8), the critical stretch of the *a*-C/diamond interface was found to be equal to 0.007. The depth of the wear track on the film surface was determined by calculating the average displacement of irreversibly deformed ( $0 < D < 1$ ) particle layers of the film medium along the plowing path after the unloading of the probe tip.

## 5. Results and discussion

Simulation results obtained with the peridynamics friction and wear models are presented in this section in conjunction with experimental results from a previous experimental study [Lu and Komvopoulos 2001] to validate both peridynamics models.

**5.1. Coefficient of friction.** The coefficient of friction is defined as the ratio of the tangential (friction) force and the applied normal load. At each time step, the friction force was calculated as the tangential component of the total force generated by the sliding action of the tip; thus, a coefficient of friction was computed at each time step. An overall coefficient of friction was calculated for each *a*-C film as the average of all friction coefficient data.

| $\delta$ (nm) | $m$ | Coefficient of friction |
|---------------|-----|-------------------------|
| 8             | 3.5 | 0.1421                  |
| 8             | 4.0 | 0.1526                  |
| 8             | 4.5 | 0.1567                  |
| 8             | 5.0 | 0.1591                  |
| 8             | 5.5 | 0.1456                  |

**Table 4.** Coefficient of friction results from  $m$ -convergence tests.

Similar to local numerical methods, determining an appropriate grid size in peridynamics requires convergence testing [Bobaru et al. 2009; Bobaru and Hu 2012]. Among various convergence tests, the  $m$ -convergence test was used in the peridynamics friction model to calculate the coefficient of friction. The  $\delta$ -convergence test was not used because the decrease of the horizon radius to zero (i.e., no length scale) should yield solutions converging to classical elasticity solutions, which not only do not hold at the nanoscale [Luan and Robbins 2005] but are also length-scale independent. In the  $m$ -convergence test,  $\delta$  is fixed whereas  $m = \delta/\Delta x$  is gradually increased until the solution converges to an exact nonlocal peridynamics solution obtained for fixed  $\delta$  [Bobaru et al. 2009]. Table 4 shows results from  $m$ -convergence tests for film #7 (Table 2),  $P = 400 \mu\text{N}$ ,  $\delta = 8 \text{ nm}$ , and  $m$  in the range of 3.5–5.5. The coefficient of friction diverges with the increase of  $m$  from 5.0 to 5.5, suggesting an increasing effect of long-range forces. Therefore,  $m = 5.0$  (i.e.,  $\Delta x = 1.6 \text{ nm}$ ) was used in the present peridynamics analysis. Because the focus of this study is the analysis of thin  $a$ -C films, the convergence test was only carried out for the  $a$ -C film.

Table 5 shows a comparison between peridynamics and experimental results of the coefficient of friction of  $a$ -C films with different thickness and rms roughness for  $P$  in the range of 50–400  $\mu\text{N}$ . Even though the films were modeled to have ideally smooth surfaces, the agreement between numerical and experimental results is very good. It is noted that the experimental coefficients of friction represent averages of 300 data acquired along the entire sliding track and that the scatter in the measurements increases with the decrease of the normal load, yielding standard deviation values in the range of 0.05–0.08 [Lu and Komvopoulos 2001].

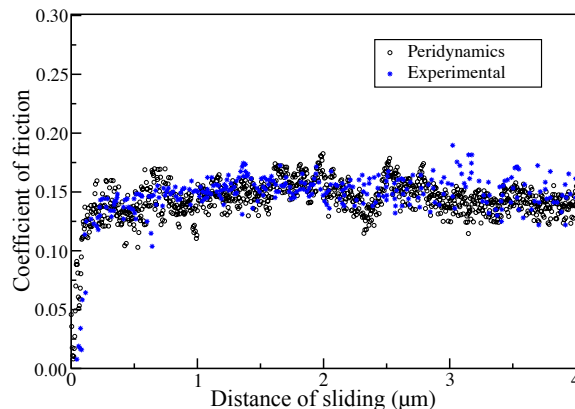


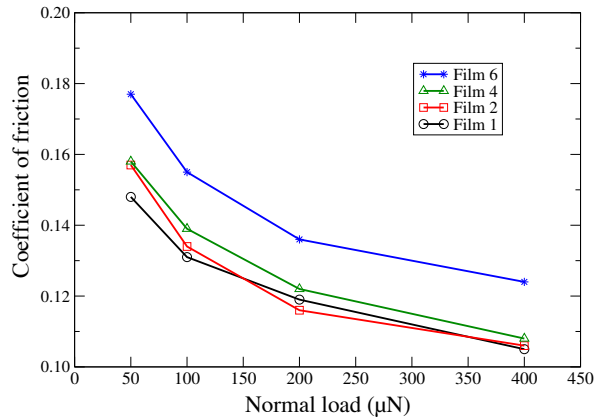
**Figure 3.** Peridynamics and experimental results [Lu and Komvopoulos 2001] of the coefficient of friction of an  $a$ -C film versus sliding distance for  $P = 400 \mu\text{N}$ .

| Film # | Thickness <sup>(a)</sup><br>(nm) | Roughness <sup>(a)</sup> ,<br>rms (nm) | Normal load <sup>(a)</sup><br>( $\mu\text{N}$ ) | Coeff. of friction<br>(peridynamics) | Coeff. of friction<br>(experimental) <sup>(a)</sup> |
|--------|----------------------------------|--|---|--------------------------------------|---|
| 1      | 31                               | 0.51                                   | 50  | 0.132                                | 0.16  |
|        |                                  |  | 100   | 0.127                                | 0.14  |
|        |                                  |  | 200   | 0.115                                | 0.13  |
|        |                                  |  | 400   | 0.108                                | 0.12  |
| 2      | 34                               | 0.20                                   | 50  | 0.149                                | 0.17  |
|        |                                  |  | 100   | 0.128                                | 0.15  |
|        |                                  |  | 200   | 0.110                                | 0.14  |
|        |                                  |  | 400   | 0.099                                | 0.12  |
| 3      | 39                               | 0.15                                   | 50  | 0.156                                | 0.18  |
|        |                                  |  | 100   | 0.142                                | 0.16  |
|        |                                  |  | 200   | 0.121                                | 0.14  |
|        |                                  |  | 400   | 0.115                                | 0.13  |
| 4      | 53                               | 0.27                                   | 50  | 0.145                                | 0.17  |
|        |                                  |  | 100   | 0.127                                | 0.15  |
|        |                                  |  | 200   | 0.118                                | 0.13  |
|        |                                  |  | 400   | 0.102                                | 0.12  |
| 5      | 59                               | 0.23                                   | 50  | 0.140                                | 0.17  |
|        |                                  |  | 100   | 0.122                                | 0.15  |
|        |                                  |  | 200   | 0.114                                | 0.14  |
|        |                                  |  | 400   | 0.105                                | 0.12  |
| 6      | 69                               | 0.15                                   | 50  | 0.169                                | 0.18  |
|        |                                  |  | 100   | 0.148                                | 0.16  |
|        |                                  |  | 200   | 0.129                                | 0.14  |
|        |                                  |  | 400   | 0.121                                | 0.13  |
| 7      | 95                               | 0.24                                   | 50  | 0.147                                | 0.17  |
|        |                                  |  | 100   | 0.108                                | 0.15  |
|        |                                  |  | 200   | 0.115                                | 0.13  |
|        |                                  |  | 400   | 0.108                                | 0.12  |

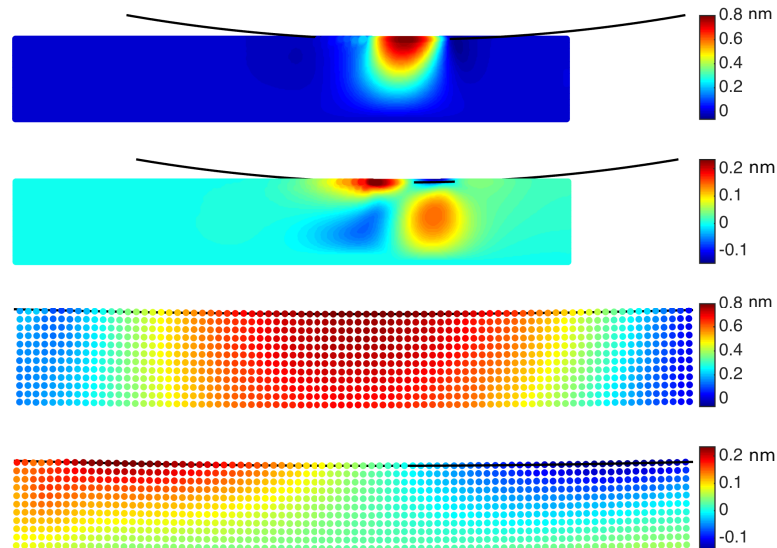
**Table 5.** Peridynamics and experimental results of the coefficient of friction of *a*-C films versus film thickness, roughness, and normal load. <sup>(a)</sup>Ref. [Lu and Komvopoulos 2001].

Figure 3 shows a comparison between peridynamics and experimental results of a typical coefficient of friction response for a 400  $\mu\text{N}$  normal load. The peridynamics solution closely follows the experimental trend, showing good agreement with the average response of the scattered experimental data. Figure 3 and Table 5 illustrate the validity of the peridynamics friction model and provide justification for the modeling assumptions.

Figure 4 shows peridynamics results of the steady-state coefficient of friction (obtained as the average of all numerical data in the 0–4  $\mu\text{m}$  sliding distance range) versus normal load for different *a*-C films



**Figure 4.** Peridynamics results of the coefficient of friction of various *a*-C films versus normal load.



**Figure 5.** Contour maps of *y*-displacement (top image) and *x*-displacement (second image) of particles in film #4 for  $x/S = 1$ , and corresponding high-magnification contour maps (bottom two images) showing the displacement of particles in the near-surface region of the film adjacent to the contact interface with the sliding rigid tip.

(Table 2). All peridynamics solutions show that the coefficient of friction decreases with increasing normal load. This trend is in good agreement with experimental findings and is attributed to the inverse proportionality of the coefficient of friction of predominantly elastically deformed surfaces to the cubic root of the normal load [Lu and Komvopoulos 2001].

The top two images in Figure 5 show *y*- and *x*-displacement contour maps, respectively, for  $x/S = 1$ . High-magnification views of the particle displacements under the tip, shown in the bottom two images in Figure 5, provide insight into the highly stressed region of the film underneath the loaded tip. However,

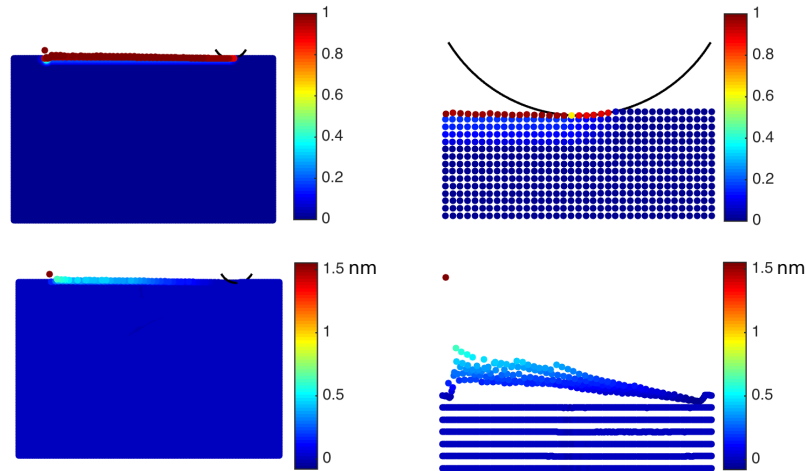


**Figure 6.** Top left: damage contour map of film #9 after tip unloading (damage index  $D = 1$  corresponds to particles with all their bonds broken). Top right: corresponding high-magnification damage contour map of damaged particle layers in the near-surface region of the film. Bottom left:  $y$ -displacement contour map of damaged film #9 after tip unloading. Bottom right: corresponding high-magnification contour map showing the  $y$ -displacement of particles adjacent to the contact interface with the plowing rigid tip.

the zero displacements in the wake of the tip (top two images in Figure 5) reveal a full recovery of the unloaded film region. Importantly, despite the fully elastic behavior of the film/substrate medium and the adhesionless tip/film contact interface, the instantaneous coefficient of friction is not zero. Not only is this finding in contrast with classical friction theories, which attribute friction to irreversible deformation, but also reveals that frictionless contact is practically impossible.

**5.2. Wear depth.** To validate the peridynamics wear model, the experimentally measured depths of wear tracks produced on  $a$ -C film surfaces by a sharp conospherical rigid tip [Lu and Komvopoulos 2001] are compared with numerical results. Figure 6 (top left) shows damage at the film surface due to sliding contact interaction. A damage index  $D = 1$  is indicative of bond breakage. As the rigid tip plows through the film, the particles near the surface are permanently displaced from their original positions. Figure 6 (top right) shows a close-up view of the deformed grid below the tip, revealing much more pronounced damage in the near-surface region of the  $a$ -C film adjacent to the sharp tip. Further insight into nanoscale film wear is provided by the  $y$ -displacement contour map and the close-up view of the near-surface damaged particle layers shown in Figure 6 (bottom left and right, respectively).

The wear depth is defined as the average displacement of all particles with partly broken bonds (i.e.,  $0 < D < 1$ ), located relatively far from the initial ( $x/S = 0$ ) and final ( $x/S = 1$ ) tip positions. The displacements of particles with  $D = 1$  were not included in the calculation of the wear depth. Table 6 shows numerical and experimental results of the wear depth of three  $a$ -C films for  $P = 10 \mu\text{N}$ . For films #8 and #9 the agreement is very good ( $\sim 4\%$  error), whereas for film #10 the agreement is fair, presumably because of the rougher film surface and errors due to the small film thickness (10 nm) relative to the grid size ( $\approx 1.6$  nm).

| Film # | Thickness (nm) | Roughness, <sup>(a)</sup> rms (nm) | Normal load ( $\mu\text{N}$ ) | Wear depth (nm) (peridynamics) | Wear depth (nm) (experimental) <sup>(a)</sup> |
|--------|----------------|------------------------------------|-------------------------------|--------------------------------|---|
| 8      | 17             | 0.19                               | 10                            | 0.730                          | 0.76  |
| 9      | 22             | 0.18                               | 10                            | 0.391                          | 0.40  |
| 10     | 10             | 0.20                               | 10                            | 0.161                          | 0.20  |

**Table 6.** Comparison of peridynamics and experimental results of the wear depth of *a*-C films versus film thickness, roughness, and normal load. <sup>(a)</sup>Ref. [Lu and Komvopoulos 2001].

## 6. Conclusions

Nanoscale material behavior can be challenging because classical continuum theory breaks down at the nanoscale, whereas MD analysis is limited to very small scales of limited practical use. Peridynamics promises to bridge the material gap in computational mechanics. In this study, state-based peridynamics theory was used to develop friction and wear models of thin films. Favorable comparisons between peridynamics solutions and experimental results of thin films obtained under identical testing conditions illustrate the validity of the peridynamics friction and wear models developed in this study. Long-range forces were not considered and film surfaces were modeled as perfectly smooth, because the film roughness was significantly less than the grid size. Despite these assumptions, very good agreement was obtained between peridynamics and experimental results of films with thickness equal to or larger than 10 nm. The results of this study demonstrate the potential of peridynamics to capture the nanoscale tribological behavior of thin films, which is difficult (if not impossible) to achieve at the nanoscale with other numerical techniques, such as finite element analysis and the boundary element method.

## Acknowledgments

This research was partially funded by the Computer Mechanics Laboratory, University of California, Berkeley.

## References

- [Agwai et al. 2008] A. Agwai, I. Guven, and E. Madenci, “Peridynamic theory for failure prediction in multilayer thin-film structures of electronic packages”, pp. 1614–1619 in *58th Electronic Components and Technology Conference, IEEE* (Lake Buena Vista, FL, 2008), IEEE Service Center, Piscataway, NJ, 2008.
- [Agwai et al. 2009] A. Agwai, I. Guven, and E. Madenci, “Damage prediction for electronic package drop test using finite element method and peridynamic theory”, pp. 565–569 in *59th Electronic Components and Technology Conference, IEEE* (San Diego, CA, 2009), IEEE Service Center, Piscataway, NJ, 2009.
- [Agwai et al. 2011] A. Agwai, I. Guven, and E. Madenci, “Crack propagation in multilayer thin-film structures of electronic packages using the peridynamic theory”, *Microelectron. Reliab.* **51**:12 (2011), 2298–2305.
- [Alali and Lipton 2012] B. Alali and R. Lipton, “Multiscale dynamics of heterogeneous media in the peridynamic formulation”, *J. Elasticity* **106**:1 (2012), 71–103.
- [Alder and Wainwright 1959] B. J. Alder and T. E. Wainwright, “Studies in molecular dynamics. I: General method”, *J. Chem. Phys.* **31**:2 (1959), 459–466.



- [Askari et al. 2006] E. Askari, J. Xu, and S. Silling, “Peridynamic analysis of damage and failure in composites”, paper no. 2006–88 in *44th AIAA Aerospace Sciences Meeting and Exhibit* (Reno, NV, 2006), American Institute of Aeronautics and Astronautics, Reston, VA, 2006.
- [Askari et al. 2008] E. Askari, F. Bobaru, R. B. Lehoucq, M. L. Parks, S. A. Silling, and O. Weckner, “Peridynamics for multiscale materials modeling”, *J. Phys.: Conf. Ser.* **125**:1 (2008), 012078.
- [Bobaru 2007] F. Bobaru, “Influence of van der Waals forces on increasing the strength and toughness in dynamic fracture of nanofiber networks: A peridynamic approach”, *Model. Simul. Mater. Sci. Eng.* **15**:5 (2007), 397–417.
- [Bobaru and Hu 2012] F. Bobaru and W. Hu, “The meaning, selection, and use of the peridynamic horizon and its relation to crack branching in brittle materials”, *Int. J. Fract.* **176**:2 (2012), 215–222.
- [Bobaru and Silling 2004] F. Bobaru and S. A. Silling, “Peridynamic 3D models of nanofiber networks and carbon nanotube-reinforced composites”, pp. 1565–1570 in *Materials processing and design: Modeling, simulation and applications* (Columbus, OH, 2004), AIP Conf. Proc. **712**, 2004.
- [Bobaru et al. 2009] F. Bobaru, M. Yang, L. F. Alves, S. A. Silling, E. Askari, and J. Xu, “Convergence, adaptive refinement, and scaling in 1D peridynamics”, *Int. J. Numer. Methods Eng.* **77**:6 (2009), 852–877.
- [Bobaru et al. 2011] F. Bobaru, S. A. Silling, and H. Jiang, “Peridynamic fracture and damage modeling of membranes and nanofiber networks”, pp. 976–981 in *Proceedings of the 11th International Conference on Fracture, II* (Turin, Italy, 2005), Curran Associates, New York, 2011.
- [Casiraghi et al. 2007] C. Casiraghi, J. Robertson, and A. C. Ferrari, “Diamond-like carbon for data and beer storage”, *Mater. Today* **10**:1 (2007), 44–53.
- [Celik et al. 2009] E. Celik, E. Oterkus, I. Guven, and E. Madenci, “Mechanical characterization of ultra-thin films by combining AFM nanoindentation tests and peridynamic simulations”, pp. 262–268 in *59th Electronic Components and Technology Conference, IEEE* (San Diego, CA, 2009), IEEE Service Center, Piscataway, NJ, 2009.
- [Charitidis 2010] C. A. Charitidis, “Nanomechanical and nanotribological properties of carbon-based thin films: A review”, *Int. J. Refract. Met. Hard Mater.* **28**:1 (2010), 51–70.
- [Grill 1999] A. Grill, “Diamond-like carbon: State of the art”, *Diam. Relat. Mater.* **8**:2 (1999), 428–434.
- [Ha and Bobaru 2010] Y. D. Ha and F. Bobaru, “Studies of dynamic crack propagation and crack branching with peridynamics”, *Int. J. Fract.* **162**:1-2 (2010), 229–244.
- [Ha and Bobaru 2011] Y. D. Ha and F. Bobaru, “Characteristics of dynamic brittle fracture captured with peridynamics”, *Eng. Fract. Mech.* **78**:6 (2011), 1156–1168.
- [Hu et al. 2011] W. Hu, Y. D. Ha, and F. Bobaru, “Modeling dynamic fracture and damage in a fiber-reinforced composite lamina with peridynamics”, *J. Multiscale Comput. Eng.* **9**:6 (2011), 707–726.
- [Hu et al. 2012] W. Hu, Y. D. Ha, and F. Bobaru, “Peridynamic model for dynamic fracture in unidirectional fiber-reinforced composites”, *Comput. Methods Appl. Mech. Eng.* **217/220** (2012), 247–261.
- [Kilic and Madenci 2010] B. Kilic and E. Madenci, “An adaptive dynamic relaxation method for quasi-static simulations using the peridynamic theory”, *Theor. Appl. Fract. Mech.* **53**:3 (2010), 194–204.
- [Kilic et al. 2009] B. Kilic, A. Agwai, and E. Madenci, “Peridynamic theory for progressive damage prediction in center-cracked composite laminates”, *Compos. Struct.* **90**:2 (2009), 141–151.
- [Komvopoulos et al. 1985] K. Komvopoulos, N. Saka, and N. P. Suh, “The mechanism of friction in boundary lubrication”, *J. Tribol. (ASME)* **107**:4 (1985), 452–462.
- [Lehoucq and Silling 2008] R. B. Lehoucq and S. A. Silling, “Force flux and the peridynamic stress tensor”, *J. Mech. Phys. Solids* **56**:4 (2008), 1566–1577.
- [Lifshitz 1996] Y. Lifshitz, “Hydrogen-free amorphous carbon films: Correlation between growth conditions and properties”, *Diam. Relat. Mater.* **5**:3 (1996), 388–400.
- [Lipton 2014] R. Lipton, “Dynamic brittle fracture as a small horizon limit of peridynamics”, *J. Elasticity* **117**:1 (2014), 21–50.
- [Liu and Hong 2012] W. Liu and J.-W. Hong, “Discretized peridynamics for brittle and ductile solids”, *Int. J. Numer. Methods Eng.* **89**:8 (2012), 1028–1046.

- [Lu and Komvopoulos 2001] W. Lu and K. Komvopoulos, “Nanotribological and nanomechanical properties of ultrathin amorphous carbon films synthesized by radio frequency sputtering”, *J. Tribol. (ASME)* **123**:3 (2001), 641–650.
- [Luan and Robbins 2005] B. Luan and M. O. Robbins, “The breakdown of continuum models for mechanical contacts”, *Nature* **435**:7044 (2005), 929–932.
- [Marshall and Evans 1984] D. B. Marshall and A. G. Evans, “Measurement of adherence of residually stressed thin films by indentation. I: Mechanics of interface delamination”, *J. Appl. Phys.* **56**:10 (1984), 2632–2638.
- [Parks et al. 2008] M. L. Parks, R. B. Lehoucq, S. J. Plimpton, and S. A. Silling, “Implementing peridynamics within a molecular dynamics code”, *Comput. Phys. Commun.* **179**:11 (2008), 777–783.
- [Parks et al. 2010] M. L. Parks, P. Seleson, S. J. Plimpton, S. A. Silling, and R. B. Lehoucq, “Peridynamics with LAMMPS: A user guide v0.3 beta”, Report 2011-8523, Sandia National Labs, 2010, <http://prod.sandia.gov/techlib/access-control.cgi/2011/118523.pdf>.
- [Silling 2000] S. A. Silling, “Reformulation of elasticity theory for discontinuities and long-range forces”, *J. Mech. Phys. Solids* **48**:1 (2000), 175–209.
- [Silling and Askari 2005] S. A. Silling and E. Askari, “A meshfree method based on the peridynamic model of solid mechanics”, *Comput. Struct.* **83**:17 (2005), 1526–1535.
- [Silling and Bobaru 2005] S. A. Silling and F. Bobaru, “Peridynamic modeling of membranes and fibers”, *Int. J. Non-Linear Mech.* **40**:2-3 (2005), 395–409.
- [Silling and Lehoucq 2008] S. A. Silling and R. B. Lehoucq, “Convergence of peridynamics to classical elasticity theory”, *J. Elasticity* **93**:1 (2008), 13–37.
- [Silling et al. 2007] S. A. Silling, M. Epton, O. Weckner, J. Xu, and E. Askari, “Peridynamic states and constitutive modeling”, *J. Elasticity* **88**:2 (2007), 151–184.
- [Volinsky et al. 2002] A. A. Volinsky, N. R. Moody, and W. W. Gerberich, “Interfacial toughness measurements for thin films on substrates”, *Acta Mater.* **50**:3 (2002), 441–466.
- [Xu et al. 2008] J. Xu, A. Askari, O. Weckner, and S. Silling, “Peridynamic analysis of impact damage in composite laminates”, *J. Aerosp. Eng. (ASCE)* **21**:3 (2008), 187–194.

Received 3 Oct 2014. Revised 2 Jun 2015. Accepted 19 Jun 2015.

SAYNA EBRAHIMI: [sayna@berkeley.edu](mailto:sayna@berkeley.edu)

*Department of Mechanical Engineering, University of California, Berkeley, CA 94720-1740, United States*

DAVID J. STEIGMANN: [dsteigmann@berkeley.edu](mailto:dsteigmann@berkeley.edu)

*Department of Mechanical Engineering, University of California, Berkeley, 6133 Etcheverry Hall, Berkeley, CA 94720-1740, United States*

KYRIAKOS KOMVOPOULOS: [kyriakos@me.berkeley.edu](mailto:kyriakos@me.berkeley.edu)

*Department of Mechanical Engineering, University of California, Berkeley, 5143 Etcheverry Hall, Berkeley, CA 94720-1740, United States*

## INVERSE PROBLEMS IN HETEROGENEOUS AND FRACTURED MEDIA USING PERIDYNAMICS

DANIEL Z. TURNER, BART G. VAN BLOEMEN WAANDERS AND MICHAEL L. PARKS

The following work presents an adjoint-based methodology for solving inverse problems in heterogeneous and fractured media using state-based peridynamics. We show that the inner product involving the peridynamic operators is self-adjoint. The proposed method is illustrated for several numerical examples with constant and spatially varying material parameters as well as in the context of fractures. We also present a framework for obtaining material parameters by integrating digital image correlation (DIC) with inverse analysis. This framework is demonstrated by evaluating the bulk and shear moduli for a sample of nuclear graphite using digital photographs taken during the experiment. The resulting measured values correspond well with other results reported in the literature. Lastly, we show that this framework can be used to determine the load state given observed measurements of a crack opening. This type of analysis has many applications in characterizing subsurface stress-state conditions given fracture patterns in cores of geologic material.

### 1. Introduction

Detecting fractures is important in many areas of engineering and geoscience. From material reliability to characterization of petroleum source rock, the goal is to predict the magnitude and orientation of fractures by calibrating the properties of numerical models so that eventually accurate predictions can be issued. Model calibration is a mathematical inversion process in which the differences between observations and numerical predictions are reconciled by perturbing model parameters such as boundary conditions, loadings, and material properties. Given a sufficient number of observations, accurate numerical models can be calculated, which in turn can then support the improvement of system design and operating conditions. In this paper, we are interested in solving inverse problems that determine loading conditions and material properties for fractured linear elasticity problems. Given calibrated numerical models, the design of engineering systems to ensure material reliability can be improved or more accurate flow patterns can increase the extraction of hydrocarbon in petroleum reservoirs. Various challenges arise in this type of an inversion problem, consisting of (1) achieving accurate and efficient modeling of fractures, (2) handling of large numbers of inversion parameters, (3) addressing sparsity of observations inherent in most large-scale inversion problems, (4) managing discontinuities from fractures, and (5) accounting for nonlinearities in the material inversion problem.

Our first challenge is to numerically model fractures accurately and efficiently in addition to being more conducive to the inverse setting. In particular, sensitivity objects will need to be extracted from the forward model to efficiently calculate the gradient as part of an optimization algorithm. Consequently, any approach must be able to generate derivatives with respect to the state variable (displacements in

---

*Keywords:* peridynamics, fractured media, inverse problems, digital image correlation.

the case of linear elasticity). To accommodate this prerequisite and model fractures, we leverage peridynamics, which has rapidly gained popularity as a nonlocal model for solid mechanics and naturally incorporates discontinuities (cracks). As opposed to partial derivative based models, integral equations are used instead, thereby avoiding differentiability requirements on the displacement field in the forward case. One of the goals of the paper is to demonstrate that this differentiability condition is not violated in the inverse setting. First introduced in 2000, peridynamics has been successfully applied in a number of areas [Silling 2000; Silling et al. 2007; Silling and Askari 2005; Silling and Lehoucq 2008]. The methodology has evolved from a bond- to a state-based approach to allow the modeling of more general linear elastic materials with Poisson's ratio other than  $\frac{1}{4}$ . Furthermore, this paper graduates peridynamics from a powerful forward modeling capability to, in some respects, an even more powerful inversion capability. Our inversion approach extends to other optimization formulations such as design and control problems.

The second and third challenges motivate the use of large-scale inversion techniques to solve a least square problem constrained by peridynamics. Also known as a constrained optimization problem or in the case of partial differential equation (PDE) based dynamics, PDE-constrained optimization [Akçelik et al. 2006], these techniques are designed to take advantage of embedded sensitivity calculations from the forward simulation to efficiently calculate the objective function gradient. For moderate numbers of inversion parameters, direct sensitivities can be used, but for large numbers of inversion variables, such as material properties, the size of which is equal to the number of degrees of freedom of the problem, an adjoint-based sensitivity calculation is required. In this paper, we explore the adjoint of peridynamics by leveraging nonlocal vector calculus (NLVC) [Du et al. 2013b] and demonstrate that the inner product of the forward operators with a vector is self-adjoint. Furthermore, we establish an inverse formulation based on the displacement of the material points without having to accommodate the so-called damage model that determines which broken bonds are part of a fracture. This addresses the fourth challenge, which identified a need to manage discontinuities from fractures.

The final challenge is addressed through the application of Newton-based optimization algorithms with line-search globalization and Tikhonov regularization to solve our target inverse problems. The constrained optimization problem is converted to an unconstrained formulation by forming a Lagrangian. Taking variations with respect to the state, Lagrange multipliers, and inversion parameters, the optimality conditions are derived. In the case of inverting for loading conditions, the optimality conditions are linear and therefore equal to the final Karush–Kuhn–Tucker (KKT) matrix. For material inversion, the optimality conditions are nonlinear and a linearization step via a Newton method is needed to arrive at the KKT system. In our numerical example, the observational data provides information at each computational node and therefore regularization does not dramatically improve the quality of the inversion. It should be noted that our solution techniques are applied to an unconstrained optimization problem by exercising a nonlinear elimination of the constraints. In subsequent sections of the paper, our derivation of the optimality conditions for a constrained optimization problem is primarily for presentational reasons; an alternative approach could be to differentiate the unconstrained objective function and apply the chain rule. With additional algebraic manipulations, the adjoint equation could be derived [van Bloemen Waanders et al. 2005].

The observational data in our numerical examples comes from digital image correlation (DIC), which is a noncontact, full-field displacement measurement technique. DIC uses digital images of the experimental sample to determine deformations [Sutton et al. 2009; Chu et al. 1985; Pan et al. 2009; Hild

and Roux 2006]. The process works by correlating subsets of pixels from an image of the undeformed experimental sample to a subset of an image of the deformed sample. This technique provides a much richer set of displacement data than would otherwise be possible using mechanical gauges. We use DIC to provide the observations of the material behavior, which are subsequently used in the objective function of the optimization. Using optimization, we determine the material parameter values that lead to the best fit between the simulated displacement field and the displacement field obtained.

The backdrop of this work is in the field of materials characterization, and we build upon a number of previous works. Of particular interest are those that investigate heterogeneous or structurally damaged media. Hild and Roux [2006] review various methods for material property identification using several different flavors of DIC. Grédiac [2004] evaluates the efficacy of DIC-based methods for composite materials. An anisotropic damage law is calibrated using DIC by Périé et al. [2009], who show that the proposed method obtains close correlation even under significant noise.

It will be important to distinguish the emphasis of this work on materials characterization for fractured media rather than determining fracture parameters using inversion. Asmaro [2013] uses a similar integration of DIC and inversion to obtain fracture parameters for concrete materials. Her inversion process is based on a finite element model that uses hinge elements. Many of the difficulties encountered in this approach are circumvented in this work through the use of peridynamics, which more naturally incorporates cracks.

This work makes the following contributions:

- Solutions of the inverse problem are presented for state-based peridynamics using an adjoint-based method.
- Inversions demonstrate the state of material loading given fracture parameters such as crack aperture.
- A novel framework is presented for determining material parameters by integrating DIC with peridynamics inverse analysis.
- The applicability of this framework is shown for heterogeneous materials where the material parameters vary throughout the problem domain.

In the sections that follow, we briefly summarize state-based peridynamics, define the constrained optimization problem and optimality conditions that represent the peridynamics inverse problem, and verify the proposed methodology for a material inversion and a loading inversion in the context of a fractured medium. We demonstrate the framework for incorporating digital image correlation by analyzing a compact tension specimen of nuclear graphite.

## 2. State-based peridynamics

Peridynamics was introduced as a framework to address the shortcomings of PDE-based approaches in which material discontinuities are not conveniently handled. The integral representation of the force calculation between material points avoids the problem of differentiating through a discontinuity. Although recent extensions to finite element methods have been introduced to address these issues, it is not clear if these methods can address the inverse problem and achieve either differentiability or computational efficiency for the inverse problem. In the next two sections, we outline the basic peridynamics formulation and map this approach to the inverse setting.

The peridynamic state-based balance of linear momentum is written as

$$\rho \ddot{\mathbf{u}} = \int_{\mathcal{H}_x} \{ \underline{\mathbf{T}}[\mathbf{x}]\langle \mathbf{x}' - \mathbf{x} \rangle - \underline{\mathbf{T}}[\mathbf{x}']\langle \mathbf{x} - \mathbf{x}' \rangle \} dV_{x'} + \mathbf{b}(\mathbf{x}), \quad (1)$$

where  $\underline{\mathbf{T}}$  is the force state and  $\mathbf{b}(\mathbf{x})$  is a volumetric force. Here we use the underline notation to denote a state, which can be conceptualized as a scalar, vector, or tensor quantity of interest that involves a convolution with values of this field in the neighborhood of the material point in question. One can think of a state as being a quantity that derives its value from a sum of contributions over the region surrounding point  $\mathbf{x}$ . Within a spherical neighborhood,  $\mathcal{H}_x$ , of a material point at  $\mathbf{x}$ , the force interactions between  $\mathbf{x}$  and all other material points inside the neighborhood are nonzero. We use the state-based formulation for peridynamics to avoid the well-known restrictions on the material parameters that result from the bond-based formulation. The convention  $\langle \mathbf{x}' - \mathbf{x} \rangle$  denotes a bond between points  $\mathbf{x}$  and  $\mathbf{x}'$ . The original scalar length of a bond is denoted,  $\underline{x}$ . The current length of a bond is denoted,  $\underline{y}$ , and is a function of the displacement field,  $\mathbf{u}(\mathbf{x})$ . Without loss of generality, we ignore the inertial term and focus our attention on quasistatic analysis as this will clarify the presentation. Neglecting the inertial term has no impact on the development of the inversion process and can easily be reintroduced to obtain transient quantities. The quasistatic governing equations can be written in terms of the linear peridynamic operator,  $\mathcal{L}\mathbf{u}$

$$\mathcal{L}\mathbf{u}(\mathbf{x}) + \mathbf{b}(\mathbf{x}) = 0 \quad \text{in } \Omega \subset \mathbb{R}^d \quad (2)$$

where

$$\mathcal{L}\mathbf{u}(\mathbf{x}) := \int_{\mathcal{H}_x} \{ \underline{\mathbf{T}}[\mathbf{x}]\langle \mathbf{x}' - \mathbf{x} \rangle - \underline{\mathbf{T}}[\mathbf{x}']\langle \mathbf{x} - \mathbf{x}' \rangle \} dV_{x'}, \quad (3)$$

$d$  is the spatial dimension and  $\Omega$  is the domain. Readers unfamiliar with the notation of state-based peridynamics should consult [Silling et al. 2007] in which the state-based formulation is presented. In general, a peridynamic state produces a quantity from a summation of values over a material point's family. In the case of the force state, the resulting vector is the force density at a point given the interactions with all the bonds in the family. For an ordinary material, the force between material points acts along a unit vector between the two points in the deformed configuration (as shown at the top of Figure 1) such that the force state can be expressed as

$$\underline{\mathbf{T}} = \underline{t} \underline{\mathbf{M}}, \quad (4)$$

where  $\underline{\mathbf{M}}$  is the unit vector pointing from  $\mathbf{x} + \mathbf{u}(\mathbf{x})$  to  $\mathbf{x}' + \mathbf{u}(\mathbf{x}')$  and  $\underline{t}$  is the scalar force state.

For a linear, elastic material (parametrized by  $k$  and  $\mu$ ), in plane-strain, the constitutive relationship between the scalar force state and the deformation is

$$\underline{t} = \tilde{k} \left( \frac{2\theta}{m} \underline{x} \right) + \tilde{\alpha} \left( \underline{y} - \underline{x} \left( 1 + \frac{\theta}{2} \right) \right), \quad (5)$$

where  $m$  is the weighted size

$$m = \int_{\mathcal{H}_x} \underline{x}^2 dV_{x'}, \quad (6)$$

$\theta$  is the dilatation

$$\theta = \frac{2}{m} \int_{\mathcal{H}_x} (\underline{y} - \underline{x}) \underline{x} dV_{x'}, \quad (7)$$

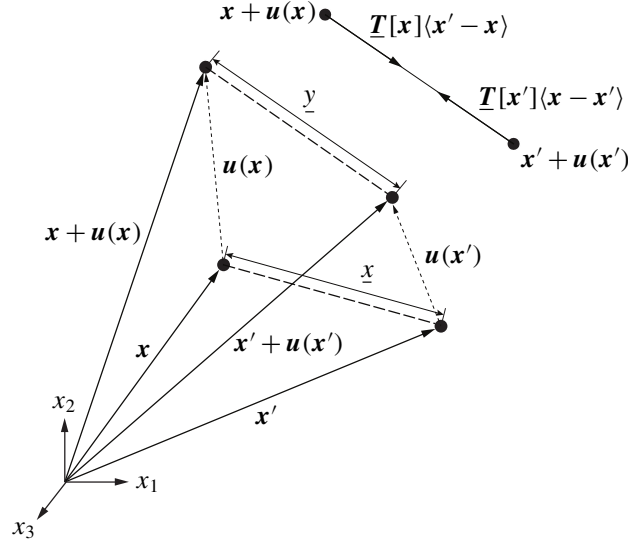


**Figure 1.** Geometry of deformation for peridynamics. This figure shows a bond between two material points as it evolves from the reference to the deformed configuration. The nodes in the figure above represent the cell centroids in the discretization of peridynamics. The cells surrounding each node are not drawn in this figure. The force-state interaction of these two material points is shown in the top of the figure which illustrates that the resulting forces align with the bond between the material points. Here we are using an ordinary material formulation in which the force between material points is always directed along the bond between them.

and the coefficients are  $\tilde{k} = (k + \mu/9)$  and  $\tilde{\alpha} = 8\mu/m$ . (Here we are using the two-dimensional formulation proposed in [Le et al. 2014]. Extending this formulation to three dimensions is trivial.)

In the discrete setting, using single point quadrature, (1) becomes<sup>1</sup>

$$c(\mathbf{u}, k, \mu) \equiv \sum_{i=1}^{N_x} \{ \underline{\mathbf{T}}[\mathbf{x}]\langle \mathbf{x}'_i - \mathbf{x} \rangle - \underline{\mathbf{T}}[\mathbf{x}'_i]\langle \mathbf{x} - \mathbf{x}'_i \rangle \} V_{x_i} + \mathbf{b}(\mathbf{x}) = 0 \tag{8}$$

for all points in the domain, where  $N_x$  is the number of discrete neighbors of  $\mathbf{x}$  in  $\mathcal{H}_x$  and  $V_{x_i}$  is the cell area of neighbor  $i$ . The structure of (8) is important from the perspective that it preserves symmetry of the resulting tangent matrix. This ensures that the discrete operator,  $\mathbf{J}_u$  (to be defined below) has the following property,  $\mathbf{J}_u = \mathbf{J}_u^T$ , even if the material parameters vary throughout the domain, for example  $k(\mathbf{x}) \neq k(\mathbf{x}')$ . Also note that the quantities  $\theta$  and  $\underline{y}$  are dependent on the peridynamic displacement field,  $\mathbf{u}$ .

<sup>1</sup>Note that in the formulation above we have used a constant, unit, influence function ( $\underline{w} = 1$ ), which we have omitted for brevity.

The weighted size and dilatation are computed in the discrete setting as

$$m = \sum_{i=1}^N \underline{x}^2 V_{x'_i}, \quad (9)$$

$$\theta = \frac{2}{m} \sum_{i=1}^N (\underline{y} - \underline{x}) \underline{x} V_{x'_i}. \quad (10)$$

### 3. Peridynamics inverse problem

In this section, our optimization problem is formulated, the optimality conditions are derived, and we prove that the inner product involving the forward operators is self-adjoint. This realization has obvious benefits to implementing the inverse process.

**3.1. Inverse problem.** The inverse problem can be stated as the following nonlinear, constrained, least squares optimization problem:

$$\min_{\mathbf{u}, k, \mu} g(\mathbf{u}, k, \mu) \quad \text{subject to} \quad \begin{cases} \mathbf{c}(\mathbf{u}, k, \mu) = \mathbf{0} & \text{in } \Omega, \\ \mathbf{u} = \mathbf{u}_0 & \text{in } \Omega^u, \\ \mathbf{b} = \mathbf{q} & \text{in } \Omega^q \end{cases} \quad (11)$$

where  $\mathbf{c}(\mathbf{u}, k, \mu)$  is the constraint equation given by (8).  $\Omega^u$  and  $\Omega^q$  are the volume constraint regions for displacement and loading, respectively. Note that as opposed to traditional boundary value problems in which the boundary conditions are prescribed over a surface, in peridynamics, the boundary conditions are prescribed over a volume. Typically, to represent a displacement boundary condition, rather than apply a prescribed displacement on the surface nodes, ghost cells are added to the domain at the boundary, for which the displacement is given. For loading boundary conditions, the prescribed load is distributed among a collection of cells interior to the domain. The above problem is nonlinear due to the constraint equation's dependence on the decision variables.<sup>2</sup> We employ a least squares misfit of the computed displacements with a set of observed displacements,  $\mathbf{u}^*$ , at  $N_{\text{obs}}$  observation points, as our objective function,  $g(\mathbf{u}, k, \mu)$ , with Tikhonov regularization [Tikhonov and Arsenin 1977]:

$$g(\mathbf{u}, k, \mu) = \frac{1}{2} \sum_{j=1}^{N_{\text{obs}}} \int_{\Omega} ((u_x - u_x^*)^2 + (u_y - u_y^*)^2) \delta(\mathbf{x} - \mathbf{x}_j) d\Omega + \frac{\psi_k}{2} \int_{\Omega} k^2 d\Omega + \frac{\psi_\mu}{2} \int_{\Omega} \mu^2 d\Omega. \quad (12)$$

In the objective function above,  $\Omega$  represents the problem domain,  $\psi_k$  and  $\psi_\mu$  are the regularization parameters and  $\delta$  is the Dirac delta. We wish to invert the system of state-based peridynamics equations above for the material parameters  $k$  and  $\mu$ , which represent our *decision* variables. The parameters  $\psi_\mu$  and  $\psi_k$  represent tunable parameters that drive the optimization process to a unique solution. The third and fourth terms in the functional provide that for large values of  $\psi_\mu$  and  $\psi_k$  the functional is quadratic in nature.

<sup>2</sup>Formally speaking, since we solve the above system in a staggered fashion, it would be more appropriate to denote the minimization problem as  $\text{ming}(\mathbf{u}(k, \mu))$  where  $\mathbf{u}$  satisfies  $\mathbf{c}(\mathbf{u}(k, \mu)) = 0$ .



**3.2. Optimality conditions.** Introducing the Lagrange multiplier field,  $\lambda(\mathbf{x})$  (the adjoint variable) the following Lagrangian functional can be constructed using the inner product

$$L(\mathbf{u}, \lambda, \mathbf{d}) := g(\mathbf{u}, \mathbf{d}) + \int_{\Omega} \mathbf{c} \cdot \lambda - \mathbf{d} \cdot \lambda \, dx, \tag{13}$$

where  $\mathbf{d}$  represents the decision variables that include  $k$  and  $\mu$ . Linearizing the peridynamic operator and taking variations of  $L(\mathbf{u}, \lambda, \mathbf{d})$  with respect to  $\mathbf{u}$ ,  $\mathbf{d}$  and  $\lambda$  produces optimality conditions given below. It can be shown that taking the variation with respect to  $\mathbf{u}$  leads to  $\mathcal{L}^* = \mathbf{J}_u = \partial \mathbf{c} / \partial \mathbf{u}$ , i.e. that the peridynamic operator is self-adjoint, the proof of which is demonstrated in the following section.

The optimality conditions for (11) are as follows:

$$\mathbf{c} = \mathbf{0} \quad \text{in } \Omega \quad (\text{state}), \tag{14}$$

$$\mathbf{J}_u^T \lambda + \mathbf{g}_u = \mathbf{0} \quad \text{in } \Omega \quad (\text{adjoint}), \tag{15}$$

$$\mathbf{J}_d^T \lambda + \mathbf{g}_d = \mathbf{0} \quad \text{in } \Omega \quad (\text{decision}). \tag{16}$$

In the discrete context,  $\mathbf{u} \in \mathbb{R}^M$  is the state variable vector,  $\lambda \in \mathbb{R}^M$  is the adjoint variable vector, and  $\mathbf{d} \in \mathbb{R}^P$  is the decision variable vector. For the numerical examples that follow, the decision vector is assembled as a single column vector

$$\mathbf{d} = \begin{bmatrix} k_1 \\ \vdots \\ k_{P/2} \\ \mu_1 \\ \vdots \\ \mu_{P/2} \end{bmatrix}. \tag{17}$$

The other terms in the optimality conditions include:  $\mathbf{J}_u = \partial \mathbf{c} / \partial \mathbf{u} \in \mathbb{R}^{M \times M}$  which is a matrix that represents the variation of the constraint with respect to the state variables;  $\mathbf{J}_d = \partial \mathbf{c} / \partial \mathbf{d} \in \mathbb{R}^{M \times P}$ , a matrix that represents the variation of the constraint with respect to the decision variables;  $\mathbf{g}_u = \partial g / \partial \mathbf{u} \in \mathbb{R}^M$ , and  $\mathbf{g}_d = \partial g / \partial \mathbf{d} \in \mathbb{R}^P$ , that represent the sensitivity of the objective function to the state and decision variables, respectively.

In addition to the optimization problem being nonlinear, the state equation is also nonlinear due to the dependence of the displacement at  $\mathbf{x}$  on the displacement at  $\mathbf{x}'$  (hence the nonlocal nature of peridynamics). To treat this complexity, in the calculation of  $\mathbf{J}_u$ , we first linearize the state equation and compute  $\mathbf{J}_u$  using central finite differencing. The above optimization problem can be solved using a variety of methods. For the numerical examples that follow, a reflective trust-region algorithm was used with a conjugate gradient solver. For any given method, the gradient of the objective function with respect to the decision variables,  $\nabla_d(g) = dg/d\mathbf{d}$ , must be computed. To compute  $\nabla_d(g)$ , the following algorithm was used. First, the adjoint equation is solved for  $\lambda$ , as

$$\lambda = -\mathbf{J}_u^{-T} \mathbf{g}_u. \tag{18}$$

Once the adjoint variables are determined, the gradient of the objective function can be computed as

$$\nabla_d(g) = -\mathbf{g}_d - \mathbf{J}_d^T \boldsymbol{\lambda}. \quad (19)$$

**3.3. Self-adjointness of the peridynamic operator.** The self-adjointness of  $\mathcal{L}$  is not immediately obvious given the state-based representation of peridynamics. The state-based formulation involves a multilayered convolution, the first is used to obtain the dilatation which is then convolved for the force state. To prove this property we turn to NLVC [Du et al. 2013a; Gunzburger and Lehoucq 2010; Du et al. 2013b; Alali et al. 2014] in an effort to analyze the peridynamic operator in a more straightforward manner. The self-adjointness of peridynamics on bounded domains has also been studied in [Mengesha and Du 2014; 2015]. NLVC is a recently introduced formalism with appropriate nonlocal corollaries to all of the components of local balance laws. In addition, NLVC can be used to cast nonlocal theories (like peridynamics) in a more abstract and general mathematical setting which is more amenable to analysis. Following the presentation in [Alali et al. 2014], the peridynamics operator,  $\mathcal{L}$  from (2) can be written as

$$\mathcal{L}\mathbf{u} = -\mathcal{G}(c_1 \mathcal{G}^* \mathbf{u}) - \mathcal{G}(c_2 \overline{\mathcal{G}^*} \mathbf{u}), \quad (20)$$

where  $\mathcal{G}$ ,  $\mathcal{G}^*$  and  $\overline{\mathcal{G}^*}$  are defined as the nonlocal gradient operator, the adjoint of the nonlocal gradient operator and the average of the adjoint, respectively. For a scalar function  $\xi(\mathbf{x}, \mathbf{y})$  these are given as

$$(\mathcal{G}\xi)(\mathbf{x}) = \int_{\mathbb{R}^d} (\xi(\mathbf{y}, \mathbf{x}) + \xi(\mathbf{x}, \mathbf{y})) \boldsymbol{\alpha}(\mathbf{x}, \mathbf{y}) d\mathbf{y}, \quad (21)$$

$$(\mathcal{G}^* \mathbf{u}) = -(\mathbf{u}(\mathbf{y}) - \mathbf{u}(\mathbf{x})) \cdot \boldsymbol{\alpha}(\mathbf{x}, \mathbf{y}), \quad (22)$$

$$(\overline{\mathcal{G}^*} \mathbf{u})(\mathbf{x}) = - \int_{\mathbb{R}^d} (\mathbf{u}(\mathbf{y}) - \mathbf{u}(\mathbf{x})) \cdot \boldsymbol{\alpha}(\mathbf{x}, \mathbf{y}) d\mathbf{y}, \quad (23)$$

where  $\boldsymbol{\alpha}(\mathbf{x}, \mathbf{y})$  is an appropriate antisymmetric vector-valued kernel ( $\boldsymbol{\alpha}(\mathbf{x}, \mathbf{y}) = -\boldsymbol{\alpha}(\mathbf{y}, \mathbf{x})$ ). We have cast the peridynamic equations in the NLVC setting to derive the adjoint of  $\mathcal{L}$ , denoted as  $\mathcal{L}^*$ . Given the function spaces and duality pairings defined in [Alali et al. 2014], the adjoint of the peridynamic operator is defined such that it satisfies

$$\langle \mathbf{v}, \mathcal{L}\mathbf{u} \rangle = \langle \mathbf{u}, \mathcal{L}^* \mathbf{v} \rangle, \quad (24)$$

where  $\langle \cdot, \cdot \rangle$  is the vector inner product, given by  $\langle \mathbf{a}(\mathbf{x}), \mathbf{b}(\mathbf{x}) \rangle = \int_{\mathbb{R}^d} \mathbf{a}(\mathbf{x}) \cdot \mathbf{b}(\mathbf{x}) d\mathbf{x}$ . Expanding the terms of (20), gives

$$\mathcal{G}(c_1 \mathcal{G}^* \mathbf{u}) = - \int_{\mathbb{R}^d} [c_1(\mathbf{y})(\mathbf{u}(\mathbf{x}) - \mathbf{u}(\mathbf{y})) \cdot \boldsymbol{\alpha}(\mathbf{y}, \mathbf{x}) + c_1(\mathbf{x})(\mathbf{u}(\mathbf{y}) - \mathbf{u}(\mathbf{x})) \cdot \boldsymbol{\alpha}(\mathbf{x}, \mathbf{y})] \boldsymbol{\alpha}(\mathbf{x}, \mathbf{y}) d\mathbf{y},$$

$$\mathcal{G}(c_2 \overline{\mathcal{G}^*} \mathbf{u}) = - \int_{\mathbb{R}^d} \left[ c_2(\mathbf{y}) \int_{\mathbb{R}^d} (\mathbf{u}(\mathbf{z}) - \mathbf{u}(\mathbf{y})) \cdot \boldsymbol{\alpha}(\mathbf{y}, \mathbf{z}) dz + c_2(\mathbf{x}) \int_{\mathbb{R}^d} (\mathbf{u}(\mathbf{z}) - \mathbf{u}(\mathbf{x})) \cdot \boldsymbol{\alpha}(\mathbf{x}, \mathbf{z}) dz \right] \boldsymbol{\alpha}(\mathbf{x}, \mathbf{y}) d\mathbf{y}.$$

The inner product of  $\mathcal{L}\mathbf{u}$  and  $\mathbf{v}$  is then

$$\begin{aligned} \langle \mathbf{v}, \mathcal{L}\mathbf{u} \rangle &= \int_{\mathbb{R}^d} \int_{\mathbb{R}^d} [c_1(\mathbf{y})(\mathbf{u}(\mathbf{x}) - \mathbf{u}(\mathbf{y})) \cdot \boldsymbol{\alpha}(\mathbf{y}, \mathbf{x}) + c_1(\mathbf{x})(\mathbf{u}(\mathbf{y}) - \mathbf{u}(\mathbf{x})) \cdot \boldsymbol{\alpha}(\mathbf{x}, \mathbf{y})] \boldsymbol{\alpha}(\mathbf{x}, \mathbf{y}) \cdot \mathbf{v}(\mathbf{x}) d\mathbf{x} d\mathbf{y} \\ &+ \int_{\mathbb{R}^d} \int_{\mathbb{R}^d} \left[ c_2(\mathbf{y}) \int_{\mathbb{R}^d} (\mathbf{u}(\mathbf{z}) - \mathbf{u}(\mathbf{y})) \cdot \boldsymbol{\alpha}(\mathbf{y}, \mathbf{z}) dz + c_2(\mathbf{x}) \int_{\mathbb{R}^d} (\mathbf{u}(\mathbf{z}) - \mathbf{u}(\mathbf{x})) \cdot \boldsymbol{\alpha}(\mathbf{x}, \mathbf{z}) dz \right] \boldsymbol{\alpha}(\mathbf{x}, \mathbf{y}) \cdot \mathbf{v}(\mathbf{x}) d\mathbf{x} d\mathbf{y}. \end{aligned}$$

Expanding all terms in the inner product gives

$$\begin{aligned}
 \langle \mathbf{v}, \mathcal{L}\mathbf{u} \rangle &= \int_{\mathbb{R}^d} \int_{\mathbb{R}^d} c_1(\mathbf{y})(\mathbf{u}(\mathbf{x}) \cdot \boldsymbol{\alpha}(\mathbf{y}, \mathbf{x}))(\boldsymbol{\alpha}(\mathbf{x}, \mathbf{y}) \cdot \mathbf{v}(\mathbf{x})) \, d\mathbf{x} \, d\mathbf{y} \\
 &\quad - \int_{\mathbb{R}^d} \int_{\mathbb{R}^d} c_1(\mathbf{y})(\mathbf{u}(\mathbf{y}) \cdot \boldsymbol{\alpha}(\mathbf{y}, \mathbf{x}))(\boldsymbol{\alpha}(\mathbf{x}, \mathbf{y}) \cdot \mathbf{v}(\mathbf{x})) \, d\mathbf{x} \, d\mathbf{y} \\
 &\quad + \int_{\mathbb{R}^d} \int_{\mathbb{R}^d} c_1(\mathbf{x})(\mathbf{u}(\mathbf{y}) \cdot \boldsymbol{\alpha}(\mathbf{x}, \mathbf{y}))(\boldsymbol{\alpha}(\mathbf{x}, \mathbf{y}) \cdot \mathbf{v}(\mathbf{x})) \, d\mathbf{x} \, d\mathbf{y} \\
 &\quad - \int_{\mathbb{R}^d} \int_{\mathbb{R}^d} c_1(\mathbf{x})(\mathbf{u}(\mathbf{x}) \cdot \boldsymbol{\alpha}(\mathbf{x}, \mathbf{y}))(\boldsymbol{\alpha}(\mathbf{x}, \mathbf{y}) \cdot \mathbf{v}(\mathbf{x})) \, d\mathbf{x} \, d\mathbf{y} \\
 &\quad + \int_{\mathbb{R}^d} \int_{\mathbb{R}^d} c_2(\mathbf{y}) \int_{\mathbb{R}^d} (\mathbf{u}(\mathbf{z}) \cdot \boldsymbol{\alpha}(\mathbf{y}, \mathbf{z})) \, d\mathbf{z} (\boldsymbol{\alpha}(\mathbf{x}, \mathbf{y}) \cdot \mathbf{v}(\mathbf{x})) \, d\mathbf{x} \, d\mathbf{y} \\
 &\quad - \int_{\mathbb{R}^d} \int_{\mathbb{R}^d} c_2(\mathbf{y}) \int_{\mathbb{R}^d} (\mathbf{u}(\mathbf{y}) \cdot \boldsymbol{\alpha}(\mathbf{y}, \mathbf{z})) \, d\mathbf{z} (\boldsymbol{\alpha}(\mathbf{x}, \mathbf{y}) \cdot \mathbf{v}(\mathbf{x})) \, d\mathbf{x} \, d\mathbf{y} \\
 &\quad + \int_{\mathbb{R}^d} \int_{\mathbb{R}^d} c_2(\mathbf{x}) \int_{\mathbb{R}^d} (\mathbf{u}(\mathbf{z}) \cdot \boldsymbol{\alpha}(\mathbf{x}, \mathbf{z})) \, d\mathbf{z} (\boldsymbol{\alpha}(\mathbf{x}, \mathbf{y}) \cdot \mathbf{v}(\mathbf{x})) \, d\mathbf{x} \, d\mathbf{y} \\
 &\quad - \int_{\mathbb{R}^d} \int_{\mathbb{R}^d} c_2(\mathbf{x}) \int_{\mathbb{R}^d} (\mathbf{u}(\mathbf{x}) \cdot \boldsymbol{\alpha}(\mathbf{x}, \mathbf{z})) \, d\mathbf{z} (\boldsymbol{\alpha}(\mathbf{x}, \mathbf{y}) \cdot \mathbf{v}(\mathbf{x})) \, d\mathbf{x} \, d\mathbf{y}.
 \end{aligned}$$

Using the antisymmetry of  $\boldsymbol{\alpha}(\mathbf{x}, \mathbf{y})$  and a change of variable from  $\mathbf{x} \rightarrow \mathbf{y}$  in some of the terms above leads to

$$\begin{aligned}
 \langle \mathbf{v}, \mathcal{L}\mathbf{u} \rangle &= \int_{\mathbb{R}^d} \int_{\mathbb{R}^d} c_1(\mathbf{y})(\mathbf{u}(\mathbf{x}) \cdot \boldsymbol{\alpha}(\mathbf{y}, \mathbf{x}))(\boldsymbol{\alpha}(\mathbf{x}, \mathbf{y}) \cdot \mathbf{v}(\mathbf{x})) \, d\mathbf{x} \, d\mathbf{y} \\
 &\quad \times \int_{\mathbb{R}^d} \int_{\mathbb{R}^d} c_1(\mathbf{x})(\mathbf{u}(\mathbf{x}) \cdot \boldsymbol{\alpha}(\mathbf{x}, \mathbf{y}))(\boldsymbol{\alpha}(\mathbf{x}, \mathbf{y}) \cdot \mathbf{v}(\mathbf{y})) \, d\mathbf{x} \, d\mathbf{y} \\
 &\quad - \int_{\mathbb{R}^d} \int_{\mathbb{R}^d} c_1(\mathbf{y})(\mathbf{u}(\mathbf{x}) \cdot \boldsymbol{\alpha}(\mathbf{x}, \mathbf{y}))(\boldsymbol{\alpha}(\mathbf{y}, \mathbf{x}) \cdot \mathbf{v}(\mathbf{y})) \, d\mathbf{x} \, d\mathbf{y} \\
 &\quad - \int_{\mathbb{R}^d} \int_{\mathbb{R}^d} c_1(\mathbf{x})(\mathbf{u}(\mathbf{x}) \cdot \boldsymbol{\alpha}(\mathbf{x}, \mathbf{y}))(\boldsymbol{\alpha}(\mathbf{x}, \mathbf{y}) \cdot \mathbf{v}(\mathbf{x})) \, d\mathbf{x} \, d\mathbf{y} \\
 &\quad + \int_{\mathbb{R}^d} \int_{\mathbb{R}^d} \int_{\mathbb{R}^d} c_2(\mathbf{y})(\mathbf{u}(\mathbf{x}) \cdot \boldsymbol{\alpha}(\mathbf{x}, \mathbf{y}))(\boldsymbol{\alpha}(\mathbf{y}, \mathbf{z}) \cdot \mathbf{v}(\mathbf{z})) \, d\mathbf{z} \, d\mathbf{x} \, d\mathbf{y} \\
 &\quad - \int_{\mathbb{R}^d} \int_{\mathbb{R}^d} \int_{\mathbb{R}^d} c_2(\mathbf{y})(\mathbf{u}(\mathbf{x}) \cdot \boldsymbol{\alpha}(\mathbf{x}, \mathbf{y}))(\boldsymbol{\alpha}(\mathbf{y}, \mathbf{z}) \cdot \mathbf{v}(\mathbf{y})) \, d\mathbf{z} \, d\mathbf{x} \, d\mathbf{y} \\
 &\quad + \int_{\mathbb{R}^d} \int_{\mathbb{R}^d} \int_{\mathbb{R}^d} c_2(\mathbf{x})(\mathbf{u}(\mathbf{x}) \cdot \boldsymbol{\alpha}(\mathbf{x}, \mathbf{y}))(\boldsymbol{\alpha}(\mathbf{x}, \mathbf{z}) \cdot \mathbf{v}(\mathbf{z})) \, d\mathbf{z} \, d\mathbf{x} \, d\mathbf{y} \\
 &\quad - \int_{\mathbb{R}^d} \int_{\mathbb{R}^d} \int_{\mathbb{R}^d} c_2(\mathbf{x})(\mathbf{u}(\mathbf{x}) \cdot \boldsymbol{\alpha}(\mathbf{x}, \mathbf{y}))(\boldsymbol{\alpha}(\mathbf{x}, \mathbf{z}) \cdot \mathbf{v}(\mathbf{x})) \, d\mathbf{z} \, d\mathbf{x} \, d\mathbf{y} \\
 &= \langle \mathbf{u}, \mathcal{L}^*\mathbf{v} \rangle.
 \end{aligned}$$

Here we have shown that the peridynamic operator is self-adjoint, i.e.,

$$\mathcal{L}^* = \mathcal{L}^T = \mathcal{L}. \tag{25}$$

| Parameter | Exact  | Computed | Error (%) |
|-----------|--------|----------|-----------|
| $k$       | 666.67 | 666.67   | 0.0000644 |
| $\mu$     | 400.0  | 399.9984 | 0.000395  |

**Table 1.** Results for the constant material parameter verification problem.

#### 4. Numerical examples

We present here three illustrative examples that demonstrate the effectiveness of the proposed method. The first problem is a verification problem in which the parameters  $k$  and  $\mu$  are determined as constants for the entire domain (nonspatially varying) and compared with the exact result. In the second problem we invert for a spatially varying, heterogeneous material parameter  $\mu(x)$  and compare the result with the exact solution. In the last problem, digital image correlation is used to experimentally determine  $k$  and  $\mu$  for a sample of nuclear graphite in a compact tension test.

**4.1. Verification for constant material parameters.** Consider a 2D, square domain  $\Omega \in \mathbb{R}^{L \times L}$ , where  $L = 1000$ , subjected to zero displacement along the bottom edge ( $y = 0$ ) and an applied force in the  $x$  and  $y$  directions,  $F_x = 1000.0$  and  $F_y = 1000.0$ , respectively, along the top edge as shown in Figure 2.<sup>3</sup> For this problem, the observed displacement field,  $\mathbf{u}^*$ , was manufactured by solving the forward problem with  $k = 666.67$  and  $\mu = 400.0$ . Both material parameters were held constant over the domain (i.e.  $P = 2$ ). The goal of this inverse problem is to solve for the constants  $k$  and  $\mu$ , given the loading and least squares misfit of the computed displacement field,  $\mathbf{u}$ , to the observed displacement field,  $\mathbf{u}^*$ , using the objective function defined by (12). For this problem no regularization was used ( $\psi_k = 0$  and  $\psi_\mu = 0$ ).

The domain was discretized into cells of size  $h \times h$ , where  $h = 100.0$ .<sup>4</sup> The initial guess for  $k$  and  $\mu$  were seeded with values of 100.0 and 100.0, respectively. Table 1 shows the results for this example. The results suggest that constant parameters can be inverted for with great accuracy using the methodology above. The convergence of the objective function is plotted in Figure 3.

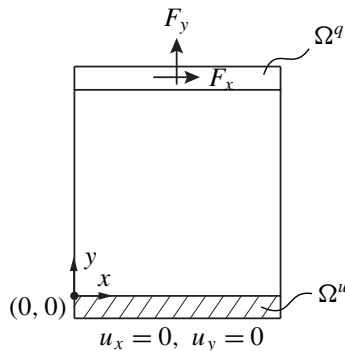


**Figure 2.** Domain and boundary conditions for academic verification problems.

<sup>3</sup>The force is applied by distributing the magnitude of the force over the cells along the top edge of the domain and adding the value to the momentum balance residual (8) for each point. As the horizon increases, the force is distributed over a layer of points near the boundary of thickness,  $\delta$ .

<sup>4</sup>Along the boundary, the centroid of the cell was placed on the edge of the domain such that  $h = 10.0$  results in 11 cells in  $x$  and  $y$ , or 121 cells total.

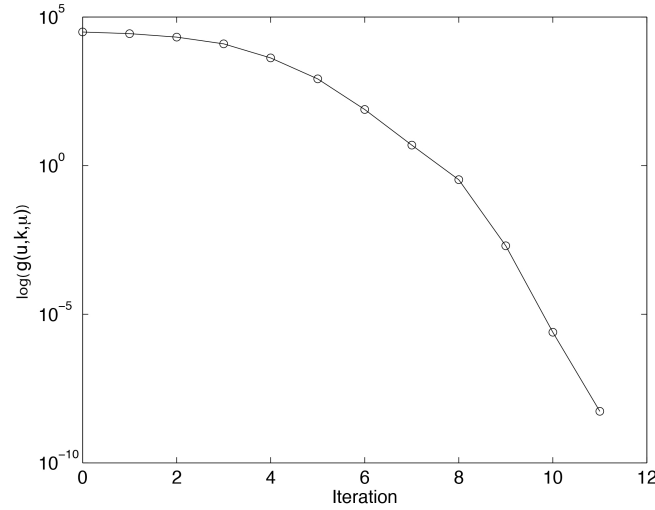


**Figure 3.** Convergence of the objective function per iteration for the constant material parameters problem. The y-axis is  $\log(g(u, k, \mu))$ .

**4.2. Inversion for heterogeneous material properties.** In this example we invert for  $\mu(\mathbf{x})$ , a spatially varying material parameter, using the same domain and boundary conditions shown in Figure 2. The value of  $\mu$  is determined for every cell in the domain (i.e.  $P = 121$ ). Observed values of displacement were populated using the following material parameters, which represent the exact solution.

$$k(\mathbf{x}) = -\gamma_k r k_0 + k_0, \tag{26}$$

$$\mu(\mathbf{x}) = \gamma_\mu r \mu_0 + \mu_0 \tag{27}$$

where  $r = \|\mathbf{x}\|$ ,  $\gamma_k = 0.00025$ ,  $\gamma_\mu = 0.0002$ ,  $k_0 = 666.67$  and  $\mu_0 = 400.0$ . The initial guess for  $\mathbf{d}$  was seeded with a constant  $\mu = \mu_0$  throughout the domain. Note that we only solve for  $\mu(\mathbf{x})$  and not  $k(\mathbf{x})$ .

A comparison between the computed result and the exact solution is shown in Figure 4. The maximum error in the computed solution is 1.2%. These results suggest that the method above is effective for constant material parameters as well as spatially varying fields. A plot of the convergence of the objective function for each iteration is shown in Figure 5.

**4.3. Inversion for material parameters using digital image correlation data.** The last example illustrates the proposed method’s usefulness in determining material parameters by inversion using experimental data generated with digital image correlation. For this example, the parameters  $k$  and  $\mu$  are determined for a sample of (nonirradiated) nuclear graphite loaded in a compact tension test. The boundary conditions for the problem are established by using the digital image correlation displacements as a prescribed displacement over a thin layer of cells that circumscribe the area of interest. To simplify the analysis, the parameters are evaluated for a load state early in the loading cycle before nonlinear behavior is present. A picture of the experimental setup is shown in Figure 6. The setup involves a single axis

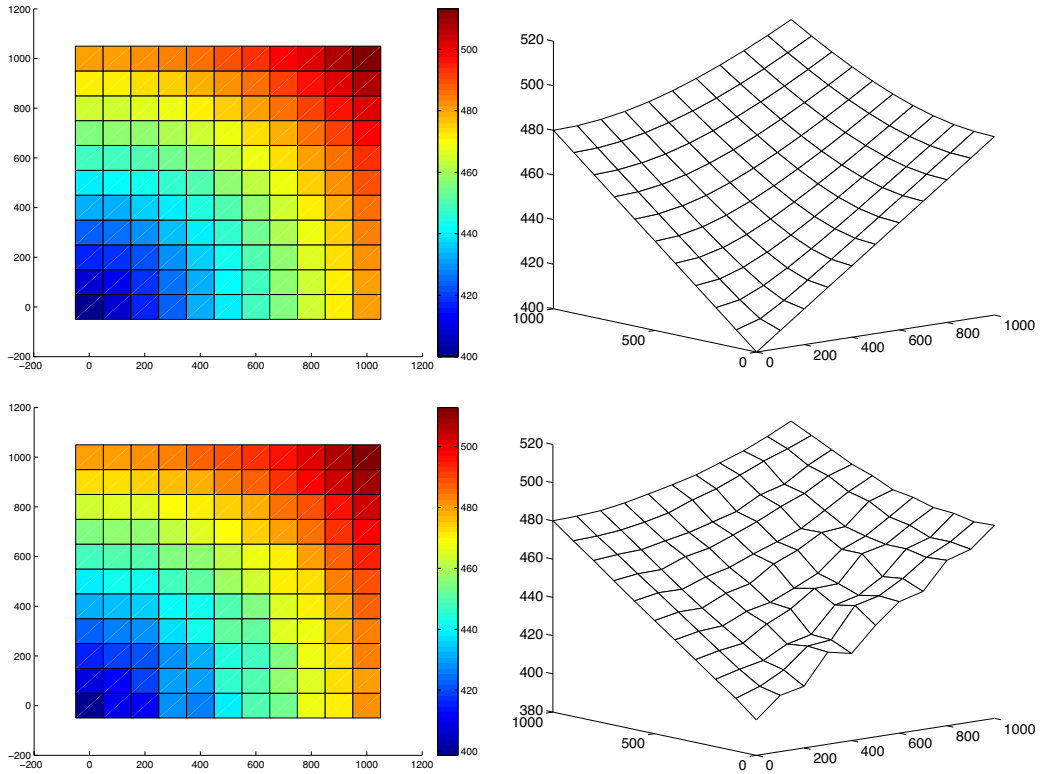


**Figure 4.** Top: exact  $\mu(x)$  shown as (left) a contour plot and (right) a surface plot. Bottom: computed  $\mu(x)$  shown as (left) a contour plot and (right) a surface plot.

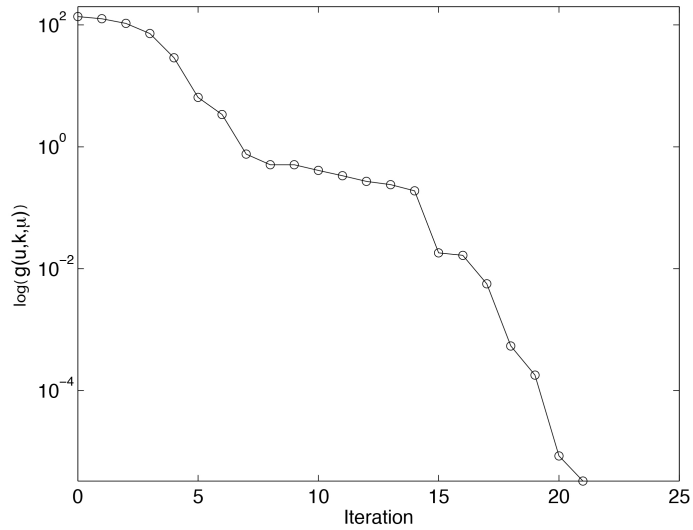


**Figure 5.** Convergence of the objective function per iteration for the heterogeneous problem. The y-axis is  $\log(g(u, k, \mu))$ .

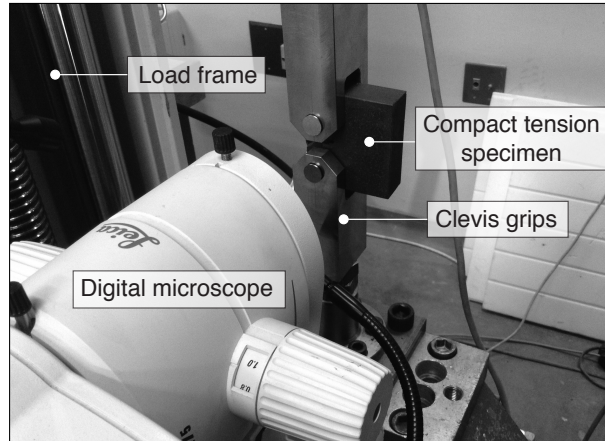


**Figure 6.** Experimental setup.

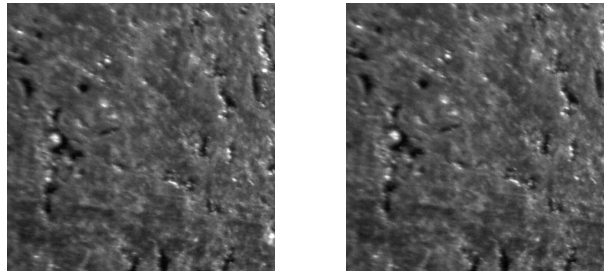


**Figure 7.** Left: reference image, taken prior to loading. Right: deformed image, taken early in the loading cycle. (Displacements are not visible the naked eye.)

load frame with the graphite sample loaded by clevis grips. Displacement control was used to load the sample until failure. A Leica digital microscope was used to obtain the images shown in Figure 7.<sup>5</sup>

*Digital image correlation algorithm.* The process of inverting for material parameters using digital image correlation is outlined below:

- (1) An image is taken with the microscope to serve as the reference image.
- (2) The load step is advanced.
- (3) Another image is taken to serve as the deformed image.
- (4) Control points are established for the reference and deformed images.
- (5) Displacements are calculated using a correlation algorithm (these will serve as the observed displacements,  $\mathbf{u}^*$ ).
- (6) A computational mesh is constructed such that each cell corresponds to a control point from the image correlation.

<sup>5</sup>It was not necessary to apply a speckle pattern to the sample since there is enough variation in surface due to the natural voids in the graphite.

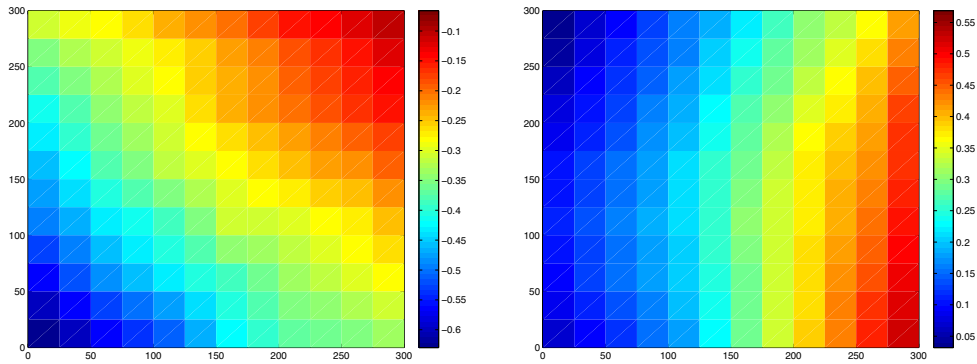


**Figure 8.** Left:  $x$ -displacements (px) calculated using digital image correlation. Right:  $y$ -displacement (px).

- (7) Along the outer boundary of the domain, the observed displacements are prescribed as a boundary condition for the inverse analysis.
- (8) The material parameters are seeded with values of 1.0.
- (9) The peridynamics model is inverted for  $k$  and  $\mu$  until the objective function is minimized (the computed displacements from the peridynamics model match the observed image correlation displacements).

The differential method presented in [Sutton et al. 2009] was used to perform the image correlation. Bilinear interpolation was used to achieve subpixel accuracy. The digital microscope was calibrated such that 1 pixel is equivalent to 0.0147 mm. A mesh spacing of 50 pixels was used for the computed results for both the image correlation and the inverse analysis. The experimental displacements, calculated by the image correlation algorithm are shown in Figure 8.

The material parameters determined by the inverse analysis are presented in Table 2 and the error in the computed displacements is shown in Figure 9. Table 2 also shows the range of reported values in the literature. Note that the inverted material parameters fall within the reported range. Using the inverted

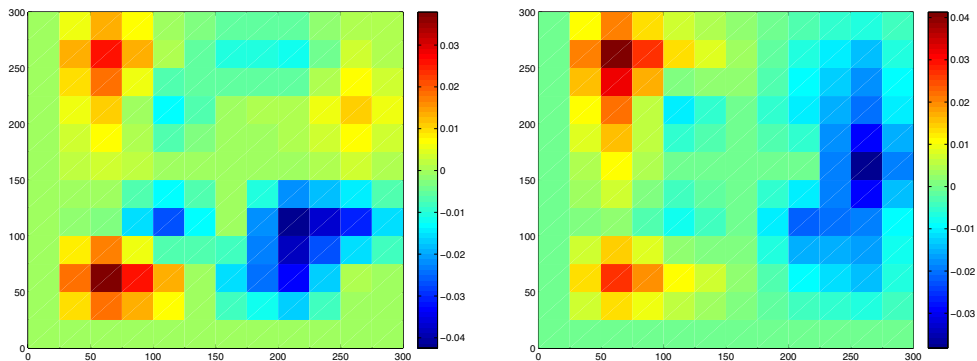


**Figure 9.** Left: error in the  $x$ -displacements (px) calculated using the inverted material parameters. Right:  $y$ -displacement error (px).



| Parameter | Reported Range (GPa) | Computed (GPa) |
|-----------|----------------------|----------------|
| $k$       | 2.3–15.3             | 9.18           |
| $\mu$     | 1.7–11.5             | 6.77           |

**Table 2.** Results for inversion problem using digital image correlation.

material parameters, Poisson’s ratio is calculated as  $\nu = 0.204$  which is close to the value of  $\nu = 0.2$  commonly used for nuclear graphite.

**5. Inversion for load state given fracture parameters**

The framework presented above can also be used to determine the state of loading given observed fracture parameters such as the crack aperture. Consider an alternative objective function given as

$$g(h) = \frac{1}{2} \sum_{j=1}^{N_{\text{obs}}} \int_{\Omega} (h - h^*)^2 \delta(\mathbf{x} - \mathbf{x}_j) d\mathbf{x} \tag{28}$$

where  $h^*$  is the measured value of the crack aperture at location  $\mathbf{x}_j$  and  $h$  is the computed crack aperture in the simulation. The decision variable in this case is the loading applied to the material,  $\mathbf{d} = [F_y]$ . Under these modifications, we optimize for the loading that results in a fracture with the same aperture as the observed value.

The geometry and boundary conditions for this problem are shown in Figure 10. The material parameters are given as  $k = 66.7$  GPa and  $\mu = 40$  GPa. The initial crack length,  $a$  was 1.0mm. The boundary conditions include a constant applied loading,  $F_y$  applied to a strip of width  $2\delta$  along the top of the domain. The displacement was constrained along a strip of width  $2\delta$  along the bottom of the domain.

A comparison of the inverted value for the loading given the crack aperture is shown in Figure 11. The observed values for the crack aperture were obtained by solving the forward problem for various magnitudes of the loading  $F_y$  and taking the relative distance between points on either side of the resulting fracture. A critical stretch damage model was used in the forward problem in which bonds that are stretched beyond a critical stretch break and no longer contribute to the material stiffness. The critical

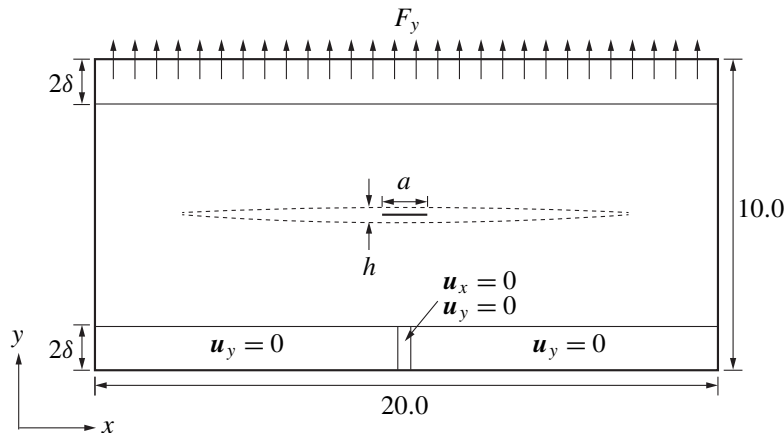


**Figure 10.** Geometry and boundary conditions for the load state inversion problem.

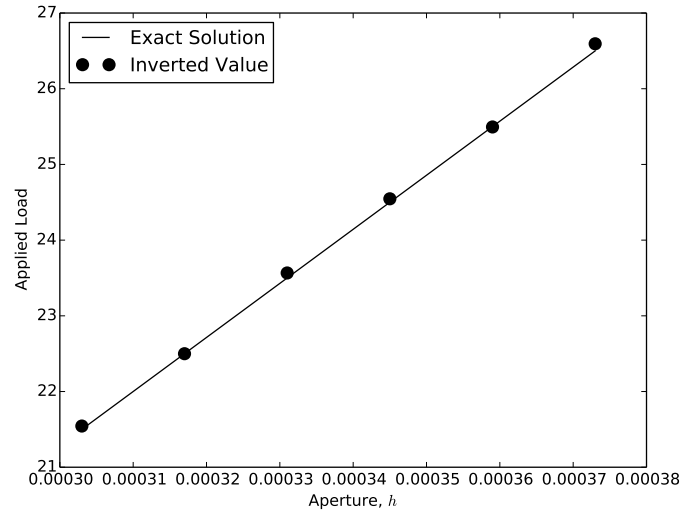


**Figure 11.** Inverted load state vs. exact value for the load state inversion problem.

stretch value for this problem was 0.001. The exact solution for the applied loading is represented by the loading used in the forward problem to obtain the observed crack apertures. The inverted value for the load state matches closely the exact solution suggesting that this approach to inverting for the load state is quite robust. Note that our inversion approach can solve for material properties in this dataset with minimal effort.

## 6. Conclusions

We have presented an adjoint-based methodology for peridynamics inverse problems and shown by means of several numerical examples, that this method can be used effectively to determine material properties for heterogeneous materials. We have also presented a framework for determining material properties that integrates digital image correlation with peridynamics inverse analysis. We have illustrated that this framework can be used to determine the load state of a material given observed fracture parameters such as the crack aperture. This peridynamics inversion capability can be used in a variety of engineering applications and provides a robust method to calibrate peridynamical models from sparse field or experimental measurements. While the solution of inverse problems in finite-element PDE based approaches may pose challenges associated with fractures, peridynamics presents a natural environment for inverse problems with discontinuities.

## Acknowledgments

Sandia National Laboratories is a multiprogram laboratory managed and operated by Sandia Corporation, a wholly owned subsidiary of Lockheed Martin Corporation, for the U.S. Department of Energy's National Nuclear Security Administration under contract DE-AC04-94AL85000.

The authors would like to thank Thorsten Becker, Johan Conradie, and Matt Molteno from Stellenbosch University for their assistance with the nuclear graphite experiments. Portions of this work were funded by the Institute for Structural Engineering at Stellenbosch University.

## References

- [Akçelik et al. 2006] V. Akçelik, G. Biros, O. Ghattas, J. Hill, D. Keyes, and B. van Bloemen Waanders, “Parallel algorithms for PDE-constrained optimization”, pp. 291–322 in *Parallel processing for scientific computing*, edited by M. A. Heroux et al., Society for Industrial and Applied Mathematics, Philadelphia, 2006.
- [Alali et al. 2014] B. Alali, K. Liu, and M. Gunzburger, “A generalized nonlocal calculus with application to the peridynamics model for solid mechanics”, preprint, 2014. arXiv 1402.0271v1
- [Asmaro 2013] W. P. Asmaro, *Identification of concrete fracture parameters using digital image correlation and inverse analysis*, Ph.D. thesis, University of Windsor, 2013, Available at <http://scholar.uwindsor.ca/etd/4952>.
- [van Bloemen Waanders et al. 2005] B. G. van Bloemen Waanders, R. A. Bartlett, S. S. Collis, E. R. Keiter, C. C. Ober, T. M. Smith, V. Akcelik, O. Ghattas, J. C. Hill, M. Berggren, M. Heinkenschloss, and L. C. Wilcox, “Sensitivity technologies for large scale simulation”, technical report SAND2004-6574, Sandia National Laboratories, 2005.
- [Chu et al. 1985] T. C. Chu, W. F. Ranson, M. A. Sutton, and W. H. Peters, “Applications of digital-image-correlation techniques to experimental mechanics”, *Exp. Mech.* **25**:3 (1985), 232–244.
- [Du et al. 2013a] Q. Du, M. Gunzburger, R. B. Lehoucq, and K. Zhou, “Analysis of the volume-constrained peridynamic Navier equation of linear elasticity”, *J. Elasticity* **113**:2 (2013), 193–217.
- [Du et al. 2013b] Q. Du, M. Gunzburger, R. B. Lehoucq, and K. Zhou, “A nonlocal vector calculus, nonlocal volume-constrained problems, and nonlocal balance laws”, *Math. Models Methods Appl. Sci.* **23**:3 (2013), 493–540.
- [Grédiac 2004] M. Grédiac, “The use of full-field measurement methods in composite material characterization: interest and limitations”, *Compos. Part A Appl. S.* **35**:7–8 (2004), 751–761.
- [Gunzburger and Lehoucq 2010] M. Gunzburger and R. B. Lehoucq, “A nonlocal vector calculus with application to nonlocal boundary value problems”, *Multiscale Model. Simul.* **8**:5 (2010), 1581–1598.
- [Hild and Roux 2006] F. Hild and S. Roux, “Digital image correlation: from displacement measurement to identification of elastic properties – a review”, *Strain* **42**:2 (2006), 69–80.
- [Le et al. 2014] Q. V. Le, W. K. Chan, and J. Schwartz, “A two-dimensional *ordinary*, state-based peridynamic model for linearly elastic solids”, *Internat. J. Numer. Methods Engrg.* **98**:8 (2014), 547–561.
- [Mengesha and Du 2014] T. Mengesha and Q. Du, “Nonlocal constrained value problems for a linear peridynamic Navier equation”, *J. Elasticity* **116**:1 (2014), 27–51.
- [Mengesha and Du 2015] T. Mengesha and Q. Du, “On the variational limit of a class of nonlocal functionals related to peridynamics”, *Nonlinearity* **28**:11 (2015), 3999–4035.
- [Pan et al. 2009] B. Pan, K. Qian, H. Xie, and A. Asundi, “Two-dimensional digital image correlation for in-plane displacement and strain measurement: a review”, *Meas. Sci. Technol.* **20**:6 (2009), 062001.
- [Périeré et al. 2009] J. N. Périeré, H. Leclerc, S. Roux, and F. Hild, “Digital image correlation and biaxial test on composite material for anisotropic damage law identification”, *Int. J. Solids and Struct.* **46**:11–12 (2009), 2388–2396.
- [Silling 2000] S. A. Silling, “Reformulation of elasticity theory for discontinuities and long-range forces”, *J. Mech. Phys. Solids* **48**:1 (2000), 175–209.
- [Silling and Askari 2005] S. A. Silling and E. Askari, “A meshfree method based on the peridynamic model of solid mechanics”, *Comput. Struct.* **83**:17–18 (2005), 1526–1535.
- [Silling and Lehoucq 2008] S. A. Silling and R. B. Lehoucq, “Convergence of peridynamics to classical elasticity theory”, *J. Elasticity* **93**:1 (2008), 13–37.
- [Silling et al. 2007] S. A. Silling, M. Epton, O. Weckner, J. Xu, and E. Askari, “Peridynamic states and constitutive modeling”, *J. Elasticity* **88**:2 (2007), 151–184.
- [Sutton et al. 2009] M. A. Sutton, J.-J. Orteu, and H. W. Schreier, *Image correlation for shape, motion and deformation measurements: basic concepts, theory and applications*, Springer, New York, 2009.
- [Tikhonov and Arsenin 1977] A. N. Tikhonov and V. Y. Arsenin, *Solutions of ill-posed problems*, Winston, Washington, DC, 1977.

Received 26 Nov 2014. Revised 5 Nov 2015. Accepted 7 Nov 2015.

DANIEL Z. TURNER: [dzturne@sandia.gov](mailto:dzturne@sandia.gov)

*Multiscale Science, Sandia National Laboratories, P.O. Box 5800, Albuquerque, NM 87185, United States*

BART G. VAN BLOEMEN WAANDERS: [bartv@sandia.gov](mailto:bartv@sandia.gov)

*Optimization and UQ, Sandia National Laboratories, P.O. Box 5800, Albuquerque, NM 87185, United States*

MICHAEL L. PARKS: [mlparks@sandia.gov](mailto:mlparks@sandia.gov)

*Computational Mathematics, Sandia National Laboratories, P.O. Box 5800, Albuquerque, NM 87185, United States*



## VARIABLE HORIZON IN A PERIDYNAMIC MEDIUM

STEWART A. SILLING, DAVID J. LITTLEWOOD AND PABLO SELESÓN

A notion of material homogeneity is proposed for peridynamic bodies with variable horizon but constant bulk properties. A relation is derived that scales the force state according to the position-dependent horizon while keeping the bulk properties unchanged. Using this scaling relation, if the horizon depends on position, artifacts called ghost forces may arise in a body under a homogeneous deformation. These artifacts depend on the second derivative of the horizon and can be reduced by employing a modified equilibrium equation using a new quantity called the *partial stress*. Bodies with piecewise constant horizon can be modeled without ghost forces by using a simpler technique called a *splice*. As a limiting case of zero horizon, both the partial stress and splice techniques can be used to achieve local–nonlocal coupling. Computational examples, including dynamic fracture in a one-dimensional model with local–nonlocal coupling, illustrate the methods.

### 1. Introduction

The peridynamic theory is a strongly nonlocal formulation of solid mechanics, based on long-range forces, that is adapted to the study of continuous bodies with evolving discontinuities, including cracks [Silling 2000; Silling et al. 2007; Silling and Lehoucq 2010]. Each material point  $\mathbf{x}$  in the reference configuration of a body  $\mathcal{B}$  interacts through the material model with other material points within a distance  $\delta(\mathbf{x})$  of itself. The maximum interaction distance  $\delta(\mathbf{x})$  is called the *horizon* of  $\mathbf{x}$ . The material points within the horizon of  $\mathbf{x}$  comprise a set called the *material family* of  $\mathbf{x}$ :

$$\mathcal{F}_x = \{\mathbf{q} \in \mathcal{B} : 0 < |\mathbf{q} - \mathbf{x}| \leq \delta(\mathbf{x})\},$$

where  $|\cdot|$  denotes the Euclidean norm. The vector from  $\mathbf{x}$  to any neighboring material point  $\mathbf{q} \in \mathcal{F}_x$ ,  $\boldsymbol{\xi} = \mathbf{q} - \mathbf{x}$ , is called a *bond*. The set of bonds from  $\mathbf{x}$  to its neighbors within its horizon is called the *family* of  $\mathbf{x}$ , denoted  $\mathcal{H}_x$ :

$$\mathcal{H}_x = \{\boldsymbol{\xi} \in \mathbb{R}^3 : \mathbf{x} + \boldsymbol{\xi} \in \mathcal{F}_x\}.$$

In an elastic peridynamic solid, the strain energy density  $W(\mathbf{x})$  is determined by the collective deformation of  $\mathcal{F}_x$ . To express this collective deformation, it is convenient to define the function

$$\underline{\mathbf{Y}}[\mathbf{x}, t](\cdot) : \mathcal{H}_x \rightarrow \mathbb{R}^3$$

that maps bonds into their images under the deformation  $\mathbf{y}$ . For any material point  $\mathbf{q} \in \mathcal{F}_x$  at time  $t \geq 0$ , let

$$\underline{\mathbf{Y}}[\mathbf{x}, t](\mathbf{q} - \mathbf{x}) = \mathbf{y}(\mathbf{q}, t) - \mathbf{y}(\mathbf{x}, t). \quad (1-1)$$

Sandia is a multiprogram laboratory operated by Sandia Corporation, a Lockheed Martin Company, for the United States Department of Energy's National Nuclear Security Administration under contract DE-AC04-94AL85000.

*Keywords:* elasticity, nonlocality, local–nonlocal coupling, peridynamics.

The function  $\underline{Y}[\mathbf{x}, t](\cdot)$  is an example of a *state*, which is a mapping with domain  $\mathcal{H}_x$ . By convention, the bond  $\xi \in \mathcal{H}_x$  that a state operates on is written in angle brackets, i.e.,  $\langle \xi \rangle$ . The state  $\underline{Y}[\mathbf{x}, t]$  is called the *deformation state* at  $\mathbf{x}$  and at time  $t$ . The deformation state is the basic kinematical quantity for purposes of material modeling, and, in this role, it is analogous to the deformation gradient in the classical theory of continuum mechanics,  $\mathbf{F} = \partial \mathbf{y} / \partial \mathbf{x}$ .

In the present discussion, for convenience, we will adopt the generalization that a state operating on a bond vector outside of the family of a given point  $\mathbf{x}$  is defined, but its value is zero:

$$|\xi| > \delta(\mathbf{x}) \implies \underline{A}[\mathbf{x}](\xi) = \mathbf{0}.$$

The inner product of two states  $\underline{A}$  and  $\underline{B}$  is defined by

$$\underline{A} \bullet \underline{B} = \int_{\mathcal{H}} \underline{A}(\xi) \cdot \underline{B}(\xi) dV_{\xi}. \quad (1-2)$$

In (1-2) and the rest of this paper, we use the symbol  $\mathcal{H}$  instead of  $\mathcal{H}_x$  when it is not necessary to refer to a specific  $\mathbf{x} \in \mathcal{B}$ . The *norm* of a state  $\underline{A}$  is defined by

$$\|\underline{A}\| = \sqrt{\underline{A} \bullet \underline{A}}.$$

In an elastic material, the strain energy density  $W(\mathbf{x})$  depends through the material model on the deformation state, and this dependence is written as

$$W(\mathbf{x}) = \widehat{W}(\underline{Y}[\mathbf{x}]).$$

When manipulating functions of states such as  $W$ , it is helpful to introduce the *Fréchet derivative*. Given the function  $\widehat{W}(\underline{Y})$ , its Fréchet derivative  $\widehat{W}_{\underline{Y}}$  is a functional derivative with the property that if  $\delta \underline{Y}$  is a small increment in the deformation state, then

$$\widehat{W}(\underline{Y} + \delta \underline{Y}) = \widehat{W}(\underline{Y}) + \widehat{W}_{\underline{Y}}(\underline{Y}) \bullet \delta \underline{Y} + o(\|\delta \underline{Y}\|). \quad (1-3)$$

Note that  $\widehat{W}_{\underline{Y}}$  is a state-valued function even though  $\widehat{W}$  is scalar-valued.

Let  $\Phi_y$  denote the total potential energy in a bounded elastic body  $\mathcal{B}$  under external force density field  $\mathbf{b}$ , subjected to the deformation  $\mathbf{y}$ :

$$\Phi_y = \int_{\mathcal{B}} (W(\mathbf{x}) - \mathbf{b}(\mathbf{x}) \cdot \mathbf{y}(\mathbf{x})) dV_x. \quad (1-4)$$

To derive the Euler–Lagrange equation corresponding to stationary values of this functional, set the first variation of (1-4) to zero. Combining (1-1), (1-3), and (1-4), and neglecting higher-order terms in the small increment in the deformation state, leads to

$$\begin{aligned} 0 &= \delta \Phi_y = \int_{\mathcal{B}} (\delta W(\mathbf{x}) - \mathbf{b}(\mathbf{x}) \cdot \delta \mathbf{y}(\mathbf{x})) dV_x \\ &= \int_{\mathcal{B}} (\widehat{W}_{\underline{Y}}(\underline{Y}[\mathbf{x}]) \bullet \delta \underline{Y}[\mathbf{x}] - \mathbf{b}(\mathbf{x}) \cdot \delta \mathbf{y}(\mathbf{x})) dV_x \\ &= \int_{\mathcal{B}} \left( \int_{\mathcal{B}} \widehat{W}_{\underline{Y}}(\underline{Y}[\mathbf{x}]) \langle \mathbf{q} - \mathbf{x} \rangle \cdot (\delta \mathbf{y}(\mathbf{q}) - \delta \mathbf{y}(\mathbf{x})) dV_q - \mathbf{b}(\mathbf{x}) \cdot \delta \mathbf{y}(\mathbf{x}) \right) dV_x. \end{aligned}$$

Using the change of dummy variables  $\mathbf{q} \leftrightarrow \mathbf{x}$  to eliminate  $\delta \mathbf{y}(\mathbf{q})$ , we obtain

$$0 = \int_{\mathcal{B}} \left( \int_{\mathcal{B}} (\widehat{W}_{\underline{Y}}(\underline{Y}[\mathbf{q}])(\mathbf{x} - \mathbf{q}) - \widehat{W}_{\underline{Y}}(\underline{Y}[\mathbf{x}])(\mathbf{q} - \mathbf{x})) dV_{\mathbf{q}} - \mathbf{b}(\mathbf{x}) \right) \cdot \delta \mathbf{y}(\mathbf{x}) dV_{\mathbf{x}}.$$

Since this must hold for every choice of the variation  $\delta \mathbf{y}$ , the Euler–Lagrange equation, which is the peridynamic equilibrium equation, is given by

$$\mathbf{L}^{\text{pd}}(\mathbf{x}) + \mathbf{b}(\mathbf{x}) = \mathbf{0} \quad (1-5)$$

for all  $\mathbf{x} \in \mathcal{B}$ . In (1-5), the *peridynamic internal force density* at  $\mathbf{x}$  is given by

$$\mathbf{L}^{\text{pd}}(\mathbf{x}) := \int_{\mathcal{B}} \{ \underline{\mathbf{T}}[\mathbf{x}](\mathbf{q} - \mathbf{x}) - \underline{\mathbf{T}}[\mathbf{q}](\mathbf{x} - \mathbf{q}) \} dV_{\mathbf{q}}, \quad (1-6)$$

where  $\underline{\mathbf{T}}[\mathbf{x}]$  is the *force state* at  $\mathbf{x}$ , which is related to the strain energy density by

$$\underline{\mathbf{T}}[\mathbf{x}] = \widehat{W}_{\underline{Y}}(\underline{Y}[\mathbf{x}]). \quad (1-7)$$

The *pairwise bond force density*  $\mathbf{f}$  on a point  $\mathbf{x}$  due to its interaction with any point  $\mathbf{q} \in \mathcal{F}_{\mathbf{x}}$  is given by

$$\mathbf{f}(\mathbf{q}, \mathbf{x}) = \underline{\mathbf{T}}[\mathbf{x}](\mathbf{q} - \mathbf{x}) - \underline{\mathbf{T}}[\mathbf{q}](\mathbf{x} - \mathbf{q}). \quad (1-8)$$

The peridynamic internal force density (1-6) may be written more succinctly in terms of the pairwise bond force density as

$$\mathbf{L}^{\text{pd}}(\mathbf{x}) = \int_{\mathcal{B}} \mathbf{f}(\mathbf{q}, \mathbf{x}) dV_{\mathbf{q}}. \quad (1-9)$$

In general,

$$\underline{\mathbf{T}}[\mathbf{x}] = \widehat{\underline{\mathbf{T}}}(\underline{Y}[\mathbf{x}]) \quad \text{and} \quad \underline{\mathbf{T}}[\mathbf{q}] = \widehat{\underline{\mathbf{T}}}(\underline{Y}[\mathbf{q}]),$$

where  $\widehat{\underline{\mathbf{T}}}$  is the material model expressed in terms of the force state.

By invoking d'Alembert's principle, the dynamic form of the balance of linear momentum is found from (1-5) to be

$$\rho(\mathbf{x}) \ddot{\mathbf{y}}(\mathbf{x}, t) = \mathbf{L}^{\text{pd}}(\mathbf{x}, t) + \mathbf{b}(\mathbf{x}, t) \quad (1-10)$$

for all  $\mathbf{x} \in \mathcal{B}$  and for any  $t \geq 0$ , where  $\rho$  is the mass density.

The mechanical interpretation of the force state is that  $\underline{\mathbf{T}}[\mathbf{x}](\mathbf{q} - \mathbf{x})$  represents a bond force density on  $\mathbf{x}$  due to its interaction with  $\mathbf{q}$ . More general material models, whether elastic or not, may be written in the form

$$\underline{\mathbf{T}}[\mathbf{x}] = \widehat{\underline{\mathbf{T}}}(\underline{Y}[\mathbf{x}], \dots, \mathbf{x}),$$

where  $\widehat{\underline{\mathbf{T}}}$  is the material model, which may depend on additional variables besides  $\underline{Y}$ . The dimensions of  $\underline{\mathbf{T}}$  and  $\mathbf{f}$  are force per unit volume squared. The dimensions of  $W$  are the same as in the classical theory, i.e., energy per unit volume.

If at any  $\mathbf{x}$ ,  $\underline{\mathbf{T}}$  depends only on  $\underline{Y}$  and  $\mathbf{x}$  (but not additional variables such as loading history), then the material model is *simple*, and we write

$$\underline{\mathbf{T}}[\mathbf{x}] = \widehat{\underline{\mathbf{T}}}(\underline{Y}[\mathbf{x}], \mathbf{x}).$$

All elastic materials are simple.

If  $\widehat{\underline{T}}$  has no explicit dependence on  $\mathbf{x}$ , then the body is *homogeneous*. If it is simple and homogeneous, we write

$$\underline{T}[\mathbf{x}] = \widehat{\underline{T}}(\underline{Y}[\mathbf{x}]).$$

Since  $\delta$  is in effect a material property, any homogeneous body has constant  $\delta$ .

If  $\delta$  is constant in  $\mathcal{B}$ , then the region of integration in (1-6) and (1-9) may be changed from  $\mathcal{B}$  to  $\mathcal{F}_x$ . The vast majority of applications of peridynamics to date assume constant horizon.

## 2. The peridynamic stress tensor

As shown in [Lehoucq and Silling 2008], given a continuously differentiable pairwise bond force density  $\mathbf{f}$  with asymptotic second-order decay with the bond length, the peridynamic internal force density can be expressed as

$$\underline{L}^{\text{pd}} = \nabla \cdot \nu^{\text{pd}} \quad \text{in } \mathcal{B},$$

where  $\nu^{\text{pd}}$  is the *peridynamic stress tensor* field defined for any  $\mathbf{x}$  by

$$\nu^{\text{pd}}(\mathbf{x}) := \frac{1}{2} \int_S \int_0^\infty \int_0^\infty (v+w)^2 \mathbf{f}(\mathbf{x} + v\mathbf{m}, \mathbf{x} - w\mathbf{m}) \otimes \mathbf{m} \, dw \, dv \, d\Omega_{\mathbf{m}}, \quad (2-1)$$

where  $S$  is the unit sphere,  $d\Omega_{\mathbf{m}}$  is a differential solid angle in the direction of the unit vector  $\mathbf{m}$ , and  $\mathbf{f}$  is given by (1-8).

Suppose the deformation is continuously differentiable, and let  $\underline{F}$  be the classical deformation gradient tensor field,

$$\underline{F} = \nabla \mathbf{y} \quad \text{in } \mathcal{B}.$$

Define the *deformation gradient state* field  $\underline{F}$  by

$$\underline{F}[\mathbf{x}](\xi) = \underline{F}(\mathbf{x})\xi \quad \text{for all } \mathbf{x} \in \mathcal{B} \text{ and } \xi \in \mathcal{H}_x. \quad (2-2)$$

An equivalent statement to (2-2) is

$$\underline{F} = \underline{F}\underline{X} \quad \text{in } \mathcal{B},$$

where  $\underline{X}$  is the *identity* state defined by

$$\underline{X}(\xi) = \xi \quad \text{for all } \xi \in \mathcal{H}_x.$$

Suppose the deformation is such that there is a tensor  $\underline{F}^*$  such that

$$\mathbf{y}(\mathbf{x} + \xi) - \mathbf{y}(\mathbf{x}) = \underline{F}^*\xi \quad \text{for all } \mathbf{x} \in \mathcal{B} \text{ and } \xi \in \mathcal{H}_x.$$

Then the deformation is called *uniform*. In this case,

$$\underline{Y} = \underline{F} \quad \text{in } \mathcal{B} \quad \text{and} \quad \underline{F}[\mathbf{x}](\xi) = \underline{F}^*\xi \quad \text{for all } \mathbf{x} \in \mathcal{B} \text{ and } \xi \in \mathcal{H}_x. \quad (2-3)$$



If the body is homogeneous and the deformation is uniform, then the peridynamic stress tensor is easily computed making use of the change of variables  $z = v + w$ :

$$\begin{aligned}
 \nu^{\text{pd}} &= \int_S \int_0^\infty \int_v^\infty z^2 \widehat{\underline{\mathbf{T}}}(\underline{\mathbf{F}})\langle z\mathbf{m} \rangle \otimes \mathbf{m} \, dz \, dv \, d\Omega_m \\
 &= \int_S \int_0^\infty \int_0^z z^2 \widehat{\underline{\mathbf{T}}}(\underline{\mathbf{F}})\langle z\mathbf{m} \rangle \otimes \mathbf{m} \, dv \, dz \, d\Omega_m \\
 &= \int_S \int_0^\infty z^3 \widehat{\underline{\mathbf{T}}}(\underline{\mathbf{F}})\langle z\mathbf{m} \rangle \otimes \mathbf{m} \, dz \, d\Omega_m \\
 &= \int_S \int_0^\infty \widehat{\underline{\mathbf{T}}}(\underline{\mathbf{F}})\langle z\mathbf{m} \rangle \otimes (z\mathbf{m})(z^2 \, dz \, d\Omega_m) \\
 &= \nu^0,
 \end{aligned}
 \tag{2-4}$$

where  $\nu^0$  is the *collapsed stress tensor* defined by

$$\nu^0 := \int_{\mathcal{H}} \widehat{\underline{\mathbf{T}}}(\underline{\mathbf{F}})\langle \xi \rangle \otimes \xi \, dV_\xi.
 \tag{2-5}$$

Also define the *collapsed internal force density* field by

$$\mathbf{L}^0 := \nabla \cdot \nu^0 \quad \text{in } \mathcal{B}.
 \tag{2-6}$$

As discussed in [Silling and Lehoucq 2008], the collapsed stress tensor is an admissible first Piola–Kirchhoff stress tensor whose constitutive model depends on the local deformation gradient tensor through (2-5). The collapsed internal force density field provides the “local limit of peridynamics” in the sense that as  $\delta \rightarrow 0$ ,

$$\mathbf{L}^{\text{pd}} \rightarrow \mathbf{L}^0,$$

provided that the deformation is twice continuously differentiable and  $\widehat{\underline{\mathbf{T}}}$  obeys the scaling relation derived in the next section.

### 3. Rescaling a material model at a point

The remainder of this paper concerns methods for allowing changes in the horizon as a function of position such that the “bulk properties” are invariant to this change. The first step is to specify what this required invariance means.

Suppose an elastic material model is given for a particular value of horizon (without loss of generality, we will assume that this horizon has the value 1), and denote the corresponding strain energy density function by  $\widehat{W}_1$ . Now consider a different value of horizon,  $\delta$ , and denote the corresponding strain energy density function by  $\widehat{W}$ . As a physical requirement, the strain energy density for any uniform deformation must be invariant with respect to changes in  $\delta$ . By reasoning similar to that in [Silling and Lehoucq 2008], it is assumed that for any deformation state  $\underline{\mathbf{Y}}$ ,

$$\widehat{W}(\underline{\mathbf{Y}}) = \widehat{W}_1(\underline{\mathbf{Y}}_1),
 \tag{3-1}$$

where  $\underline{Y}_1$  is the *reference deformation state* defined by

$$\underline{Y}_1\langle \mathbf{n} \rangle := \delta^{-1} \underline{Y}\langle \delta \mathbf{n} \rangle \quad \text{for all } \mathbf{n} \in \mathcal{H}_1, \quad (3-2)$$

where  $\mathcal{H}_1$  is the family of  $\mathbf{x}$  with horizon 1. In the remainder of this paper, the symbols  $\mathbf{n}$  or  $\mathbf{m}$  will generally be used instead of  $\xi$  to denote bonds in  $\mathcal{H}_1$ . To derive the force state  $\underline{T}$ , observe that (3-1) implies

$$\hat{W}_{\underline{Y}} \bullet d\underline{Y} = (\hat{W}_1)_{\underline{Y}_1} \bullet d\underline{Y}_1.$$

Hence, using (1-7),

$$\underline{T} \bullet d\underline{Y} = \underline{T}_1 \bullet d\underline{Y}_1.$$

Combining this with (1-2), (1-3), and (3-2) leads to the following scaling relation for peridynamic material models in three dimensions:

$$\hat{\underline{T}}(\underline{Y})\langle \xi \rangle = \delta^{-4} \hat{\underline{T}}_1(\underline{Y}_1)\langle \delta^{-1} \xi \rangle \quad \text{for all } \xi \in \mathcal{H}$$

for any deformation state  $\underline{Y}$  on  $\mathcal{H}$ . Repeating the above derivation for one- or two-dimensional models leads to

$$\hat{\underline{T}}(\underline{Y})\langle \xi \rangle = \delta^{-(1+D)} \hat{\underline{T}}_1(\underline{Y}_1)\langle \delta^{-1} \xi \rangle \quad \text{for all } \xi \in \mathcal{H}, \quad (3-3)$$

where  $D$  is the number of dimensions and  $\underline{Y}_1$  is given by (3-2). The state  $\hat{\underline{T}}_1$  is called the *reference material model*.

From (2-2) and (3-2), the deformation gradient state has the following invariance with respect to changes in  $\delta$ :

$$\underline{F}_1\langle \mathbf{n} \rangle = \delta^{-1} \underline{F}\langle \delta \mathbf{n} \rangle = \delta^{-1} \underline{F} \delta \mathbf{n} = \underline{F} \mathbf{n} = \underline{F}\langle \mathbf{n} \rangle \quad \text{for all } \mathbf{n} \in \mathcal{H}_1.$$

Hence,

$$\underline{F}_1 = \underline{F} \quad \text{in } \mathcal{H} \cap \mathcal{H}_1, \quad (3-4)$$

which is a result that could be anticipated owing to the fact that  $\underline{F}$  is dimensionless. From (2-5), (3-2) and (3-3),

$$\begin{aligned} v^0 &= \int_{\mathcal{H}} \hat{\underline{T}}(\underline{F})\langle \xi \rangle \otimes \xi \, dV_{\xi} \\ &= \int_{\mathcal{H}_1} \delta^{-(1+D)} \hat{\underline{T}}_1(\underline{F}_1)\langle \mathbf{n} \rangle \otimes (\delta \mathbf{n}) (\delta^D dV_{\mathbf{n}}) \\ &= \int_{\mathcal{H}_1} \hat{\underline{T}}_1(\underline{F}_1)\langle \mathbf{n} \rangle \otimes \mathbf{n} \, dV_{\mathbf{n}}, \end{aligned} \quad (3-5)$$

which shows that the collapsed stress tensor is also invariant with respect to changes in  $\delta$ . Note that this invariance does not require the body to be homogeneous.

#### 4. Variable scale homogeneous bodies

Recall from Section 1 that any homogeneous body necessarily has constant horizon. Therefore, it is necessary to define a relaxed concept of homogeneity that captures the meaning of having a peridynamic body with constant “bulk properties” without adhering to the strict definition of homogeneity. The reference material model defined in Section 3 provides a way to do this.

**Definition.** Suppose a reference material model  $\widehat{\underline{T}}_1$  is given in  $\mathcal{B}$ , independent of position. In addition, let the horizon  $\delta(\mathbf{x})$  be prescribed as a function of position. If, at any  $\mathbf{x} \in \mathcal{B}$ ,

$$\widehat{\underline{T}}(\underline{Y}[\mathbf{x}], \mathbf{x})\langle \underline{\xi} \rangle = \frac{1}{(\delta(\mathbf{x}))^{1+D}} \widehat{\underline{T}}_1(\underline{Y}_1[\mathbf{x}])\left\langle \frac{\underline{\xi}}{\delta(\mathbf{x})} \right\rangle \quad \text{for all } \underline{\xi} \in \mathcal{H}_{\mathbf{x}}, \tag{4-1}$$

then  $\mathcal{B}$  is a *variable scale homogeneous* (VSH) body. Note that a homogeneous body is a VSH body with constant horizon.

By the results of Section 3, an elastic VSH body under uniform deformation has constant  $W$ . However, it does *not* necessarily have constant  $\nu^{\text{pd}}$  and is therefore not necessarily in equilibrium in the absence of body forces. (Recall that (2-4) applies only to homogeneous bodies, and homogeneity implies that  $\delta$  is constant.) As shown in the next section, nonconstant  $\delta$  in a VSH body leads to *ghost forces* at points where the horizon changes.

### 5. Ghost forces

We demonstrate that in the absence of body forces, a uniform deformation of a VSH body is not necessarily in equilibrium. To see this, assume a uniform deformation, take  $\delta$  to be twice continuously differentiable, and compute the net internal force density  $\mathbf{L}^{\text{pd}}(\mathbf{x})$ . Extending the integration domain in (1-6) to the entire space for convenience, and using (4-1), we obtain, for any  $\mathbf{x}$ ,

$$\begin{aligned} \mathbf{L}^{\text{pd}}(\mathbf{x}) &= \int_{\mathbb{R}^3} \{ \underline{T}[\mathbf{x}]\langle \mathbf{q} - \mathbf{x} \rangle - \underline{T}[\mathbf{q}]\langle \mathbf{x} - \mathbf{q} \rangle \} dV_{\mathbf{q}} \\ &= \int_{\mathbb{R}^3} \{ \delta^{-(1+D)}(\mathbf{x}) \underline{T}_1\langle \mathbf{m} \rangle - \delta^{-(1+D)}(\mathbf{q}) \underline{T}_1\langle \mathbf{n} \rangle \} dV_{\mathbf{q}}, \end{aligned} \tag{5-1}$$

where

$$\mathbf{m} = \frac{\mathbf{q} - \mathbf{x}}{\delta(\mathbf{x})} \quad \text{and} \quad \mathbf{n} = \frac{\mathbf{x} - \mathbf{q}}{\delta(\mathbf{q})}. \tag{5-2}$$

Holding  $\mathbf{x}$  fixed,

$$dV_{\mathbf{q}} = \left| \det \left( \frac{\partial \mathbf{m}}{\partial \mathbf{q}} \right) \right|^{-1} dV_{\mathbf{m}} = \delta^D(\mathbf{x}) dV_{\mathbf{m}}, \tag{5-3}$$

$$dV_{\mathbf{q}} = \left| \det \left( \frac{\partial \mathbf{n}}{\partial \mathbf{q}} \right) \right|^{-1} dV_{\mathbf{n}} = \frac{\delta^D(\mathbf{q})}{1 + \mathbf{n} \cdot \nabla \delta(\mathbf{q}) + O(|\nabla \delta|^2)} dV_{\mathbf{n}}. \tag{5-4}$$

From (5-1)–(5-4), it follows that

$$\begin{aligned} \mathbf{L}^{\text{pd}}(\mathbf{x}) &= \int_{\mathbb{R}^3} \frac{\underline{T}_1\langle \mathbf{m} \rangle}{\delta(\mathbf{x})} dV_{\mathbf{m}} - \int_{\mathbb{R}^3} \frac{\underline{T}_1\langle \mathbf{n} \rangle}{\delta(\mathbf{q})} \left( \frac{1}{1 + \mathbf{n} \cdot \nabla \delta(\mathbf{q}) + O(|\nabla \delta|^2)} \right) dV_{\mathbf{n}} \\ &= \int_{\mathbb{R}^3} \epsilon(\mathbf{x}, \mathbf{q}) \underline{T}_1\langle \mathbf{m} \rangle dV_{\mathbf{m}}, \end{aligned} \tag{5-5}$$

where

$$\begin{aligned}\epsilon(\mathbf{x}, \mathbf{q}) &= \frac{1}{\delta(\mathbf{x})} - \frac{1}{\delta(\mathbf{q})} \left( \frac{1}{1 + \mathbf{n} \cdot \nabla \delta(\mathbf{q}) + O(|\nabla \delta|^2)} \right) \\ &= \frac{1}{\delta(\mathbf{x})} - \frac{1}{\delta(\mathbf{q}) + \nabla \delta(\mathbf{q}) \cdot (\mathbf{x} - \mathbf{q}) + O(\delta |\nabla \delta|^2)}.\end{aligned}\quad (5-6)$$

Now approximate  $\delta(\mathbf{x})$  by the first three terms of a Taylor expansion around  $\mathbf{q}$ , that is,

$$\delta(\mathbf{x}) = \delta(\mathbf{q}) + \nabla \delta(\mathbf{q}) \cdot (\mathbf{x} - \mathbf{q}) + \frac{1}{2} \nabla \nabla \delta(\mathbf{q}) (\boldsymbol{\xi} \otimes \boldsymbol{\xi}) + \dots,$$

where  $\boldsymbol{\xi} = \mathbf{q} - \mathbf{x}$ . Using this to eliminate the term  $\nabla \delta(\mathbf{q}) \cdot (\mathbf{x} - \mathbf{q})$  in (5-6) leads, after further straightforward manipulations, to

$$\epsilon(\mathbf{x}, \mathbf{q}) = \frac{1}{\delta(\mathbf{x})} - \frac{1}{\delta(\mathbf{x}) - \frac{1}{2} \nabla \nabla \delta(\mathbf{q}) (\boldsymbol{\xi} \otimes \boldsymbol{\xi}) + \dots} = -\frac{1}{2} \nabla \nabla \delta(\mathbf{q}) \mathbf{m} \otimes \mathbf{m} + \dots,$$

where  $\mathbf{m}$  is given by (5-2). From this result and (5-5), the peridynamic internal force density at  $\mathbf{x}$  is estimated from

$$\mathbf{L}^{\text{pd}}(\mathbf{x}) = -\frac{1}{2} \int_{\mathbb{R}^3} \nabla \nabla \delta(\mathbf{q}) (\mathbf{m} \otimes \mathbf{m}) \underline{\mathbf{T}}_1 \langle \mathbf{m} \rangle dV_{\mathbf{m}} + \dots.$$

We thus obtain

$$|\mathbf{L}^{\text{pd}}(\mathbf{x})| \leq \frac{1}{2} \int_{\mathbb{R}^3} \max_{\mathcal{H}_x} \{ |\nabla \nabla \delta| \} |\mathbf{m} \otimes \mathbf{m}| |\underline{\mathbf{T}}_1 \langle \mathbf{m} \rangle| dV_{\mathbf{m}} + \dots.$$

Since, by assumption,  $\delta$  is twice continuously differentiable, and since  $|\mathbf{m}| \leq 1$ , this result implies

$$\mathbf{L}^{\text{pd}}(\mathbf{x}) = O(|\nabla \nabla \delta|) O(\|\underline{\mathbf{T}}_1\|). \quad (5-7)$$

The departure from equilibrium represented by nonzero values of  $\mathbf{L}^{\text{pd}}$  is called *ghost force* and is an artifact of the position dependence of the horizon. Observe that the leading term in the ghost force depends on the *second* derivative of  $\delta$ . In fact, it can be shown directly that if  $\delta$  is a linear function of position, then the ghost force vanishes.

An illustration of the effect of ghost force in a VSH bar in equilibrium is shown in Figure 1. The

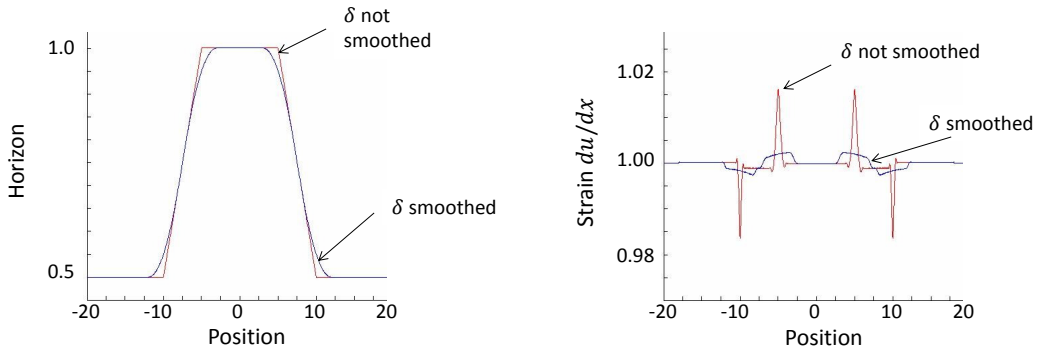


**Figure 1.** Ghost strain in a VSH body in equilibrium. Left: horizon as a function of position. Right: strain as a function of position.

peridynamic reference material model  $\widehat{\underline{T}}_1$  is a bond-based model [Silling 2000] with a nominal Young’s modulus of 1. The horizon in the bar depends on position as shown in the left figure. The numerical approximation method is discussed in the Appendix. Two cases are considered for the spatial dependence of the horizon: piecewise linear (“not smoothed”) and cubic spline (“smoothed”). The ends of the bar have prescribed displacements corresponding to a nominal strain in the bar of 1. The strain (defined as  $du/dx$ ) in equilibrium for the two cases is shown in the right figure. The strain is computed numerically using a central finite difference formula. If there were no ghost forces, the strain would be constant and equal to 1. Because of ghost forces, anomalies in strain (“ghost strains”) appear that equilibrate the ghost forces. The smoothed  $\delta(x)$  has lower ghost strains than the nonsmoothed one. This result is consistent with (5-7), which predicts that ghost forces are proportional to the second derivative of  $\delta(x)$ .

In this example, the anomalies in strain are less than 2%, even for the nonsmoothed case. This departure from constant strain could be acceptable in many applications. Ghost forces in a VSH peridynamic body are always self-equilibrated, that is, they do not exert a net force on the body. This follows from the fact that the peridynamic equilibrium equation always conserves linear momentum, even if the material model depends on position. To address applications in which these ghost forces are not acceptable, or it is desired to have a jump in  $\delta(x)$ , we will introduce two methods, *partial stress* and *splice*, that exhibit zero ghost forces in a uniform deformation of a VSH body.

### 6. The partial stress field

We investigate a modified form of the momentum balance that eliminates ghost forces in a VSH body under a uniform deformation. The momentum balance is expressed in terms of a new field called the “partial stress” tensor field.

Consider a peridynamic body  $\mathcal{B}$  and let its force state field  $\underline{T}$  be given. Let the *partial stress* tensor field  $\nu^{\text{ps}}$  be defined by

$$\nu^{\text{ps}}(\mathbf{x}) := \int_{\mathcal{H}_x} \underline{T}[\mathbf{x}](\boldsymbol{\xi}) \otimes \boldsymbol{\xi} \, dV_{\boldsymbol{\xi}} \quad \text{for all } \mathbf{x} \in \mathcal{B}. \tag{6-1}$$

Also define the *partial internal force density* by

$$\underline{L}^{\text{ps}}(\mathbf{x}) := \nabla \cdot \nu^{\text{ps}}(\mathbf{x}) \quad \text{for all } \mathbf{x} \in \mathcal{B}. \tag{6-2}$$

If the material model is simple, the partial stress can be expressed in the form

$$\nu^{\text{ps}}(\mathbf{x}) = \widehat{\nu}^{\text{ps}}(\underline{Y}[\mathbf{x}]) \quad \text{for all } \mathbf{x} \in \mathcal{B},$$

where

$$\widehat{\nu}^{\text{ps}}(\underline{Y}) = \int_{\mathcal{H}} \widehat{\underline{T}}(\underline{Y})(\boldsymbol{\xi}) \otimes \boldsymbol{\xi} \, dV_{\boldsymbol{\xi}}. \tag{6-3}$$

Note the similarity between  $\nu^{\text{ps}}$  and  $\nu^0$  defined by (2-5). The difference is that  $\nu^{\text{ps}}$  depends on the (nonlocal) deformation state  $\underline{Y}$ , while  $\nu^0$  depends on the (local) deformation gradient tensor. In the special case of a uniform deformation of a homogeneous body (which implies  $\delta = \text{constant}$  and  $\underline{Y} = \underline{F}$ ), clearly  $\nu^{\text{ps}} \equiv \nu^0$ .

By repeating the manipulations leading to (3-5), it is easily shown that in a VSH body with reference material model  $\widehat{\underline{T}}_1$ ,

$$\nu^{\text{ps}}(\mathbf{x}) = \int_{\mathcal{H}_1} \widehat{\underline{T}}_1(\underline{\mathbf{Y}}_1[\mathbf{x}]) \langle \mathbf{n} \rangle \otimes \mathbf{n} dV_n \quad \text{for all } \mathbf{x} \in \mathcal{B}, \quad (6-4)$$

where  $\underline{\mathbf{Y}}_1$  is given by (3-2). Since, in a uniform deformation,  $\underline{\mathbf{Y}}_1$  is constant (and equal to  $\underline{\mathbf{F}}$ ), it follows from (2-3), (2-6), (3-4), (3-5), (6-2), and (6-4) that in a VSH body under a uniform deformation,

$$\nu^{\text{ps}} \equiv \nu^0 \quad \text{and} \quad \mathbf{L}^{\text{ps}} \equiv \mathbf{L}^0 \equiv \mathbf{0}. \quad (6-5)$$

This establishes that, for a VSH body under a uniform deformation, ghost forces are absent in the partial stress formulation of the momentum balance equation, regardless of the spatial dependence of horizon. This observation motivates the use of this modified momentum balance in the transition region of the horizon.

## 7. The partial stress as an approximation to peridynamics

With the intent of modeling some parts of a body using the partial internal force density (6-2) and other parts using the peridynamic internal force density (1-6), the relation between the two will now be investigated. Since the plan is to make a transition between  $\mathbf{L}^{\text{ps}}$  and  $\mathbf{L}^{\text{pd}}$  where the horizon is constant, we investigate the way these fields approximate each other under this assumption.

**Proposition 1.** *Let  $\mathcal{B}$  be a homogeneous body (which implies constant  $\delta$ ). Let a twice continuously differentiable deformation  $\mathbf{y}$  of  $\mathcal{B}$  be prescribed. Then*

$$\nu^{\text{pd}} - \nu^{\text{ps}} = O(\delta)O(\|\nabla \underline{\mathbf{T}}_1\|) \quad \text{in } \mathcal{B} \quad (7-1)$$

and

$$\mathbf{L}^{\text{pd}} - \mathbf{L}^{\text{ps}} = O(\delta)O(\|\nabla \nabla \underline{\mathbf{T}}_1\|) \quad \text{in } \mathcal{B}. \quad (7-2)$$

*Proof of (7-1).* Let  $\mathbf{x} \in \mathcal{B}$  be fixed. Combining (1-8), (2-1), and (4-1) leads to

$$\begin{aligned} \nu^{\text{pd}}(\mathbf{x}) &= \int_S \int_0^\infty \int_0^\infty (v+w)^2 \underline{\mathbf{T}}[\mathbf{x} - w\mathbf{m}] \langle (v+w)\mathbf{m} \rangle \otimes \mathbf{m} dw dv d\Omega_{\mathbf{m}} \\ &= \int_S \int_0^\infty \int_0^\infty (v_1+w_1)^2 \underline{\mathbf{T}}_1[\mathbf{x} - \delta w_1\mathbf{m}] \langle (v_1+w_1)\mathbf{m} \rangle \otimes \mathbf{m} dw_1 dv_1 d\Omega_{\mathbf{m}}, \end{aligned}$$

where  $v = \delta v_1$  and  $w = \delta w_1$ . A Taylor expansion for  $\underline{\mathbf{T}}_1$  yields

$$\underline{\mathbf{T}}_1[\mathbf{x} - \delta w_1\mathbf{m}] = \underline{\mathbf{T}}_1[\mathbf{x}] - \delta w_1 \nabla \underline{\mathbf{T}}_1[\mathbf{x}]\mathbf{m} + \dots$$

After repeating the manipulations leading up to (2-4), and after evaluating the triple integral, the first term in this Taylor expansion gives the partial stress defined by (6-1). Thus

$$\nu^{\text{pd}} = \nu^{\text{ps}} + O(\delta)O(\|\nabla \underline{\mathbf{T}}_1\|),$$

proving (7-1).

*Proof of (7-2).* Let  $\mathbf{x} \in \mathcal{B}$  be fixed. Applying a Taylor expansion to  $\underline{\mathbf{T}}[\mathbf{q}]$  around  $\mathbf{x}$  and setting  $\boldsymbol{\xi} = \mathbf{q} - \mathbf{x}$  leads to

$$\underline{\mathbf{T}}[\mathbf{q}] = \underline{\mathbf{T}}[\mathbf{x}] + \nabla \underline{\mathbf{T}}[\mathbf{x}] \boldsymbol{\xi} + \frac{1}{2} \nabla \nabla \underline{\mathbf{T}}[\mathbf{x}] (\boldsymbol{\xi} \otimes \boldsymbol{\xi}) + \dots .$$

Combining this with (1-6), we find

$$\begin{aligned} \mathbf{L}^{\text{pd}}(\mathbf{x}) &= \int_{\mathcal{H}_x} \{ \underline{\mathbf{T}}[\mathbf{x}] \langle \boldsymbol{\xi} \rangle - \underline{\mathbf{T}}[\mathbf{q}] \langle -\boldsymbol{\xi} \rangle \} dV_{\boldsymbol{\xi}} \\ &= \int_{\mathcal{H}_x} \left\{ \underline{\mathbf{T}}[\mathbf{x}] \langle \boldsymbol{\xi} \rangle - \left( \underline{\mathbf{T}}[\mathbf{x}] \langle -\boldsymbol{\xi} \rangle + \nabla \underline{\mathbf{T}}[\mathbf{x}] \langle -\boldsymbol{\xi} \rangle \boldsymbol{\xi} + \frac{1}{2} \nabla \nabla \underline{\mathbf{T}}[\mathbf{x}] \langle -\boldsymbol{\xi} \rangle (\boldsymbol{\xi} \otimes \boldsymbol{\xi}) + \dots \right) \right\} dV_{\boldsymbol{\xi}}. \end{aligned}$$

Replacing  $\boldsymbol{\xi}$  by  $-\boldsymbol{\xi}$ , the first two terms in the integrand cancel. Bringing the gradient operator in the third term of the integrand outside the integral yields

$$\begin{aligned} \mathbf{L}^{\text{pd}}(\mathbf{x}) &= \nabla \cdot \int_{\mathcal{H}_x} \underline{\mathbf{T}}[\mathbf{x}] \langle \boldsymbol{\xi} \rangle \otimes \boldsymbol{\xi} dV_{\boldsymbol{\xi}} - \frac{1}{2} \int_{\mathcal{H}_x} \nabla \nabla \underline{\mathbf{T}}[\mathbf{x}] \langle \boldsymbol{\xi} \rangle (\boldsymbol{\xi} \otimes \boldsymbol{\xi}) dV_{\boldsymbol{\xi}} + \dots \\ &= \mathbf{L}^{\text{ps}}(\mathbf{x}) - \frac{1}{2} \int_{\mathcal{H}_x} \nabla \nabla \underline{\mathbf{T}}[\mathbf{x}] \langle \boldsymbol{\xi} \rangle (\boldsymbol{\xi} \otimes \boldsymbol{\xi}) dV_{\boldsymbol{\xi}} + \dots . \end{aligned}$$

Using (3-3) to express the remainder in terms of the reference force state, and setting  $\boldsymbol{\xi} = \delta \mathbf{m}$ , this implies

$$\mathbf{L}^{\text{pd}}(\mathbf{x}) = \mathbf{L}^{\text{ps}}(\mathbf{x}) - \frac{\delta}{2} \int_{\mathcal{H}_1} \nabla \nabla \underline{\mathbf{T}}_1[\mathbf{x}] \langle \mathbf{m} \rangle (\mathbf{m} \otimes \mathbf{m}) dV_{\mathbf{m}} + \dots .$$

Since  $|\mathbf{m}| \leq 1$ , this proves (7-2). □

Because of (7-2), it follows that at the interface between subregions where  $\mathbf{L}^{\text{ps}}$  and  $\mathbf{L}^{\text{pd}}$  are used in the momentum balance, there are no ghost forces if the deformation is uniform (since  $\underline{\mathbf{T}}_1$  is constant in  $\mathcal{B}$ ).

In Figure 2, we present an example of the propagation of a stress pulse in a VSH bar. The horizon increases from 0.1 on the left to 1.0 on the right through a transition region of thickness 0.1. The

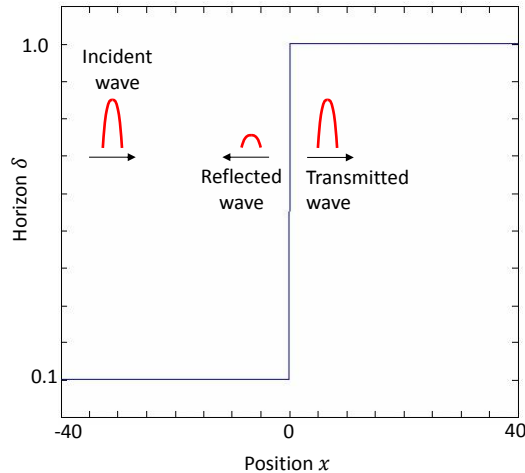


**Figure 2.** Stress pulse in a VSH bar: horizon as a function of position.

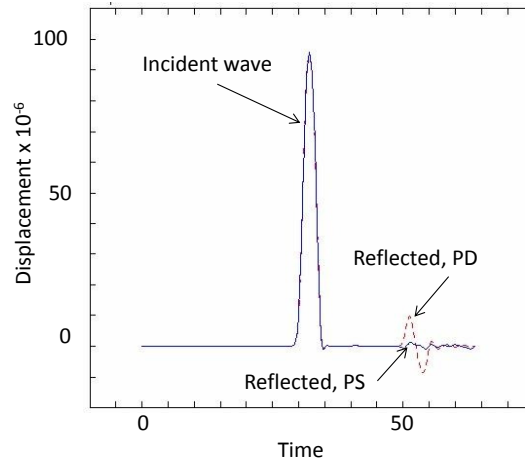


**Figure 3.** Stress pulse in a VSH bar: time history of displacement at  $x = -10$ . The two curves are for a fully peridynamic (PD) model, and for peridynamic with a partial stress (PS) region surrounding the transition in  $\delta$ . The PS curve has a different reflection than the PD model.

numerical approximation method is discussed in the Appendix. An incident wave pulse is applied on the left boundary. The total thickness of the pulse is 4.0, which is thin enough that we expect to see some effect of nonlocality as the pulse moves into the high- $\delta$  region. Two cases are considered: (1) the full peridynamic equation applied throughout the domain, and (2) the partial stress model applied in a region containing and surrounding the transition region with the full peridynamic equation applied everywhere else. In case (2), the total width of the partial stress region is 10. Figure 3 compares the time history of the displacement at the point  $x = -10$  for the two cases, showing both the incident and reflected pulses. Evidently, the use of the partial stress model in the transition region reduces the reflections. Figure 4 shows the comparison at the point  $x = 10$ , showing the transmitted pulses, which are essentially the same for both models. The change in shape of the transmitted pulse compared with the incident pulse is primarily due to nonlocality: as  $\delta$  increases, short wavelength components of the pulse experience a lower wave speed. This effect of nonlocality on wave speed is reflected in the dependence on the horizon of dispersion curves for linear waves [Silling and Lehoucq 2010; Seleson and Parks 2011].

This example illustrates that it is hopeless to try to find a coupling method that transmits waves without reflection between regions with different horizons. However, as the example demonstrates, different coupling methods can have different transmission and reflection properties that may be more or less desirable for different applications.

## 8. Partial stress as an approximation to the local theory

In Section 7, the relationship between the partial stress and the full peridynamic versions of the internal force density were discussed. Here, we investigate the approximate relationship between the partial stress formulation and the local theory. The appropriate material model in the local theory uses the collapsed



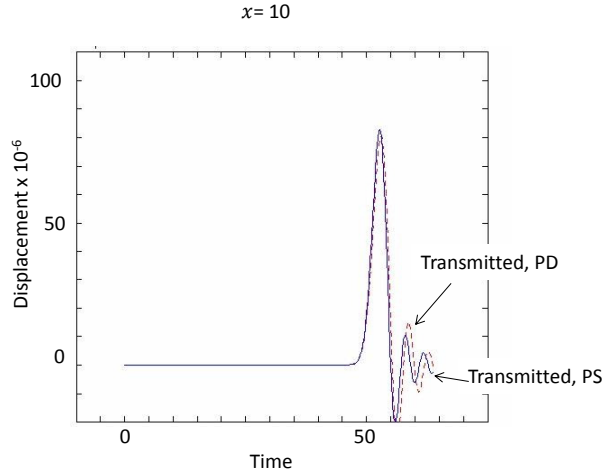


**Figure 4.** Stress pulse in a VSH bar: time history of displacement at  $x = 10$ . The transmitted pulses are similar between the two models, with the primary effect being the nonlocality of the material model.

stress tensor defined by (2-5), because, as shown in (6-5), it coincides with the partial stress for uniform deformations.

**Proposition 2.** *Let  $\mathcal{B}$  be a homogeneous body (which implies constant  $\delta$ ). Let the reference material model  $\hat{\underline{T}}_1$  be a continuously differentiable function (of the reference deformation state). Let  $\mathbf{y}$  be twice continuously differentiable in  $\mathcal{B}$ . Then*

$$v^{ps} - v^0 = O(\delta)O(\|\nabla \underline{T}_1\|) \quad \text{in } \mathcal{B}, \tag{8-1}$$

where  $v^{ps}$  and  $v^0$  are defined by (6-1) and (2-5), and

$$\underline{L}^{ps} - \underline{L}^0 = O(\delta)O(\|\nabla \nabla \underline{T}_1\|) \quad \text{in } \mathcal{B}, \tag{8-2}$$

where  $\underline{L}^{ps}$  and  $\underline{L}^0$  are defined by (6-2) and (2-6).

*Proof of (8-1).* Let  $\mathbf{x} \in \mathcal{B}$  be fixed. From (3-2) and a Taylor expansion of  $\mathbf{y}$  around  $\mathbf{x}$ ,

$$\begin{aligned} \underline{Y}_1[\mathbf{x}]\langle \mathbf{n} \rangle &= \delta^{-1}(\mathbf{y}(\mathbf{x} + \delta \mathbf{n}) - \mathbf{y}(\mathbf{x})) \\ &= \delta^{-1}((\mathbf{y}(\mathbf{x}) + \delta \mathbf{F}(\mathbf{x})\mathbf{n} + \frac{1}{2}\delta^2 \nabla \mathbf{F}(\mathbf{x})(\mathbf{n} \otimes \mathbf{n}) + \dots) - \mathbf{y}(\mathbf{x})). \\ &= \mathbf{F}(\mathbf{x})\mathbf{n} + \frac{1}{2}\delta \nabla \mathbf{F}(\mathbf{x})(\mathbf{n} \otimes \mathbf{n}) + \dots \end{aligned}$$

Hence,

$$\underline{Y}_1 = \underline{F} + O(\delta)O(\|\nabla \underline{F}\|), \tag{8-3}$$

and similarly

$$\nabla \underline{Y}_1 = \nabla \underline{F} + O(\delta)O(\|\nabla \nabla \underline{F}\|). \tag{8-4}$$

By the chain rule for Fréchet derivatives and (8-4),

$$\begin{aligned}\nabla \underline{\mathbf{T}}_1 &= \underline{\mathbb{K}} \bullet \nabla \underline{\mathbf{Y}}_1 \\ &= \underline{\mathbb{K}} \bullet (\nabla \underline{\mathbf{F}} + O(\delta)O(\|\nabla \nabla \underline{\mathbf{F}}\|)),\end{aligned}\tag{8-5}$$

where  $\underline{\mathbb{K}} = (\widehat{\underline{\mathbf{T}}}_1)_{\underline{\mathbf{Y}}_1}$ , that is, the Fréchet derivative of  $\widehat{\underline{\mathbf{T}}}_1$  (also known as the *micromodulus double state* [Silling 2010]). From (8-5), it is immediate that

$$O(\|\nabla \underline{\mathbf{T}}_1\|) = O(\|\nabla \underline{\mathbf{F}}\|).\tag{8-6}$$

From (8-3), (8-6), and a Taylor expansion of  $\widehat{\underline{\mathbf{T}}}_1$  near  $\underline{\mathbf{Y}}_1$ , it follows that

$$\begin{aligned}\widehat{\underline{\mathbf{T}}}_1(\underline{\mathbf{Y}}_1) &= \widehat{\underline{\mathbf{T}}}_1(\underline{\mathbf{F}}) + \underline{\mathbb{K}} \bullet (\underline{\mathbf{Y}}_1 - \underline{\mathbf{F}}) + \dots \\ &= \widehat{\underline{\mathbf{T}}}_1(\underline{\mathbf{F}}) + O(\delta)O(\|\nabla \underline{\mathbf{F}}\|) \\ &= \widehat{\underline{\mathbf{T}}}_1(\underline{\mathbf{F}}) + O(\delta)O(\|\nabla \underline{\mathbf{T}}_1\|).\end{aligned}\tag{8-7}$$

From (2-5), (6-4), and (8-7),

$$\begin{aligned}v^{\text{ps}}(\mathbf{x}) &= \int_{\mathcal{H}_1} \widehat{\underline{\mathbf{T}}}_1(\underline{\mathbf{Y}}_1[\mathbf{x}]) \langle \mathbf{n} \rangle \otimes \mathbf{n} dV_n \\ &= \int_{\mathcal{H}_1} (\widehat{\underline{\mathbf{T}}}_1(\underline{\mathbf{F}}[\mathbf{x}]) \langle \mathbf{n} \rangle + O(\delta)O(\|\nabla \underline{\mathbf{T}}_1\|)) \otimes \mathbf{n} dV_n \\ &= \int_{\mathcal{H}_1} \widehat{\underline{\mathbf{T}}}_1(\underline{\mathbf{F}}[\mathbf{x}]) \langle \mathbf{n} \rangle \otimes \mathbf{n} dV_n + O(\delta)O(\|\nabla \underline{\mathbf{T}}_1\|) \\ &= v^0(\mathbf{x}) + O(\delta)O(\|\nabla \underline{\mathbf{T}}_1\|),\end{aligned}$$

which proves (8-1).

The proof of (8-2) is similar to that of (8-1), making use of the relations  $\mathbf{L}^{\text{ps}} = \nabla \cdot v^{\text{ps}}$  and  $\mathbf{L}^0 = \nabla \cdot v^0$ .  $\square$

Since  $\widehat{\underline{\mathbf{T}}}_1$  is constant in a VSH body under a uniform deformation, (8-1) and (8-2) imply (6-5), provided the conditions of Proposition 2 are satisfied.

Comparing (7-1) with (8-1), and comparing (7-2) with (8-2), it follows that under the conditions of Proposition 2 (which are stronger than those of Proposition 1),

$$v^{\text{pd}} - v^0 = O(\delta)O(\|\nabla \underline{\mathbf{T}}_1\|) \quad \text{in } \mathcal{B},\tag{8-8}$$

$$\mathbf{L}^{\text{pd}} - \mathbf{L}^0 = O(\delta)O(\|\nabla \nabla \underline{\mathbf{T}}_1\|) \quad \text{in } \mathcal{B}.\tag{8-9}$$

This result is consistent with the conclusion in [Silling and Lehoucq 2008] that the collapsed internal force density is the “local limit of peridynamics”.

## 9. A splice between two peridynamic subregions

Let two values of horizon be denoted by  $\delta_+$  and  $\delta_-$ , and assume  $\delta_- \leq \delta_+$ . Let a reference material model  $\widehat{\underline{\mathbf{T}}}_1$  be given. Suppose, for a given deformation, two force state fields are computed everywhere using

(3-3). For any  $\mathbf{x} \in \mathcal{B}$ , define

$$\underline{\mathbf{T}}_+[\mathbf{x}](\boldsymbol{\xi}) := \frac{1}{\delta_+^{1+D}} \widehat{\mathbf{T}}_1(\underline{\mathbf{Y}}_1[\mathbf{x}]) \left\langle \frac{\boldsymbol{\xi}}{\delta_+} \right\rangle \quad \text{and} \quad \underline{\mathbf{T}}_-[\mathbf{x}](\boldsymbol{\xi}) := \frac{1}{\delta_-^{1+D}} \widehat{\mathbf{T}}_1(\underline{\mathbf{Y}}_1[\mathbf{x}]) \left\langle \frac{\boldsymbol{\xi}}{\delta_-} \right\rangle.$$

Further suppose that  $\mathcal{B}$  is divided into two disjoint subregions,  $\mathcal{B}_+$  and  $\mathcal{B}_-$ , and assume that the internal force density at any  $\mathbf{x} \in \mathcal{B}$  is given by

$$\mathbf{L}(\mathbf{x}) = \mathbf{L}^{\text{splice}}(\mathbf{x}) := \begin{cases} \int_{\mathcal{B}} \{ \underline{\mathbf{T}}_+[\mathbf{x}](\mathbf{q} - \mathbf{x}) - \underline{\mathbf{T}}_+[\mathbf{q}](\mathbf{x} - \mathbf{q}) \} dV_{\mathbf{q}} & \text{if } \mathbf{x} \in \mathcal{B}_+, \\ \int_{\mathcal{B}} \{ \underline{\mathbf{T}}_-[\mathbf{x}](\mathbf{q} - \mathbf{x}) - \underline{\mathbf{T}}_-[\mathbf{q}](\mathbf{x} - \mathbf{q}) \} dV_{\mathbf{q}} & \text{if } \mathbf{x} \in \mathcal{B}_-. \end{cases}$$

The resulting model of  $\mathcal{B}$  is called a *splice* of the subregions  $\mathcal{B}_+$  and  $\mathcal{B}_-$ .

**Remark.** A splice is not the same as a VSH body with  $\delta(\mathbf{x})$  prescribed as a step function. The difference is that in a splice, a point  $\mathbf{x}$  near the interface “sees” the force states on the other side of the interface corresponding to the same value of horizon as itself,  $\delta(\mathbf{x})$ . In contrast, in a VSH body, each point is assigned a unique value of horizon, and the force state at each point is uniquely computed according to that horizon.

In many applications, a splice provides a viable and convenient way to model a VSH body that has piecewise constant values of horizon. It is immediate that a splice model has zero internal force density under a homogeneous deformation, since the values of  $\underline{\mathbf{T}}_+$  and  $\underline{\mathbf{T}}_-$  are constant throughout  $\mathcal{B}_+$  and  $\mathcal{B}_-$ , respectively. This implies that a splice model produces no ghost forces under a uniform deformation. This is the main advantage of a splice over a VSH body. The splice is similar to an adaptivity concept for 1D bond-based peridynamics proposed by Bobaru et al. [2009] and in 2D by Bobaru and Ha [2011]. A related approach has been used in the context of atomistic-to-continuum coupling by Seleson and Gunzburger [2010].

It follows from Proposition 2 that in a splice, recalling that  $\delta_- \leq \delta_+$ ,

$$v_+^{\text{pd}} - v_-^{\text{pd}} = O(\delta_+) O(\|\nabla \underline{\mathbf{T}}_1\|) \quad \text{on } \mathcal{B}$$

and

$$\mathbf{L}_+^{\text{pd}} - \mathbf{L}_-^{\text{pd}} = O(\delta_+) O(\|\nabla \nabla \underline{\mathbf{T}}_1\|) \quad \text{on } \mathcal{B},$$

provided that the conditions of Proposition 2 are satisfied.

### 10. Local-nonlocal coupling

The situation frequently arises that we wish to model most of a body using the classical (local) theory, and only a small portion (such as in the vicinity of a growing crack) with peridynamics. A method for achieving the transition between the two is referred to as *local–nonlocal coupling*. Methods that have been proposed for local–nonlocal coupling include Arlequin [Han and Lubineau 2012], morphing [Lubineau et al. 2012; Azdoud et al. 2013; 2014], and blending [Seleson et al. 2013a; 2015]. Liu and Hong [2012] proposed a coupling method using interface elements. Methods that achieve coupling by treating peridynamic bonds as finite elements are described in [Macek and Silling 2007] and [Oterkus et al. 2012], which contains additional references. Related issues in nonlocal diffusion were investigated by Seleson, Gunzburger, and Parks [2013b]. Wu [2014] investigated a local–nonlocal coupling method

for correspondence materials in state-based peridynamics. An adaptive method for coupling peridynamic and local regions is discussed by Wildman and Gazonas [2014].

One option for local–nonlocal coupling is to use the partial stress field as a bridge between local and peridynamic subregions. In this approach,  $\mathcal{B}$  is divided into three disjoint subregions  $\mathcal{B}_0$ ,  $\mathcal{B}_{ps}$ , and  $\mathcal{B}_{pd}$ . To avoid ghost forces under a uniform deformation,  $\delta > 0$  is assumed to be constant in  $\mathcal{B}_{pd}$ . Changes in  $\delta$  occur entirely within  $\mathcal{B}_{ps}$ , such that  $\delta$  is continuous in  $\mathcal{B}$ . (Recall from (6-5) that  $\nu^{ps} \equiv \nu^0$  and  $\mathbf{L}^{ps} \equiv \mathbf{L}^0$  where  $\delta \equiv 0$ .) The internal force density is given by

$$\mathbf{L}(\mathbf{x}) = \begin{cases} \mathbf{L}^{pd}(\mathbf{x}) & \text{if } \mathbf{x} \in \mathcal{B}_{pd}, \\ \mathbf{L}^{ps}(\mathbf{x}) & \text{if } \mathbf{x} \in \mathcal{B}_{ps}, \\ \mathbf{L}^0(\mathbf{x}) & \text{if } \mathbf{x} \in \mathcal{B}_0. \end{cases} \quad (10-1)$$

The convergence properties of this method are given by (7-2) and (8-2).

Another option for local–nonlocal coupling is to use the idea of a splice described in Section 9. The body is divided into two disjoint subregions  $\mathcal{B}_0$  and  $\mathcal{B}_{pd}$  that use the local model and the full peridynamic model (constant  $\delta > 0$ ), respectively. The internal force density in the splice model is given by

$$\mathbf{L}(\mathbf{x}) = \begin{cases} \mathbf{L}^{pd}(\mathbf{x}) & \text{if } \mathbf{x} \in \mathcal{B}_{pd}, \\ \mathbf{L}^0(\mathbf{x}) & \text{if } \mathbf{x} \in \mathcal{B}_0. \end{cases} \quad (10-2)$$

The convergence properties of such a splice model are given by (8-9).

These two options for local–nonlocal coupling differ primarily in the way they transmit waves whose wavelength is smaller than or on the order of  $\delta$ . As illustrated in the example in Section 7, the transition from a local region to a nonlocal region involves a change in the dispersion properties of the material, resulting in reflections of waves. However, because the partial stress coupling method (10-1) allows a gradual change in length scale, it can be used to reduce wave reflections compared to the splice approach (10-2). As discussed in the Appendix, numerical computation of  $\mathbf{L}^{ps}$  requires the suppression of zero energy mode oscillations, similar to correspondence material models [Littlewood 2010; 2011; Breitenfeld et al. 2014]. The root cause of these oscillations is the noninvertibility of  $\nu^{\hat{ps}}(\underline{\mathbf{Y}})$ , that is, there are many possible deformations of the family that result in the same partial stress tensor.

As an example, we apply these two methods for local–nonlocal coupling to the problem of spall initiated by the impact of two brittle elastic plates. The impactor has half the thickness of the target and strikes the target from the left side. As shown in the wave diagram in Figure 5, the compressive waves that issue from the contact surface between the impactor and the target eventually intersect each other at the midplane of the target plate. When this happens, the waves, which by that time are both tensile, reinforce each other to create a thin region where the stress is strongly tensile. Within this tensile region, the strength of the material is exceeded and a crack forms. The formation of this crack creates release pulses that move in both directions. The velocity induced by the rightward-moving release pulse as it reflects from the free surface of the target bar can be measured using VISAR or other techniques [Field et al. 2004]. With the help of analysis or computational modeling, the exact characteristics of the crack release (or “pullback”) pulse can be interpreted using suitable data processing techniques to reveal the dynamic strength properties of materials under strong tension (spall).

In the computational model of this spall experiment, the impactor and target plates have thicknesses of 20 and 40, respectively. The numerical solution method is described in the Appendix. The impact

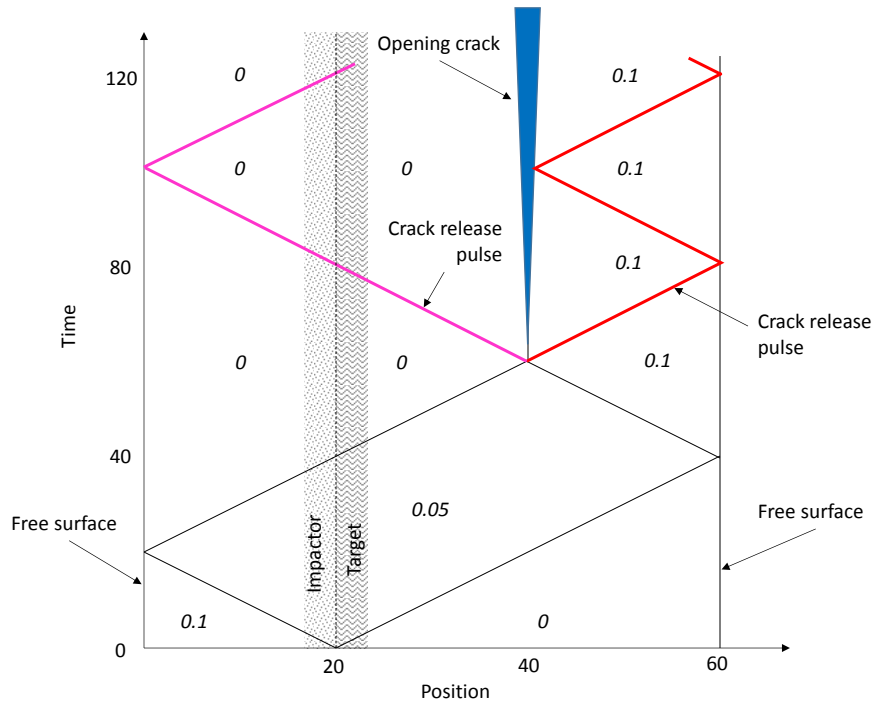


**Figure 5.** Wave diagram for the impact of a plate (from the left) on a target plate. Waves reinforce at the midplane of the target plate to cause fracture. Numbers in italics represent particle velocity.

velocity is 0.1. The elastic modulus and density of both plates are 1. The reference material model  $\hat{T}_1$  is chosen to be the bond-based prototype microelastic brittle (PMB) material model [Silling and Askari 2005] with a critical bond strain for failure of 0.04. The entire region is discretized into 1000 nodes. The objective is to model the relatively small part of the body where damage can occur using the full peridynamic equations. This peridynamic region is coupled to local regions using either of the following two methods:

- Partial stress: a peridynamic region of thickness 10, centered at the midpoint of the target plate, is enclosed by layers of thickness 4 where the partial stress method is applied. Beyond this, the local equations are used. In the peridynamic and partial stress regions, the horizon is  $\delta = 0.13$ .
- Splice: a peridynamic region of thickness 10 and horizon  $\delta = 0.13$ , centered at the midpoint of the target plate, is spliced to local regions.

For comparison, results using the full peridynamic model in the entire domain ( $\delta = 0.13$  throughout) are also computed.

The computed velocity profile at time  $t = 70$ , using the splice method for local–nonlocal coupling, is shown in Figure 6. Comparing this figure with the wave diagram in Figure 5, a number of salient features may be seen. The crack appears as a sharp jump in velocity as a function of position at  $x = 40$ .

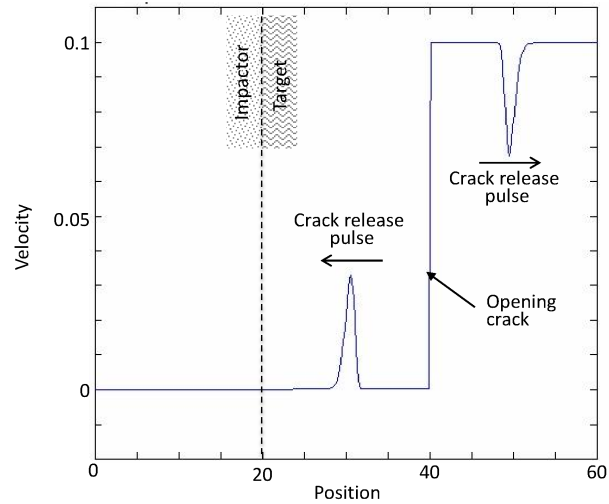


**Figure 6.** Velocity as a function of position at  $t = 70$  in the spall example problem using the splice method for local–nonlocal coupling. There are no significant artifacts from the local–nonlocal transitions, which are located at  $x = 37$  and  $x = 43$ .

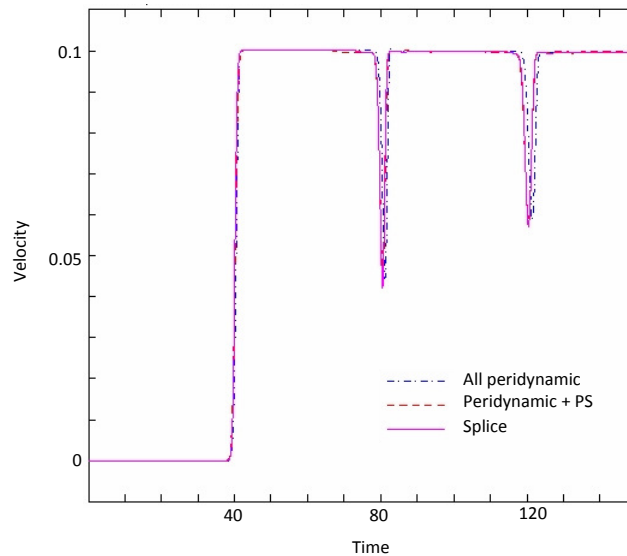


**Figure 7.** Velocity history at the free (right) surface of the target plate, showing the release pulse from the dynamic fracture occurring in the interior of the target bar. The three curves are for fully peridynamic (PD), local–nonlocal coupling using partial stress (PS), and local–nonlocal coupling using a splice.

The two release (pullback) pulses move away from the crack at the wave velocity, which is  $c = 1.0$ . In Figure 5, the particle velocities are indicated with italic numbers. The computed velocity history at the free surface is shown in Figure 7 for the two local–nonlocal coupling methods, partial stress (PS) and

splice, along with the full peridynamic model. The dips in velocity represent the crack release pulse created in the interior of the target due to spall.

As demonstrated in Figure 7, the three methods give nearly the same results in this example. However, a fully peridynamic model in multiple dimensions would require a much higher computational cost than either of the proposed local–nonlocal coupling methods, due to the large number of nonlocal interactions required to discretize the material model. So, in multiple dimensions, in problems where damage is confined to a small subregion, the splice or partial stress methods potentially offer a significant reduction in computational cost, while avoiding ghost forces. This anticipated cost reduction is a primary motivation for development of local–nonlocal coupling methods.

### 11. Discussion

In this paper, we proposed a notion of a homogeneous body (a “variable scale homogeneous” body) that characterizes a peridynamic medium with variable horizon but constant bulk material properties. We analyzed the origin and effect of ghost forces due to changes in the horizon in the full peridynamic model. The importance of these ghost forces depends on the application; they may or may not be acceptable in a computational simulation. These anomalies can be reduced by making  $\delta(\mathbf{x})$  a smoothly varying function.

If the ghost forces under a uniform deformation are not acceptable, the partial stress field can be used to effect a transition between regions with different horizons. The partial stress field appears in a modified form of the equilibrium equation. The partial stress approaches the collapsed stress in the limit of zero horizon, if the deformation is continuously differentiable. The collapsed stress,  $\hat{\nu}^0(\mathbf{F})$ , provides a material model for the first Piola–Kirchhoff stress in the local formulation.

The partial stress formulation is not thermodynamically consistent in the sense that along a cyclic loading path of a family in an elastic material, nonzero net work may appear:

$$\oint \hat{\nu}^{\text{ps}}(\underline{\mathbf{Y}}) \cdot d\mathbf{F} \neq 0. \tag{11-1}$$

(An exception to this is a uniform deformation, in which case  $\underline{\mathbf{Y}} = \underline{\mathbf{F}}$ .) The root cause of this inconsistency, which is evident in (11-1), is that the partial stress concept mixes local and nonlocal kinematics. The partial stress is therefore not suitable as a basis for a general theory of continuum mechanics. The full peridynamic theory, like the local theory, *is* thermodynamically consistent [Silling and Lehoucq 2010; Oterkus et al. 2014a; 2014b], that is,

$$\oint \hat{\mathbf{T}}(\underline{\mathbf{Y}}) \cdot d\underline{\mathbf{Y}} = 0 \quad \text{and} \quad \oint \hat{\nu}^0(\mathbf{F}) \cdot d\mathbf{F} = 0.$$

To connect subregions with constant  $\delta$  to each other, or to achieve local–nonlocal coupling, subregions can be connected using a splice. This method allows the peridynamic material model in each subregion to “see” force states in the other subregion with the same horizon as itself. The methods proposed in this paper may provide a means to reduce the computational cost of modeling a crack with peridynamics by connecting it to a larger surrounding region that is modeled with the local theory.

### Appendix: Computational details

All the numerical examples in this paper involving nonlocal models used the method described in [Silling and Askari 2005]. This method uses a midpoint quadrature rule in a Lagrangian discretization of the body. The approximation in one dimension for the peridynamic internal force density is

$$L_i^{\text{pd}} = \sum_{j \in \mathcal{F}_i} (T_{ij} - T_{ji}) V_j,$$

where  $i$  and  $j$  are node numbers,  $V_j$  is the volume of node  $j$ ,  $\mathcal{F}_i$  is the set of nodes in the material family of  $i$ , and

$$\begin{aligned} T_{ij} &= \widehat{T}(\underline{Y}[x_i], x_i) \langle x_j - x_i \rangle, & T_{ji} &= \widehat{T}(\underline{Y}[x_j], x_j) \langle x_i - x_j \rangle, \\ \underline{Y}[x_i] \langle x_j - x_i \rangle &= y_j - y_i, & \underline{Y}[x_j] \langle x_i - x_j \rangle &= y_i - y_j. \end{aligned}$$

The partial stress is computed as

$$v_i^{\text{ps}} = \sum_{j \in \mathcal{F}_i} T_{ij} (x_j - x_i) V_j.$$

The partial stress internal force density is approximated by

$$L_i^{\text{ps}} = \frac{v_{i+1}^{\text{ps}} - v_{i-1}^{\text{ps}}}{2\Delta x},$$

where  $\Delta x$  is the mesh spacing. For computations involving the PDEs of the local theory, the Piola (collapsed) stress is approximated by the finite difference formula

$$v_{i+1/2}^0 = \hat{v}^0(F_{i+1/2}) \quad \text{with} \quad F_{i+1/2} = \frac{y_{i+1} - y_i}{\Delta x}.$$

where  $\hat{v}^0$  is the material model for the Piola stress. The internal force density in the local model is approximated by

$$L_i^0 = \frac{v_{i+1/2}^0 - v_{i-1/2}^0}{\Delta x}.$$

For dynamics, time integration is performed using explicit central differencing:

$$\begin{aligned} v_i^{n+1/2} - v_i^{n-1/2} &= a_i^n \Delta t, \\ y_i^{n+1} - y_i^n &= v_i^{n+1/2} \Delta t, \end{aligned}$$

where  $\Delta t$  is the time step size. At time step  $n$ , the acceleration is computed from

$$\rho a_i^n = L_i^n + b_i^n + \eta_i^n,$$

where  $L$  is either  $L^{\text{pd}}$ ,  $L^{\text{ps}}$ , or  $L^0$ ,  $\rho$  is mass density,  $b$  is a prescribed body force density, and  $\eta$  is a linear artificial viscosity:

$$\eta_i^n = \alpha \rho c \Delta x (v_{i+1}^n - 2v_i^n + v_{i-1}^n),$$

where  $c$  is the wave speed and  $\alpha$  is a dimensionless constant on the order of 1/4. The linear artificial viscosity is effective in reducing zero energy mode oscillations that can appear due to the noninvertibility of the partial stress tensor and, when a correspondence material model is used, of the peridynamic force state. Other methods for controlling zero energy mode oscillations are described by Breitenfeld et al. [2014]



and by Littlewood [2010; 2011]. The artificial viscosity  $\eta_i^n$  is not applied if the bonds from  $i$  to  $i + 1$  or  $i$  to  $i - 1$  are damaged according to the material damage model at time step  $n$ . Otherwise, the artificial viscosity would create nonphysical forces across a crack surface.

## References

- [Azdoud et al. 2013] Y. Azdoud, F. Han, and G. Lubineau, “A morphing framework to couple non-local and local anisotropic continua”, *Int. J. Solids Struct.* **50**:9 (2013), 1332–1341.
- [Azdoud et al. 2014] Y. Azdoud, F. Han, and G. Lubineau, “The morphing method as a flexible tool for adaptive local/non-local simulation of static fracture”, *Comput. Mech.* **54**:3 (2014), 711–722.
- [Bobaru and Ha 2011] F. Bobaru and Y. Ha, “Adaptive refinement and multiscale modeling in 2D peridynamics”, *Int. J. Multiscale Comput. Eng.* **9** (2011), 707–726.
- [Bobaru et al. 2009] F. Bobaru, M. Yang, L. F. Alves, S. A. Silling, E. Askari, and J. Xu, “Convergence, adaptive refinement, and scaling in 1D peridynamics”, *Int. J. Numer. Methods Eng.* **77**:6 (2009), 852–877.
- [Breitenfeld et al. 2014] M. S. Breitenfeld, P. H. Geubelle, O. Weckner, and S. A. Silling, “Non-ordinary state-based peridynamic analysis of stationary crack problems”, *Comput. Methods Appl. Mech. Eng.* **272** (2014), 233–250.
- [Field et al. 2004] J. Field, S. Walley, W. Proud, H. Goldrein, and C. Siviour, “Review of experimental techniques for high rate deformation and shock studies”, *Int. J. Impact Eng.* **30**:7 (2004), 725–775.
- [Han and Lubineau 2012] F. Han and G. Lubineau, “Coupling of nonlocal and local continuum models by the Arlequin approach”, *Int. J. Numer. Methods Eng.* **89**:6 (2012), 671–685.
- [Lehoucq and Silling 2008] R. B. Lehoucq and S. A. Silling, “Force flux and the peridynamic stress tensor”, *J. Mech. Phys. Solids* **56**:4 (2008), 1566–1577.
- [Littlewood 2010] D. J. Littlewood, “Simulation of dynamic fracture using peridynamics, finite element modeling, and contact”, pp. 209–217 in *ASME 2010 International Mechanical Engineering Congress and Exposition* (Vancouver, 2010), 2010.
- [Littlewood 2011] D. J. Littlewood, “A nonlocal approach to modeling crack nucleation in AA 7075-T651”, pp. 567–576 in *ASME 2011 International Mechanical Engineering Congress and Exposition* (Denver, CO, 2011), 2011.
- [Liu and Hong 2012] W. Liu and J.-W. Hong, “A coupling approach of discretized peridynamics with finite element method”, *Comput. Methods Appl. Mech. Eng.* **245/246** (2012), 163–175.
- [Lubineau et al. 2012] G. Lubineau, Y. Azdoud, F. Han, C. Rey, and A. Askari, “A morphing strategy to couple non-local to local continuum mechanics”, *J. Mech. Phys. Solids* **60**:6 (2012), 1088–1102.
- [Macek and Silling 2007] R. W. Macek and S. A. Silling, “Peridynamics via finite element analysis”, *Finite Elem. Anal. Des.* **43**:15 (2007), 1169–1178.
- [Oterkus et al. 2012] E. Oterkus, E. Madenci, O. Weckner, S. Silling, P. Bogert, and A. Tessler, “Combined finite element and peridynamic analyses for predicting failure in a stiffened composite curved panel with a central slot”, *Compos. Struct.* **94**:3 (2012), 839 – 850.
- [Oterkus et al. 2014a] S. Oterkus, E. Madenci, and A. Agwai, “Fully coupled peridynamic thermomechanics”, *J. Mech. Phys. Solids* **64** (2014), 1–23.
- [Oterkus et al. 2014b] S. Oterkus, E. Madenci, and A. Agwai, “Peridynamic thermal diffusion”, *J. Comput. Phys.* **265** (2014), 71–96.
- [Seleson and Gunzburger 2010] P. Seleson and M. Gunzburger, “Bridging methods for atomistic-to-continuum coupling and their implementation”, *Commun. Comput. Phys.* **7**:4 (2010), 831–876.
- [Seleson and Parks 2011] P. Seleson and M. Parks, “On the role of the influence function in the peridynamic theory”, *Int. J. Multiscale Comput. Eng.* **9** (2011), 689–706.
- [Seleson et al. 2013a] P. Seleson, S. Beneddine, and S. Prudhomme, “A force-based coupling scheme for peridynamics and classical elasticity”, *Comput. Mater. Sci.* **66** (2013), 34–49.
- [Seleson et al. 2013b] P. Seleson, M. Gunzburger, and M. L. Parks, “Interface problems in nonlocal diffusion and sharp transitions between local and nonlocal domains”, *Comput. Methods Appl. Mech. Eng.* **266** (2013), 185–204.

- [Seleson et al. 2015] P. Seleson, Y. D. Ha, and S. Beneddine, “Concurrent coupling of bond-based peridynamics and the Navier equation of classical elasticity by blending”, *J. Multiscale Comput. Eng.* **13** (2015), 91–113.
- [Silling 2000] S. A. Silling, “Reformulation of elasticity theory for discontinuities and long-range forces”, *J. Mech. Phys. Solids* **48**:1 (2000), 175–209.
- [Silling 2010] S. A. Silling, “Linearized theory of peridynamic states”, *J. Elasticity* **99**:1 (2010), 85–111.
- [Silling and Askari 2005] S. Silling and E. Askari, “A meshfree method based on the peridynamic model of solid mechanics”, *Comput. Struct.* **83**:17-18 (2005), 1526–1535.
- [Silling and Lehoucq 2008] S. A. Silling and R. B. Lehoucq, “Convergence of peridynamics to classical elasticity theory”, *J. Elasticity* **93**:1 (2008), 13–37.
- [Silling and Lehoucq 2010] S. Silling and R. Lehoucq, “Peridynamic theory of solid mechanics”, pp. 73 – 168 in *Advances in Applied Mechanics*, vol. 44, edited by H. Aref and E. van der Giessen, Elsevier, 2010.
- [Silling et al. 2007] S. A. Silling, M. Epton, O. Weckner, J. Xu, and E. Askari, “Peridynamic states and constitutive modeling”, *J. Elasticity* **88**:2 (2007), 151–184.
- [Wildman and Gazonas 2014] R. Wildman and G. Gazonas, “A finite difference-augmented peridynamics method for reducing wave dispersion”, *Int. J. Fract.* **190**:1-2 (2014), 39–52.
- [Wu 2014] C. T. Wu, “Kinematic constraints in the state-based peridynamics with mixed local/nonlocal gradient approximations”, *Comput. Mech.* **54**:5 (2014), 1255–1267.

Received 6 Jan 2015. Accepted 21 Apr 2015.

STEWART A. SILLING: [sasilli@sandia.gov](mailto:sasilli@sandia.gov)

*Multiscale Science Department, Sandia National Laboratories, P.O. Box 5800, MS 1322, Albuquerque, NM 87185-1320, United States*

DAVID J. LITTLEWOOD: [djlittl@sandia.gov](mailto:djlittl@sandia.gov)

*Multiscale Science Department, Sandia National Laboratories, P.O. Box 5800, MS 1322, Albuquerque, NM 87185-1320, United States*

PABLO SELESON: [selesonpd@ornl.gov](mailto:selesonpd@ornl.gov)

*Computer Science and Mathematics Division, Oak Ridge National Laboratory, P.O. Box 2008, Oak Ridge, TN 37831, United States*

## A DYNAMIC ELECTRO-THERMO-MECHANICAL MODEL OF DIELECTRIC BREAKDOWN IN SOLIDS USING PERIDYNAMICS

RAYMOND A. WILDMAN AND GEORGE A. GAZONAS

The electro-thermo-mechanical breakdown of dielectric solids is modeled using peridynamics to describe the brittle fracture of a material under high electric fields. A coupled electrostatic, elastodynamic, thermodynamic model is used wherein electrostatic forces are computed and applied to the mechanical model and temperature effects are included. Fracture is simulated using peridynamics, a reformulation of elasticity that incorporates material failure. Coupling occurs between the electrostatic and mechanical forces and also the electrical material properties: specifically, the Lorentz and Kelvin forces are used to couple the electrostatic fields to the stress fields, conductivity is treated as nonlinear and a function of temperature, and mechanical damage is used to alter the permittivity. Results demonstrate that the method is capable of reproducing branching breakdown patterns seen in experiments using a deterministic method.

### 1. Introduction

Dielectric breakdown in a solid is a process involving the application of high voltage to a material, which leads to a rapid increase in the conductivity and temperature of that material, ultimately resulting in permanent material damage. In a solid material, an electromechanical breakdown process is accompanied by high temperatures, melting, vaporization, and ionization of the material, as well as physical fractures not necessarily associated with the rise in conductivity. Overall, dielectric breakdown represents a highly coupled multiphysics problem that can be challenging for numerical methods to capture.

The simulation of dielectric breakdown was first addressed with the dielectric breakdown model (DBM) or diffusion limited aggregation model [Niemeyer et al. 1984; Irurzun et al. 2002; Arshak et al. 2008]. The DBM is a stochastic method capable of reproducing the fractal patterns seen in the breakdown of various materials. Unfortunately, DBM is static and cannot reproduce breakdown velocity. Several other models are similar in nature in that they use networks of circuit components to model breakdown. These network models use fuse-like components that are destroyed when subjected to high fields [Joshi et al. 2002; Boksiner and Leath 2003; Quiña et al. 2008]. In addition to simulation methods, a simple relation between breakdown strength and a material's elastic properties can be derived, giving a rough estimate of electromechanical breakdown strength [Zebouchi and Malec 1998]. A coupled thermal/electrostatic model is given by [Noskov et al. 2001], which couples conductivity to temperature in a multiphysics model. A large field of study is focused on breakdown in thin films, in which a percolation model can be used to develop statistical characteristics [Lloyd et al. 2005; Nigam et al. 2009]. Parallels have been made between dielectric breakdown and the brittle fracture of materials under mechanical loading, leading to J-integral approaches [Beom and Kim 2008; Fan et al. 2009], a fracture energy-based approach [Schneider 2013], and a charge-free zone model [Zhang and Xie 2013]. Most

---

*Keywords:* dielectric breakdown, peridynamics, electromechanical, multiphysics.

recently, sophisticated, coupled methods have been proposed, which model the evolution of charge in gases [Chaudhury and Boeuf 2010] and liquids [Jadidian et al. 2013]. Finally, phase field modeling has been used to model the dynamic character of breakdown in a solid [Pitike and Hong 2014].

Many of the early methods discussed above are quasistatic in that they strictly dictate the breakdown velocity, though not the breakdown path. Most dynamic models are for thin films, which give accurate breakdown statistics for those geometries. The method presented here most closely resembles the coupled thermal/electrostatic model [Noskov et al. 2001], though here we extend that model through the addition of mechanical fracture. Similarly to that approach, breakdown is simulated as a change in conductivity and not using a specific breakdown field strength, such as that used in the phase field model [Pitike and Hong 2014]. The phase field approach assumes a breakdown field strength as a material property, and not as a measured quantity.

On the experimental side, dielectric breakdown can be difficult to study due to its short time scales and high energies. Despite this, several studies illustrate breakdown with high-speed photography [Yamada et al. 1990; Auckland et al. 1975; Budenstein 1980; Auckland et al. 1981]. Breakdown in solids has been studied in detail in single crystals in [Neusel et al. 2012]. In addition, the combined mechanical and electrical loading of glasses has been compared using fracture toughness, providing useful data for validating numerical schemes [Yan et al. 2010].

In the proposed approach, peridynamics will be used to simulate mechanical failure of a solid material. Peridynamics is a formulation of continuum mechanics that replaces the local divergence operators with nonlocal integral operators to facilitate fracture modeling [Silling 2000]. It has been shown to capture complex branching fracture patterns in brittle solids subjected to high mechanical loads [Ha and Bobaru 2010].

A method is proposed that uses a coupled peridynamic/finite difference method to model electromechanical breakdown in solids. The method will couple electrostatic potential, elastodynamic fields, temperature, and their constitutive models. Peridynamics is most readily discretized using a point-based scheme, compatible with finite difference methods [Wildman and Gazonas 2014], which will be used in the electrostatic simulation. In this model, thermal diffusion is ignored due to the short time scales and low thermal conductivities of the dielectrics considered, though temperature increase due to Joule heating is considered. Coupling occurs between the electrostatic forces and the elastic wave equation, the mechanical damage and the permittivity, the temperature and the conductivity, and the electric field and the conductivity [Flynn 1955; von Olshausen and Sachs 1981].

The remainder of the paper proceeds as follows: Section 2 discusses the coupled formulation including the relevant physics and discretization. Section 3 presents numerical results including homogeneous materials and materials with randomized conductivity of varying levels. Finally, Section 4 concludes the paper.

## 2. Formulation

The formulation of the coupled model is presented in this section. First, peridynamics is discussed in more detail, including its discretization and damage model. Next, the electrostatic solver is discussed, which uses a staggered grid to compute the electrostatic potential. The thermal model is then described, which only includes temperature increase due to Joule heating. Finally, the coupling of the various field equations and constitutive models is summarized.

**2.1. Peridynamics.** Peridynamics is a continuum model for brittle-elastic fracture [Silling 2000; Silling et al. 2007; Emmrich and Weckner 2006], which (in its original, bond-based form) replaces the divergence of the elastic stress tensor with an integral of a microforce function. It is characterized by a nonlocal interaction region, in that the force at a given point in space is influenced by the action at surrounding points at nonvanishing distances. The nonlocal region is governed by a specific size, or horizon, and it can be shown that for certain formulations, in the limit as this horizon approaches zero, elastodynamics is recovered [Silling and Lehoucq 2008; Lehoucq and Silling 2008]. For simplicity, a standard, bond-based peridynamics approach is used here, and summarized below.

A standard, body-force-free formulation of continuum elastodynamics (incorporating thermal expansion) can be stated as the partial differential equation

$$\rho \frac{\partial^2}{\partial t^2} \mathbf{u} = \nabla \cdot \bar{\boldsymbol{\tau}}, \quad (1)$$

where bold type with an overbar represents a second-rank tensor, the stress  $\bar{\boldsymbol{\tau}}$  is given by

$$\bar{\boldsymbol{\tau}} = \bar{\bar{\mathbf{C}}} : \bar{\boldsymbol{\varepsilon}} = \bar{\bar{\mathbf{C}}} : \left[ \frac{1}{2}(\nabla \mathbf{u} + \mathbf{u} \nabla) - \bar{\boldsymbol{\alpha}} \Delta T \right], \quad (2)$$

two overbars represent a fourth-rank tensor,  $\Delta T$  is the temperature difference relative to ambient,  $\bar{\boldsymbol{\alpha}}$  is the thermal expansion tensor, and  $\bar{\bar{\mathbf{C}}}$  is a fourth-rank constitutive tensor. In 2D plane strain, the isotropic, linear elastic constitutive tensor is given in Voigt notation by

$$\bar{\bar{\mathbf{C}}} = \begin{bmatrix} 2\mu + \lambda & \lambda & 0 \\ \lambda & 2\mu + \lambda & 0 \\ 0 & 0 & \mu \end{bmatrix}, \quad (3)$$

where Lamé's parameters  $\lambda$  and  $\mu$  are

$$\lambda = \frac{E\nu}{(1+\nu)(1-2\nu)} \quad (4)$$

and

$$\mu = \frac{E}{2(1+\nu)}, \quad (5)$$

and  $E$  is Young's modulus and  $\nu$  is Poisson's ratio.

Peridynamics proposes to replace the divergence of the stress on the right-hand side of (1) with the integral-based internal force formulation

$$\rho \frac{\partial^2}{\partial t^2} \mathbf{u} = \int_{\mathcal{H}_r} \mathbf{f}(\mathbf{u}' - \mathbf{u}, \mathbf{r}' - \mathbf{r}, T) dV', \quad (6)$$

where  $\mathcal{H}_r$  is the horizon at point  $\mathbf{r}$  and is typically spherical with radius  $\delta$  and the microforce function can be defined as

$$\mathbf{f}(\boldsymbol{\eta}, \boldsymbol{\xi}, T) = c[s(\boldsymbol{\eta}, \boldsymbol{\xi}) - \alpha \Delta T] \frac{\boldsymbol{\eta} + \boldsymbol{\xi}}{\|\boldsymbol{\eta} + \boldsymbol{\xi}\|}, \quad (7)$$

with bond stretch  $s(\boldsymbol{\eta}, \boldsymbol{\xi})$  given as

$$s(\boldsymbol{\eta}, \boldsymbol{\xi}) = \frac{\|\boldsymbol{\eta} + \boldsymbol{\xi}\| - \|\boldsymbol{\xi}\|}{\|\boldsymbol{\xi}\|}, \quad (8)$$

$c$  being a constitutive parameter, relatable to the elastic parameters as

$$c = \frac{6E}{\pi \delta^3 (1 - \nu)}. \quad (9)$$

Poisson's ratio is restricted to  $\nu = \frac{1}{3}$  for plane stress and  $\nu = \frac{1}{4}$  for plane strain [Ha and Bobaru 2010], and isotropic thermal expansion is modeled using the scalar thermal expansion coefficient  $\alpha$  and temperature (relative to ambient)  $\Delta T$  [Kilic and Madenci 2010; Oterkus and Madenci 2012; Oterkus et al. 2014].

Most importantly, peridynamics incorporates damage into its formulation by allowing for “bond-breaking” or the removal of points from horizons under high strain. The typical damage criterion is defined using the bond stretch  $s$  as

$$s - \alpha \Delta T > s_0, \quad (10)$$

where  $s_0$  can be related to the fracture energy  $G_0$  as [Ha and Bobaru 2010]

$$s_0 = \sqrt{\frac{4\pi G_0}{9E\delta}}. \quad (11)$$

If two bonds have a stretch that satisfies the inequality of (10), then those bonds are removed from each other's horizons. This approach is clearer in the discretized method, which will next be summarized.

Equation (6) is typically discretized in a pointwise fashion, wherein a domain is broken up into a regular grid and quadrature is performed with a simple midpoint rule. This approach will also be adopted here, though we will use exact quadrature weights at the edges of the horizon. In other words, where the horizon intersects with a rectangular cell, the exact area of that cell will be used, rather than the area of the entire cell as is sometimes used [Sleson 2014]. More specifically, (6) is discretized spatially as

$$\rho \frac{\partial^2}{\partial t^2} \mathbf{u}_{ij} = \sum_{m,n | \mathbf{r}_{mn} \in \mathcal{H}_{r_{ij}}}^{N_{ij}} \mathbf{f} \left( \boldsymbol{\eta}_{ij,mn}, \boldsymbol{\xi}_{ij,mn}, \frac{\Delta T_{ij} + \Delta T_{mn}}{2} \right) V_{ij,mn}, \quad (12)$$

where  $\mathbf{u}_{ij} = \mathbf{u}(\mathbf{r}_{ij})$ ,  $\boldsymbol{\xi}_{ij,mn} = \mathbf{r}_{ij} - \mathbf{r}_{mn}$ ,  $\boldsymbol{\eta}_{ij,mn} = \mathbf{u}_{ij} - \mathbf{u}_{mn}$ ,  $V_{ij,mn}$  is the area (or volume in 3D) of the  $mn$ -th node in the horizon,  $\mathcal{H}_{r_{ij}}$ , of node  $ij$ , and  $N_{ij}$  is the current number of nodes in the horizon of node  $ij$ . (In this section, the indices  $i$ ,  $j$ ,  $m$ , and  $n$  are used, though the mechanical variables will be solved on a staggered grid, offset by  $\frac{1}{2}$  in both directions. For compactness, the factor of  $\frac{1}{2}$  is dropped here. For the actual locations of all field variables, see Figure 1.) Temporal derivatives are discretized

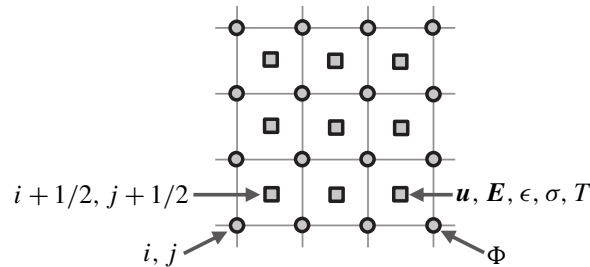


**Figure 1.** Staggered grid used for the numerical implementation, with variables labeled.

using a velocity-Verlet method, resulting in the update equations

$$\begin{aligned}
\mathbf{v}^{k+1/2} &= \mathbf{v}^k + \frac{\Delta t}{2} \mathbf{a}^k, \\
\mathbf{u}^{k+1} &= \mathbf{u}^k + \Delta t \mathbf{v}^{k+1/2}, \\
\mathbf{a}^{k+1} &= \frac{\mathbf{F}_{\text{PD}}}{\rho}, \\
\mathbf{v}^{k+1} &= \mathbf{v}^{k+1/2} + \frac{\Delta t}{2} \mathbf{a}^{k+1},
\end{aligned} \tag{13}$$

where  $\mathbf{a} = \partial^2 \mathbf{u} / \partial t^2$  is the acceleration,  $\mathbf{v} = \partial \mathbf{u} / \partial t$  is the velocity,  $\mathbf{F}_{\text{PD}}$  is the internal force given as the right-hand side of (12), and  $\Delta t$  is the time step size.

Finally, damage occurs when two nodes suffer a stretch exceeding the critical stretch (defined in (11)) and can be written in discretized form as

$$s_{ij,mn} = \frac{\|\boldsymbol{\eta}_{ij,mn} + \boldsymbol{\xi}_{ij,mn}\| - \|\boldsymbol{\xi}_{ij,mn}\|}{\|\boldsymbol{\xi}_{ij,mn}\|} - \alpha \frac{\Delta T_{ij} + \Delta T_{mn}}{2} > s_0. \tag{14}$$

In this case, any nodes satisfying the damage criterion will be removed from each other's horizons, thus decreasing  $N_{ij}$  for each. In other words, node  $mn$  will no longer contribute to the internal force of node  $ij$  in (12) (and vice versa). A damage parameter can then be defined as

$$d_{ij} = 1 - \frac{N_{ij}}{N_{ij}^{\text{initial}}}, \tag{15}$$

where  $N_{ij}^{\text{initial}}$  is the initial number of bonds in the horizon of node  $ij$ .

**2.2. Electrostatic model.** As peridynamics is most easily discretized with a particle method, a finite difference method is a natural choice for the electrostatic model. Here, the electrostatic forces will be computed beginning with the quasistatic model

$$\nabla \cdot (\sigma(T, \|\mathbf{E}\|) \nabla \Phi) + \frac{\partial}{\partial t} \nabla \cdot (\epsilon \nabla \Phi) = 0, \tag{16}$$

where  $\sigma(T, |\mathbf{E}|)$  is the conductivity and is a nonlinear function of the electric field and temperature,  $\epsilon$  is the permittivity, and  $\Phi$  is the electrostatic potential [Koch and Weiland 2011]. Note that the electrical material properties are time-varying. As stated above, (16) is a quasistatic model and can be derived by starting from either Poisson's electrostatic equation or the conservation of charge. In both cases, current density is given by Ohm's law, which has the form

$$\mathbf{J} = \sigma \mathbf{E}, \tag{17}$$

where  $\mathbf{J}$  is the current density. The quasistatic formulation used here is most appropriate for problems with finite conductivity, rather than infinite or zero as is assumed in many electrostatic problems. This formulation allows for a more accurate computation of charge and current flow, though no electromagnetic waves are generated.

In order to simplify the solution of (16), the conductivity will be linearized after temporal discretization. In other words, a Taylor series expansion will be used about the previous time step. For now, assume

that the conductivity is given by either

$$\sigma(T, \|\mathbf{E}\|) = \sigma_0 f_m(T) e^{\gamma \|\mathbf{E}\|}, \quad (18)$$

or

$$\sigma(T, \|\mathbf{E}\|) = \sigma_0 e^{\gamma \|\mathbf{E}\|} + f_a(T), \quad (19)$$

where  $\sigma_0$  is the conductivity at low temperature and field,  $f_m(T)$  and  $f_a(T)$  are some functional dependence on the temperature  $T$ , and  $\gamma$  is a parameter of the model. In addition, we assume coupling between material damage  $d$  (defined in (15)) and permittivity, modeling the formation of voids. Here, we use a linear relationship between damage and permittivity:

$$\epsilon_{ij} = \epsilon_0[\epsilon_r(1 - d_{ij}) + d_{ij}], \quad (20)$$

corresponding to a permittivity of  $\epsilon_r \epsilon_0$  when  $d_{ij} = 0$  and  $\epsilon_0$  when  $d_{ij} = 1$ , where  $\epsilon_0$  is the permittivity of free space.

This model is spatially discretized using a staggered grid for the material properties and a weak form given by

$$\oint_{\partial\Omega} \sigma \nabla \Phi \cdot \hat{\mathbf{n}} \, d\ell + \frac{\partial}{\partial t} \oint_{\partial\Omega} \epsilon \nabla \Phi \cdot \hat{\mathbf{n}} \, d\ell = 0, \quad (21)$$

where the material properties are assumed to be constant through the region  $\Omega$  enclosed by the contour  $\partial\Omega$  with unit normal  $\hat{\mathbf{n}}$ . A region  $\Omega_{ij}$  is then rectangular with side lengths  $\Delta x$  and  $\Delta y$ , centered on the point  $\mathbf{r}_{ij}$ . The electrostatic potential is then solved at each point  $\mathbf{r}_{ij}$  and denoted as  $\Phi_{ij}$ . Applying a finite difference approximation to  $\nabla \Phi$ , along with the assumption of constant material properties in each  $\Omega_{ij}$  and equal grid spacing along both  $x$  and  $y$  (i.e.,  $\Delta x = \Delta y$ ) gives the discretization

$$\nabla \cdot (a \nabla \Phi) \approx -A_0 \Phi_{ij} + A_1 \Phi_{i+1,j} + A_2 \Phi_{i,j+1} + A_3 \Phi_{i-1,j} + A_4 \Phi_{i,j-1}, \quad (22)$$

where

$$\begin{aligned} A_0 &= a_{i+1/2,j+1/2} + a_{i+1/2,j-1/2} + a_{i-1/2,j+1/2} + a_{i-1/2,j-1/2}, \\ A_1 &= \frac{1}{2}(a_{i+1/2,j+1/2} + a_{i+1/2,j-1/2}), \\ A_2 &= \frac{1}{2}(a_{i-1/2,j+1/2} + a_{i+1/2,j+1/2}), \\ A_3 &= \frac{1}{2}(a_{i-1/2,j-1/2} + a_{i-1/2,j+1/2}), \\ A_4 &= \frac{1}{2}(a_{i+1/2,j-1/2} + a_{i-1/2,j-1/2}) \end{aligned} \quad (23)$$

and  $a$  is an inhomogeneous material property.

In addition to the above discretization, we require a finite difference approximation incorporating an anisotropic material due to the linearization of the conductivity (discussed below). Generically, for anisotropic materials, the first term of (21) becomes

$$\oint_{\partial\Omega} (\bar{\mathbf{B}} \nabla \Phi) \cdot \hat{\mathbf{n}} \, d\ell, \quad (24)$$

where  $\bar{\mathbf{B}}$  is a second-rank tensor representing a generic anisotropic material property. The numerical formulation for an isotropic material can then be extended by following the same assumptions, in particular that the materials and derivative approximations are constant along each part of the contour integral.



Following this procedure leads to

$$\nabla \cdot (\bar{\mathbf{B}} \nabla \Phi) \approx -B_0 \Phi_{ij} + B_1 \Phi_{i+1,j} + B_2 \Phi_{i,j+1} + B_3 \Phi_{i-1,j} + B_4 \Phi_{i,j-1}, \quad (25)$$

where

$$B_0 = \frac{1}{2}(b_{i+1/2,j+1/2}^{xx} + b_{i+1/2,j-1/2}^{xx} + b_{i-1/2,j+1/2}^{xx} + b_{i-1/2,j-1/2}^{xx}) + \frac{1}{2}(b_{i+1/2,j+1/2}^{yy} + b_{i+1/2,j-1/2}^{yy} + b_{i-1/2,j+1/2}^{yy} + b_{i-1/2,j-1/2}^{yy}), \quad (26)$$

$$B_1 = \frac{1}{2}(b_{i+1/2,j+1/2}^{xx} + b_{i+1/2,j-1/2}^{xx}) + \frac{1}{4}(b_{i+1/2,j+1/2}^{yx} + b_{i-1/2,j+1/2}^{yx}) - \frac{1}{4}(b_{i-1/2,j-1/2}^{yx} + b_{i+1/2,j-1/2}^{yx}), \quad (27)$$

with the remaining terms  $B_2$ ,  $B_3$ , and  $B_4$  being derived similarly, and the  $b^{xx}$ ,  $b^{xy}$ ,  $b^{yx}$ , and  $b^{yy}$  are the corresponding components of  $\bar{\mathbf{B}}$ .

The spatially discretized equation can then be written as

$$D_\sigma \Phi + \frac{\partial}{\partial t} D_\epsilon \Phi = 0, \quad (28)$$

where  $D_a$  is the discretized operator defined above and  $D_\sigma$  is a nonlinear function of the potential. Because the permittivity is time-varying in this model, the above is rewritten

$$D_\sigma \Phi + D_{\partial\epsilon/\partial t} \Phi + D_\epsilon \frac{\partial}{\partial t} \Phi = 0. \quad (29)$$

An implicit backward Euler approximation can then be applied to the temporal derivatives, giving

$$(\Delta t D_{\sigma^k} + 2D_{\epsilon^k} - D_{\epsilon^{k-1}}) \Phi^k = D_{\epsilon^k} \Phi^{k-1}, \quad (30)$$

where  $\Delta t$  is the time step size. Now, the nonlinearity in the conductivity can be linearized by expanding the conductivity (given in (18) or (19)) times the electric field in a Taylor series about the field at the previous time step,  $\mathbf{E}^{k-1}$ :

$$\sigma(T^k, \|\mathbf{E}^k\|) \mathbf{E}^k \approx \sigma_0 f_m(T^k) e^{\gamma \|\mathbf{E}^{k-1}\|} \left[ \mathbf{E}^k + \gamma \frac{\mathbf{E}^{k-1} \otimes \mathbf{E}^{k-1}}{\|\mathbf{E}^{k-1}\|} (\mathbf{E}^k - \mathbf{E}^{k-1}) \right], \quad (31)$$

where  $\otimes$  denotes a tensor outer product so that the second term behaves as an anisotropic material, necessitating the use of (25)–(27). (Using the version of the conductivity given in (19) follows similarly.) Noting that  $\mathbf{E} = -\nabla \Phi$  and using the notation of (30), we find

$$(\Delta t D_{\sigma_1^k} + \Delta t D_{\sigma_2^k} + 2D_{\epsilon^k} - D_{\epsilon^{k-1}}) \Phi^k = (D_{\epsilon^k} + \Delta t D_{\sigma_2^k}) \Phi^{k-1}, \quad (32)$$

where the conductivity terms  $D_{\sigma_1^k}$  and  $D_{\sigma_2^k}$  are the discretizations of the first and second terms of the linearization in (31) as given by (22)–(23) and (25)–(27), respectively. After appropriate boundary conditions are applied, (32) can be solved at each time step for the electrostatic potential.

Next, forces can be computed from the electrostatic potential by computing the electric field,  $\mathbf{E}$ , charge density,  $q = \nabla \cdot (\epsilon \mathbf{E})$ , and polarization vector  $\mathbf{P}$  and applying the Lorentz force

$$\mathbf{F}_L = q \mathbf{E} \quad (33)$$

and the Kelvin polarization force

$$\mathbf{F}_K = \mathbf{P} \cdot \nabla \mathbf{E}, \quad (34)$$

where the polarization vector  $\mathbf{P}$  is given by

$$\mathbf{P} = (\epsilon - \epsilon_0)\mathbf{E}, \quad (35)$$

and  $\epsilon$  is the permittivity of the dielectric [Lewis 1998]. The electric field  $\mathbf{E}$  is computed from a finite difference approximation of  $\mathbf{E} = -\nabla\Phi$ , and the charge density  $q$  is computed from a finite difference approximation of Gauss's law.

Another advantage of the staggered-grid approach adopted above is that we actually require the electric field, not just the electrostatic potential. The electric field can be computed on the material grid as

$$\begin{aligned} \hat{\mathbf{x}} \cdot \mathbf{E}_{i+1/2, j+1/2} &\approx -\frac{\Phi_{i+1, j+1} - \Phi_{i, j} - \Phi_{i, j+1} + \Phi_{i+1, j}}{2\Delta x}, \\ \hat{\mathbf{y}} \cdot \mathbf{E}_{i+1/2, j+1/2} &\approx -\frac{\Phi_{i+1, j+1} - \Phi_{i, j} + \Phi_{i, j+1} - \Phi_{i+1, j}}{2\Delta y}. \end{aligned} \quad (36)$$

The advantage here is that the potential  $\Phi$  was computed on a grid offset from the grid used for the material properties and hence the peridynamic simulation. The forces needed for the peridynamic simulation must be computed by finite difference of the potential, so we can again take advantage of the offset grid and use a central difference.

These electrostatic forces are then coupled to the mechanical simulation with the equation of motion

$$\rho \frac{\partial^2}{\partial t^2} \mathbf{u} = \mathbf{F}_{PD} + \mathbf{F}_L + \mathbf{F}_K, \quad (37)$$

where  $\mathbf{F}_{PD}$  represents the mechanical forces found on the right-hand side of (12).

A simplifying assumption used here is that the mechanical displacement does not couple to the electrostatic simulation. In other words, relative motion implied by any nonzero displacement is ignored in the computation of the electrostatic potential.

**2.3. Thermal model.** Typically, the heat equation for a coupled thermomechanical problem will include terms depending on mechanical heating, diffusion, and any heat sources. Here, the thermodynamics of the model is dominated by Joule heating, so mechanical heating is ignored. Also, due to the short time scales and low thermal conductivities of most dielectric materials, thermal diffusion can be ignored. Joule heating is then defined as

$$Q = \mathbf{J} \cdot \mathbf{E}, \quad (38)$$

where  $Q$  is the power generated per unit volume due to current density  $\mathbf{J}$ . The conduction current density is then given by (17), giving

$$Q = \sigma \|\mathbf{E}\|^2. \quad (39)$$

The temperature at a point in space can be computed by summing the power at each point via

$$\frac{\partial}{\partial t} T = \frac{1}{c_p \rho} Q, \quad (40)$$

where  $c_p$  is the specific heat capacity of the material at constant pressure and  $\rho$  is again the mass density. An explicit forward Euler discretization of the above gives

$$T^{k+1} = T^k + \frac{\Delta t}{c_p \rho} Q. \quad (41)$$

The temperature is also used to alter material properties, specifically conductivity. Typically, an Arrhenius-type relation is used for temperature-conductivity coupling [Boggs and Kuang 1998; Noskov et al. 2001], which has a temperature dependency of  $\exp(-aT^{-1})$ . This type of temperature dependence can be included as an additive term to the conductivity as

$$f_a(T_{ij}) = \begin{cases} \sigma_1 e^{-\beta_1 T_{ij}^{-1}}, & T_{ij} < T_v, \\ \sigma_2 e^{-\beta_2 T_{ij}^{-1}}, & T_{ij} \geq T_v, \end{cases} \quad (42)$$

where two phases can be included depending on the temperature. The parameters  $\sigma_1$ ,  $\sigma_2$ ,  $\beta_1$ ,  $\beta_2$ , and  $T_v$  are given.

In addition, a basic exponential-type multiplicative model can be stated as [Nyberg et al. 1975]

$$f_m(T_{ij}) = \begin{cases} 1, & T_{ij} < T_m, \\ e^{\beta(T_{ij}-T_m)}, & T_m \leq T_{ij} < T_v, \\ f_{\max}, & T_{ij} \geq T_v, \end{cases} \quad (43)$$

where the coefficient  $\beta$  is given by

$$\beta = \frac{\log(f_{\max})}{T_v - T_m}. \quad (44)$$

In addition, if the temperature exceeds  $T_v$ , the conductivity is fixed at a maximum value, which will be  $\sigma = 10^6 \text{ S m}^{-1}$  throughout. In this model, the temperatures  $T_m$  and  $T_v$  may then refer to phase changes at which it may be expected that temperature influences the conductivity of the material. Temperature  $T_m$  is used to indicate the point at which the temperature begins to affect conductivity, and temperature  $T_v$  is the point at which temperature no longer influences conductivity.

Several coupled effects are ignored in the current model. Specifically, neglected but expected first- or second-order effects include the mechanical material properties dependence on temperature and the energy required to complete phase changes. Here, mechanical material properties (including the damage criterion) are not dependent on temperature while typically a material will soften as it approaches its melting point. In this model, temperatures may span all states of matter for a given material, so accurate material temperature-dependent models may be difficult to find in the literature. Also, phase changes and the energy required to complete a phase change are also ignored. A phase change from solid to liquid will of course change the governing equation of motion, though in this model, typically if the temperature rises above a certain point, enough damage has already been accumulated so that the material is not effectively behaving as a solid. Also, equations of state are not used to model gas pressure exerted on the damaged material. These effects will be considered in a future implementation. Other effects that may not be as significant include the dependence of the electrostatic potential on deformation, thermal diffusion, and the heat generated by mechanical deformation.

**2.4. Algorithm summary.** The algorithm sequence can be summarized as follows.

- (1) Specify any initial electrical material properties given by the problem geometry, and compute initial potential.
- (2) Update the displacement and velocity based on acceleration using (13).
- (3) Update the temperature using (41).
- (4) Compute the damage due to bond-breakage using condition (14) and the internal forces  $F_{PD}$ .
- (5) Update the permittivity based on the damage using (20).
- (6) Update the conductivity based on the electric field and temperature using (31).
- (7) Compute the electrostatic potential ( $\Phi$ ) from (16), with specified initial and boundary conditions.
- (8) Compute the electrostatic forces from the potential ( $F_L$  and  $F_K$ ) with (33) and (34).
- (9) Update the velocity and acceleration using the all forces  $F_{PD}$ ,  $F_L$ , and  $F_K$ .
- (10) Repeat starting at Item (2).

In addition, Figure 2 illustrates the time-stepping process: arrows indicate the dependence of variables at various points in the algorithm. The algorithm progresses to the right (increasing  $k$ ) and upward on the diagram as indicated by the arrows.

In both simulations (electrostatic and peridynamic), the spatial grid and time step size are the same, though the electrostatic potential is solved on an offset grid (see Figure 1). In this case, the time step size is governed by the requirements of the peridynamic simulation, which has a Courant-like stability condition [Silling and Askari 2005], and the accuracy of the linearization of the conductivity as given in (31). The spatial grid size is determined by the input geometry, as typically sharp features are required to produce a high electric field necessary for breakdown. Though this approach is deterministic, some random noise may be added to the electrical material properties to generate stochastic breakdown patterns.

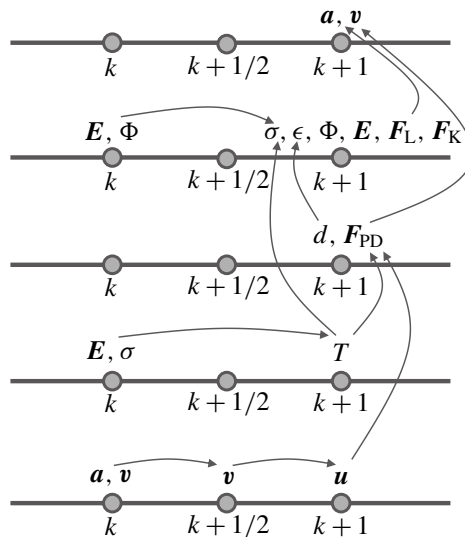


**Figure 2.** Schematic diagram of the time-stepping sequence.

|             |   |
|-------------|---|
| Mechanical: | $\rho = 2400 \text{ kg m}^{-3}$ ; $E = 72 \text{ GPa}$ ; $\delta = 0.15 \text{ mm}$ ; $G_0 = 5 \text{ J m}^{-2}$  |
| Electrical: | $\epsilon_0 = 8.85 \times 10^{-12} \text{ F m}^{-1}$ ; $\epsilon_r = 20$ ; $\sigma_0 = 10^{-19} \text{ S m}^{-1}$ |
| Thermal:    | $c_p = 800 \text{ J kg}^{-1} \text{ K}^{-1}$ ; $T_m = 500 \text{ K}$ ; $T_v = 1000 \text{ K}$                     |
| Coupled:    | $\alpha = 9 \times 10^{-6} \text{ K}^{-1}$ ; $f_{\max} = 100$ ; $\gamma = 5 \times 10^{-8} \text{ m V}^{-1}$      |

**Table 1.** Physical constants.

*Field equations.* The relevant field equations are summarized as three unknowns ( $\mathbf{u}$ ,  $\Phi$ , and  $T$ ) and the three equations

$$\rho \frac{\partial^2}{\partial t^2} \mathbf{u} = \mathbf{F}_{\text{PD}} + \mathbf{F}_{\text{L}} + \mathbf{F}_{\text{K}}, \quad (45)$$

$$\nabla \cdot (\sigma(T, \|\mathbf{E}\|) \nabla \Phi) + \frac{\partial}{\partial t} \nabla \cdot (\epsilon \nabla \Phi) = 0, \quad (46)$$

$$\frac{\partial}{\partial t} T = \frac{1}{c_p \rho} Q. \quad (47)$$

Each equation is discretized spatially using either finite differences or a grid-based mesh-free approach. Temporal discretizations are also finite difference-based, though the electrostatic equation uses backward Euler, the peridynamic equation uses velocity Verlet, and the thermodynamic equation uses forward Euler.

*Constitutive models.* The coupled constitutive models (using the multiplicative form of the temperature-conductivity coupling) are summarized as

$$\epsilon_{ij} = \epsilon_0[\epsilon_r(1 - d_{ij}) + d_{ij}], \quad (48)$$

$$\sigma_{ij}^k = \sigma_0 f_m(T_{ij}^k) e^{\gamma \|\mathbf{E}_{ij}^{k-1}\|} \left[ \mathbf{E}_{ij}^k + \gamma \frac{\mathbf{E}_{ij}^{k-1} \otimes \mathbf{E}_{ij}^{k-1}}{\|\mathbf{E}_{ij}^{k-1}\|} (\mathbf{E}_{ij}^k - \mathbf{E}_{ij}^{k-1}) \right], \quad (49)$$

$$f_m(T_{ij}) = \begin{cases} 1, & T_{ij} < T_m, \\ e^{\beta(T_{ij} - T_m)}, & T_m \leq T_{ij} < T_v, \\ f_{\max}, & T_{ij} \geq T_v. \end{cases} \quad (50)$$

In total, the permittivity depends on the damage (which depends on the mechanical deformation) and the conductivity depends on the temperature and electric field. The thermal properties (thermal conductivity and specific heat) are not coupled in this model, and neither are the mechanical properties.

*Constants.* Finally, the physical constants encompass the typical constants for the electrical, thermal, and mechanical properties, as well coupling constants needed in the constitutive models listed above. Typical values of these constants are given in Table 1 and will be used in Section 3 unless specified otherwise. The mechanical constants, thermal expansion coefficient, and heat capacity used here resemble a soda-lime glass, while the electrical and other coupling coefficients are chosen arbitrarily. Some constants, such as the coupling coefficient  $\gamma$ , can be difficult to find in the literature for many materials, so reasonable values are assumed. In addition, the effect of the temperature-conductivity coupling coefficient  $f_{\max}$  is studied below. Future work will include validation of the model with experiments.

### 3. Numerical results

Several numerical results will be presented in this section. Throughout, a point-plane geometry will be analyzed using the material properties listed in Table 1. In addition to the homogeneous material case, randomized conductivity will be demonstrated. Discretization refinement will also be explored. Finally, the effect of the temperature-conductivity coupling coefficients will be studied.

In each example, the voltage of the ground plane is fixed at 0, the point probe is held at a voltage described below, and (for simplicity) the remaining sides are treated as homogeneous Neumann boundary conditions. In each case, the voltage given ( $V_{\max}$ ) is the maximum voltage following an exponential ramp, according to

$$\Phi_{\text{probe}}(t) = V_{\max}(1 - e^{-t/\tau}), \quad (51)$$

where the time constant is  $\tau = 0.3 \mu\text{s}$  in each case.

**3.1. Uniform material properties: weak temperature dependence.** A point-plane-type geometry was simulated first with uniform material properties, wherein a point probe of length 2.5 mm and width  $150 \mu\text{m}$  was suspended above a ground plane separated by a distance of 7.5 mm. The simulation region was  $10 \text{ mm} \times 10 \text{ mm}$ . The material properties listed in Table 1 were used along with a spatial discretization of  $\Delta x = \Delta y = 50 \mu\text{m}$  and a temporal discretization of 1 ns. The simulation was run for 5000 time steps ( $5 \mu\text{s}$ ) for two different maximum voltages. First, a maximum voltage of 3 MV was used with the mechanical fracture damage shown in Figure 3, left. The electric field at the final time is shown in Figure 3, right, in units of  $\text{V m}^{-1}$ .

A maximum voltage of 4 MV was simulated next, using a spatial discretization of  $\Delta x = \Delta y = 40 \mu\text{m}$ , peridynamic horizon of  $\delta = 0.12 \text{ mm}$ , and the same temporal discretization and material properties as above. Figure 4, left, shows the damage after  $5 \mu\text{s}$ , Figure 4, right, shows the magnitude of the electric field, and Figure 5 shows the conductivity on a logarithmic scale. Clearly, the increased maximum voltage leads to higher damage in the material. Also note that, due to the weak dependence of the conductivity on temperature, the fractures observed are not associated with high conductivity. This is in contrast to typical dielectric breakdown models in which all breakdown or material damage is associated with high conductivity. Stronger dependence of conductivity on temperature is explored in a subsequent subsection.

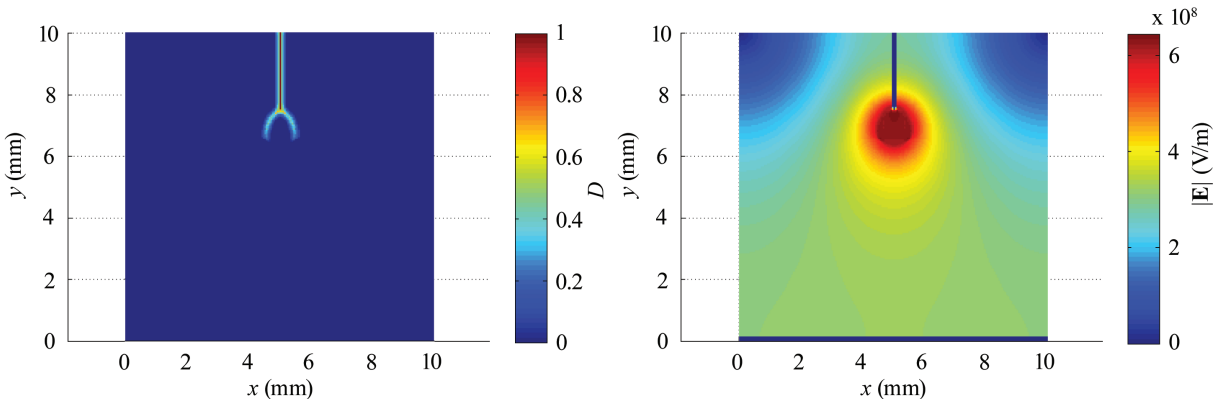


**Figure 3.** Mechanical damage including point electrode (left) and electric field (right) after  $5 \mu\text{s}$  with  $V_{\max} = 3 \text{ MV}$ .

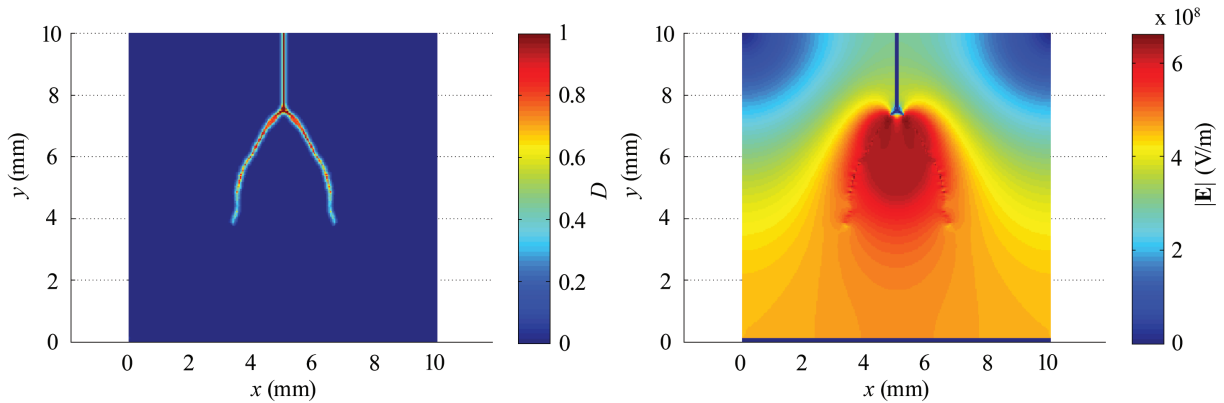


**Figure 4.** Mechanical damage including point electrode (left) and electric field (right) after  $5 \mu s$  with  $V_{max} = 4 \text{ MV}$ .

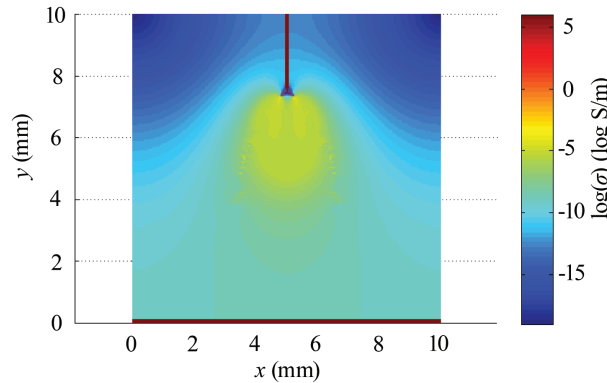


**Figure 5.** Conductivity after  $5 \mu s$  with  $V_{max} = 4 \text{ MV}$ .

**3.2. Randomized conductivity: weak temperature dependence.** A random, background conductivity will be added following a Gaussian distribution. The distribution will set the exponent of the conductivity so that the actual conductivity is exponentially related to the random distribution. More specifically, the randomized background conductivity is set as

$$\sigma_0(\mathbf{r}_{ij}) = \sigma_m + 10^{R(\sigma_m, \omega)}, \tag{52}$$

where  $\sigma_m = 10^{-19}$  is the base material’s conductivity and  $R(\mu, \omega)$  is a random variable from Gaussian distribution with mean  $\mu$  and standard deviation  $\omega$ . The standard deviation will be varied to alter the background conductivity.

First, a maximum voltage of 3 MV was simulated (using the same discretization as the 3 MV example above) with a standard deviation of  $\omega = 6$  used to alter the background conductivity. The results after  $5 \mu s$  are shown in Figure 6 (damage and conductivity). By comparison with Figure 3, left, it can be seen that the damage pattern is similar in extent, though its path is altered by the randomized conductivity.

Next, a maximum voltage of 4 MV was simulated again using the same discretization and material properties as the 4 MV above. The background conductivity was again randomized using a standard

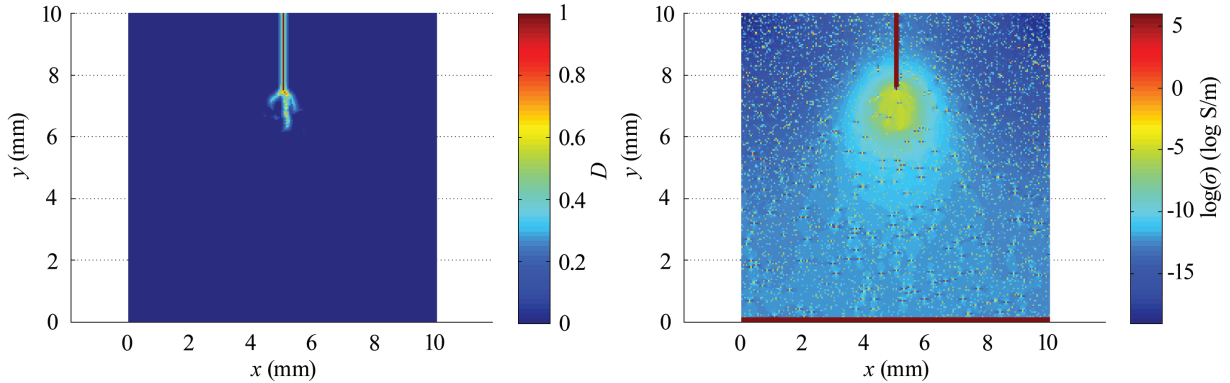


**Figure 6.** Mechanical damage including point electrode (left) and conductivity on a log scale (right) after  $5 \mu\text{s}$  with  $V_{\text{max}} = 3 \text{ MV}$  with randomized background conductivity.

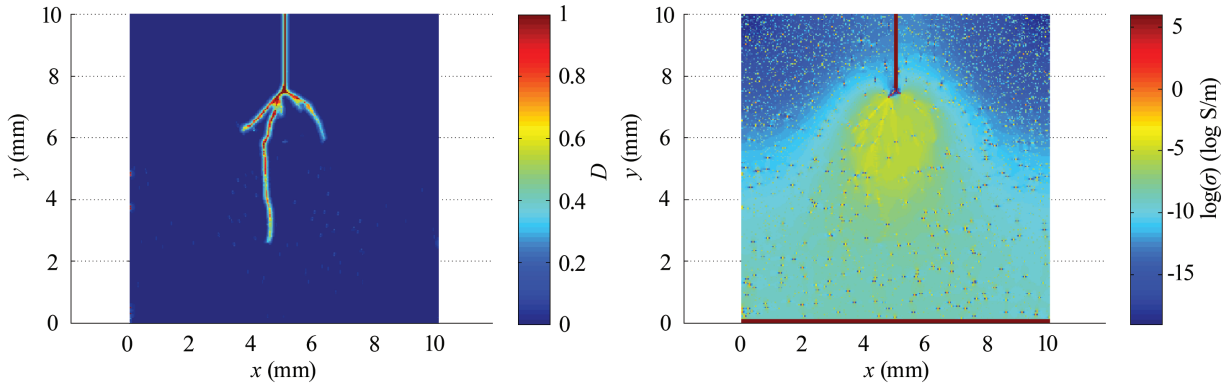


**Figure 7.** Mechanical damage including point electrode (left) and conductivity on a log scale (right) after  $5 \mu\text{s}$  with  $V_{\text{max}} = 4 \text{ MV}$  with randomized background conductivity.

deviation of  $\omega = 6$ , though the actual distribution of conductivity is not the same as the above example. In other words, the conductivity was generated using a different seed for the random number generator. Figure 7 shows the damage after  $5 \mu\text{s}$  (left) and the conductivity on a logarithmic scale (right).

**3.3. Discretization refinement.** The above test with a maximum voltage of  $4 \text{ MV}$  was repeated, though now with a time step size of  $\Delta t = 0.5 \text{ ns}$ . The resulting damage is shown in Figure 8, left. As can be seen by comparing with Figure 4, left, the damage pattern is stable between the two time step sizes.

Next, the breakdown simulation was run with a spatial discretization of  $\Delta x = \Delta y = 33.33 \mu\text{m}$ , a peridynamic horizon of  $\delta = 0.1 \text{ mm}$ , and a time step size of  $\Delta t = 1 \text{ ns}$ . In this case, the width of the point probe had to be reduced to  $100 \mu\text{m}$  to conform to the computational grid. Nevertheless, the results show a stable fracture pattern (Figure 8, right) compared with the coarse discretization.

**3.4. Strong temperature dependence.** Due to positive feedback, increasing the temperature-conductivity coupling coefficient ( $f_{\text{max}}$  or  $\beta$ ) leads to much higher temperatures than those seen in the previous examples. The model is not formulated to couple temperature to all relevant material properties (e.g.,



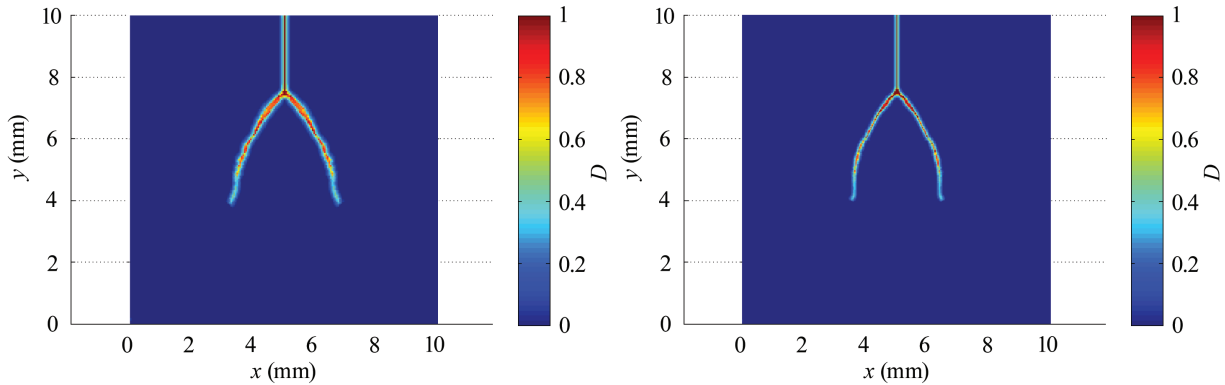


**Figure 8.** Mechanical damage including point electrode after  $5 \mu\text{s}$  with  $V_{\text{max}} = 4 \text{ MV}$  using a time step size of  $\Delta t = 0.5 \text{ ns}$  (left) and using a spatial step size of  $\Delta x = \Delta y = 33.33 \mu\text{m}$  (right).

mechanical properties), so a first approach is to limit the maximum Joule heating power allowed in the simulation. In this section, a maximum heating power of  $Q = 10^{16} \text{ W}$  is used. An immediate effect seen if higher temperatures are allowed is that the thermal expansion can lead to rapid degradation of the material and instability in the simulation.

In this example, the temperature-conductivity coupling coefficient was raised to  $f_{\text{max}} = 10^6$ . Uniform material properties were used with the coarse discretization in both space and time of the 4 MV example above. A maximum voltage of 4 MV was simulated, giving the damage seen in Figure 9. With the increased coupling coefficient, the damage pattern has changed and now has an additional branch originating at the ground plane.

**3.5. Additive temperature-conductivity model.** Finally, the additive form (see (42)) of the temperature-conductivity coupling is tested. The parameters used are transition temperature  $T_v = 1000 \text{ K}$ , base conductivities of  $\sigma_1 = 10^4 \text{ S m}^{-1}$  and  $\sigma_2 = 3 \times 10^4 \text{ S m}^{-1}$ , and exponents of  $\beta_1 = 1.2 \times 10^4 \text{ K}^{-1}$  and

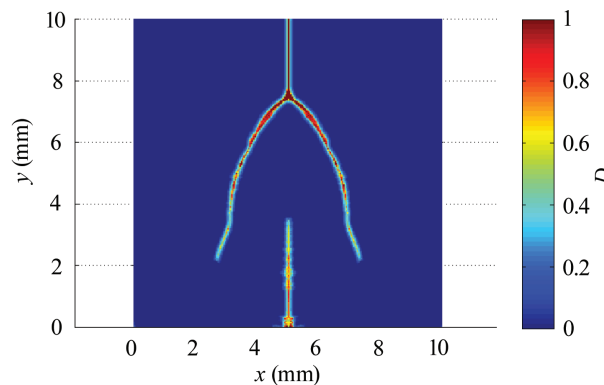


**Figure 9.** Mechanical damage including point electrode after  $5 \mu\text{s}$  with  $V_{\text{max}} = 4 \text{ MV}$  using a temperature-conductivity coupling coefficient of  $f_{\text{max}} = 10^6$ .

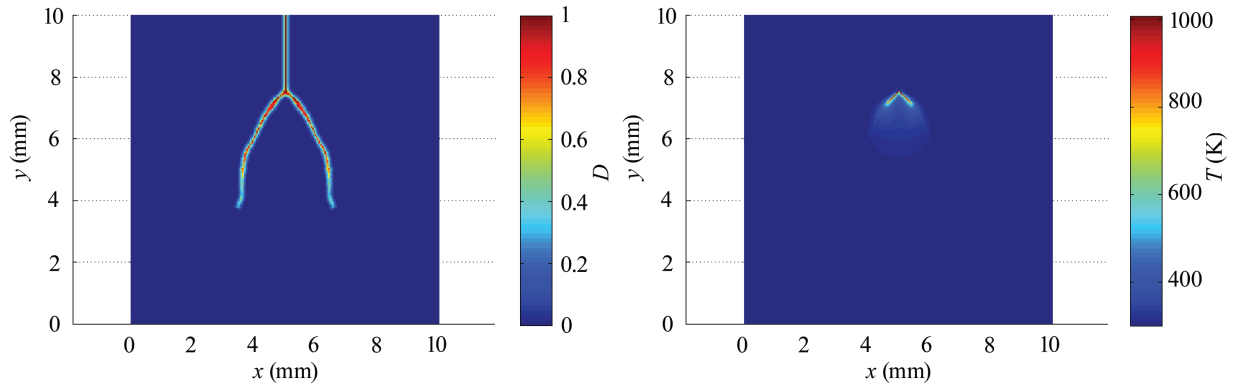


**Figure 10.** Mechanical damage including point electrode (left) and temperature distribution (right) after  $5 \mu\text{s}$  with  $V_{\text{max}} = 4 \text{ MV}$  using the additive temperature-conductivity coupling model.

$\beta_2 = 1.2 \times 10^3 \text{ K}^{-1}$ . The simulation was run with both a maximum voltage of 3 MV and 4 MV. With a maximum voltage of 3 MV and 4 MV, the resulting damage was similar to that given above for the weak temperature dependence. The damage after  $5 \mu\text{s}$  for a maximum voltage of 4 MV is shown in Figure 10, left. The temperature after  $5 \mu\text{s}$  is shown in Figure 10, right, illustrating that, while there is mechanical fracture in the material, a highly conductive region has not propagated completely through the material.

#### 4. Conclusions

A coupled electrostatic, thermodynamic, elastodynamic model of dielectric breakdown in solids was presented. The method uses a finite difference solver to compute the electrostatic potential due to an applied voltage. The Lorentz and Kelvin forces couple the electric field to the mechanical forces, thus generating stress in the solid. Peridynamics is used to then simulate the mechanical fracture of the material due to high strains. The electrical permittivity is coupled to the damage, and a nonlinear conductivity is used to model the effects of high electric fields. Finally, temperature is considered in the model using Joule heating as the heat source, and thermal expansion and temperature effects on the electrical conductivity are considered. Results show mechanical fracture patterns consistent with those seen in brittle solids undergoing dielectric breakdown. In addition, discretization refinement was performed and shows that the proposed method generates stable fracture patterns. Several additions to the model are possible, for example, coupling of temperature to mechanical material properties, deformation to electrostatic potential, and more realistic phase changes.

#### References

- [Arshak et al. 2008] K. Arshak, I. Guiney, and E. Forde, “Material dependent dielectric breakdown model”, *Comp. Mater. Sci.* **42**:3 (2008), 483–488.
- [Auckland et al. 1975] D. W. Auckland, A. B. Borishade, and N. Gravill, “A self triggered high speed camera for the photography of prebreakdown luminescence in solid dielectrics”, *J. Phys. E Sci. Instrum.* **8**:10 (1975), 847–849.
- [Auckland et al. 1981] D. W. Auckland, R. Cooper, and J. Sanghera, “Photographic investigation of formative stage of electric breakdown in diverging fields”, *IEE Proc. A* **128**:3 (1981), 209–214.

- [Beom and Kim 2008] H. G. Beom and Y. H. Kim, "Application of  $J$  integral to breakdown analysis of a dielectric material", *Int. J. Solids Struct.* **45**:24 (2008), 6045–6055.
- [Boggs and Kuang 1998] S. Boggs and J. Kuang, "High field effects in solid dielectrics", *IEEE Electr. Insul. M.* **14**:6 (1998), 5–12.
- [Boksiner and Leath 2003] J. Boksiner and P. L. Leath, "Dynamics of dielectric breakdown paths", *Phys. Rev. E* **67**:6 (2003), 066610.
- [Budenstein 1980] P. P. Budenstein, "On the mechanism of dielectric breakdown of solids", *IEEE T. Electr. Insul.* **15**:3 (1980), 225–240.
- [Chaudhury and Boeuf 2010] B. Chaudhury and J.-P. Boeuf, "Computational studies of filamentary pattern formation in a high power microwave breakdown generated air plasma", *IEEE T. Plasma Sci.* **38**:9 (2010), 2281–2288.
- [Emmrich and Weckner 2006] E. Emmrich and O. Weckner, "The peridynamic model in non-local elasticity theory", *P. Appl. Math. Mech.* **6**:1 (2006), 155–156.
- [Fan et al. 2009] C.-Y. Fan, M.-H. Zhao, and Y.-H. Zhou, "Numerical solution of polarization saturation/dielectric breakdown model in 2D finite piezoelectric media", *J. Mech. Phys. Solids* **57**:9 (2009), 1527–1544.
- [Flynn 1955] P. T. G. Flynn, "Field-dependent conductivity in non-uniform fields and its relation to electrical breakdown", *P. IEE C Monogr.* **102**:2 (1955), 264–269.
- [Ha and Bobaru 2010] Y. D. Ha and F. Bobaru, "Studies of dynamic crack propagation and crack branching with peridynamics", *Int. J. Fracture* **162**:1–2 (2010), 229–244.
- [Iruzun et al. 2002] I. M. Iruzun, P. Bergero, V. Mola, M. C. Cordero, J. L. Vicente, and E. E. Mola, "Dielectric breakdown in solids modeled by DBM and DLA", *Chaos Soliton. Fract.* **13**:6 (2002), 1333–1343.
- [Jadidian et al. 2013] J. Jadidian, M. Zahn, N. Lavesson, O. Widlund, and K. Borg, "Stochastic and deterministic causes of streamer branching in liquid dielectrics", *J. Appl. Phys.* **114**:6 (2013), 063301.
- [Joshi et al. 2002] R. P. Joshi, J. Qian, and K. H. Schoenbach, "Electrical network-based time-dependent model of electrical breakdown in water", *J. Appl. Phys.* **92**:10 (2002), 6245–6251.
- [Kilic and Madenci 2010] B. Kilic and E. Madenci, "Peridynamic theory for thermomechanical analysis", *IEEE T. Adv. Pack-aging* **33**:1 (2010), 97–105.
- [Koch and Weiland 2011] S. Koch and T. Weiland, "Different types of quasistationary formulations for time domain simulations", *Radio Sci.* **46**:5 (2011), 1–7.
- [Lehoucq and Silling 2008] R. B. Lehoucq and S. A. Silling, "Force flux and the peridynamic stress tensor", *J. Mech. Phys. Solids* **56**:4 (2008), 1566–1577.
- [Lewis 1998] T. J. Lewis, "A new model for the primary process of electrical breakdown in liquids", *IEEE T. Dielect. El. In.* **5**:3 (1998), 306–315.
- [Lloyd et al. 2005] J. R. Lloyd, E. Liniger, and T. M. Shaw, "Simple model for time-dependent dielectric breakdown in inter- and intralevel low- $k$  dielectrics", *J. Appl. Phys.* **98**:8 (2005), 084109.
- [Neusel et al. 2012] C. Neusel, H. Jelitto, D. Schmidt, R. Janssen, F. Felten, and G. A. Schneider, "Dielectric breakdown of alumina single crystals", *J. Eur. Ceram. Soc.* **32**:5 (2012), 1053–1057.
- [Niemeyer et al. 1984] L. Niemeyer, L. Pietronero, and H. J. Wiesmann, "Fractal dimension of dielectric breakdown", *Phys. Rev. Lett.* **52**:12 (1984), 1033–1036.
- [Nigam et al. 2009] T. Nigam, A. Kerber, and P. Peumans, "Accurate model for time-dependent dielectric breakdown of high- $k$  metal gate stacks", pp. 523–530 in *2009 IEEE International Reliability Physics Symposium* (Montréal, 2009), Inst. El. Electr. Eng., Piscataway, NJ, 2009.
- [Noskov et al. 2001] M. Noskov, V. Lopatin, A. Cheglov, and A. Shapovalov, "Computer simulation of discharge channel propagation in solid dielectric", pp. 465–468 in *Proceedings of the 2001 IEEE 7th International Conference on Solid Dielectrics* (Eindhoven, Netherlands, 2001), Inst. El. Electr. Eng., Piscataway, NJ, 2001.
- [Nyberg et al. 1975] B. R. Nyberg, K. Herstad, and K. Bjorlow-Larsen, "Numerical methods for calculation of electrical stresses in HVDC cables with special application to the Skagerrak cable", *IEEE T. Power. Ap. Syst.* **94**:2 (1975), 491–497.

- [von Olshausen and Sachs 1981] R. von Olshausen and G. Sachs, “AC loss and DC conduction mechanisms in polyethylene under high electric fields”, *IEE Proc. A* **128**:3 (1981), 183–192.
- [Oterkus and Madenci 2012] E. Oterkus and E. Madenci, “Peridynamic analysis of fiber-reinforced composite materials”, *J. Mech. Mater. Struct.* **7**:1 (2012), 45–84.
- [Oterkus et al. 2014] S. Oterkus, E. Madenci, and A. Agwai, “Fully coupled peridynamic thermomechanics”, *J. Mech. Phys. Solids* **64** (2014), 1–23.
- [Pitike and Hong 2014] K. C. Pitike and W. Hong, “Phase-field model for dielectric breakdown in solids”, *J. Appl. Phys.* **115**:4 (2014), 044101.
- [Quiña et al. 2008] P. L. D. Quiña, L. Herrera, I. M. Irurzun, and E. E. Mola, “A capacitive model for dielectric breakdown in polymer materials”, *Comp. Mater. Sci* **44**:2 (2008), 330–338.
- [Schneider 2013] G. A. Schneider, “A Griffith type energy release rate model for dielectric breakdown under space charge limited conductivity”, *J. Mech. Phys. Solids* **61**:1 (2013), 78–90.
- [Seleson 2014] P. Seleson, “Improved one-point quadrature algorithms for two-dimensional peridynamic models based on analytical calculations”, *Comput. Methods Appl. Mech. Engrg.* **282** (2014), 184–217.
- [Silling 2000] S. A. Silling, “Reformulation of elasticity theory for discontinuities and long-range forces”, *J. Mech. Phys. Solids* **48**:1 (2000), 175–209.
- [Silling and Askari 2005] S. A. Silling and E. Askari, “A meshfree method based on the peridynamic model of solid mechanics”, *Comput. Struct.* **83**:17–18 (2005), 1526–1535.
- [Silling and Lehoucq 2008] S. A. Silling and R. B. Lehoucq, “Convergence of peridynamics to classical elasticity theory”, *J. Elasticity* **93**:1 (2008), 13–37.
- [Silling et al. 2007] S. A. Silling, M. Epton, O. Weckner, J. Xu, and E. Askari, “Peridynamic states and constitutive modeling”, *J. Elasticity* **88**:2 (2007), 151–184.
- [Wildman and Gazonas 2014] R. A. Wildman and G. A. Gazonas, “A finite difference-augmented peridynamics method for reducing wave dispersion”, *Int. J. Fracture* **190**:1–2 (2014), 39–52.
- [Yamada et al. 1990] H. Yamada, T. Sato, and T. Fujiwara, “High-speed photography of prebreakdown phenomena in dielectric liquids under highly non-uniform field conditions”, *J. Phys. D Appl. Phys.* **23**:12 (1990), 1715–1722.
- [Yan et al. 2010] D.-J. Yan, H.-Y. Huang, C.-W. Cheung, and T.-Y. Zhang, “Fracture criterion for conductive cracks in soda-lime glass under combined mechanical and electrical loading”, *Int. J. Fracture* **164**:2 (2010), 185–199.
- [Zebouchi and Malec 1998] N. Zebouchi and D. Malec, “Combination of thermal and electromechanical breakdown mechanisms to analyze the dielectric breakdown in polyethylene terephthalate”, *J. Appl. Phys.* **83**:11 (1998), 6190–6192.
- [Zhang and Xie 2013] T.-Y. Zhang and T. Xie, “The charge-free zone model for electrically conductive cracks in dielectric and piezoelectric ceramics”, *Acta Mech.* **224**:6 (2013), 1159–1168.

Received 15 Apr 2015. Revised 29 Sep 2015. Accepted 19 Oct 2015.

RAYMOND A. WILDMAN: raymond.a.wildman.civ@mail.mil

Weapons and Materials Research Directorate, U.S. Army Research Laboratory, Aberdeen Proving Ground, MD 21005, United States

GEORGE A. GAZONAS: george.a.gazonas.civ@mail.mil

Weapons and Materials Research Directorate, U.S. Army Research Laboratory, Aberdeen Proving Ground, MD 21005, United States

## SUBMISSION GUIDELINES

### ORIGINALITY

Authors may submit manuscripts in PDF format online at the Submissions page. Submission of a manuscript acknowledges that the manuscript is original and has neither previously, nor simultaneously, in whole or in part, been submitted elsewhere. Information regarding the preparation of manuscripts is provided below. Correspondence by email is requested for convenience and speed. For further information, write to [contact@msp.org](mailto:contact@msp.org).

### LANGUAGE

Manuscripts must be in English. A brief abstract of about 150 words or less must be included. The abstract should be self-contained and not make any reference to the bibliography. Also required are keywords and subject classification for the article, and, for each author, postal address, affiliation (if appropriate), and email address if available. A home-page URL is optional.

### FORMAT

Authors can use their preferred manuscript-preparation software, including for example Microsoft Word or any variant of  $\text{\TeX}$ . The journal itself is produced in  $\text{\LaTeX}$ , so accepted articles prepared using other software will be converted to  $\text{\LaTeX}$  at production time. Authors wishing to prepare their document in  $\text{\LaTeX}$  can follow the example file at [www.jomms.net](http://www.jomms.net) (but the use of other class files is acceptable). At submission time only a PDF file is required. After acceptance, authors must submit all source material (see especially Figures below).

### REFERENCES

Bibliographical references should be complete, including article titles and page ranges. All references in the bibliography should be cited in the text. The use of  $\text{\BibTeX}$  is preferred but not required. Tags will be converted to the house format (see a current issue for examples); however, for submission you may use the format of your choice. Links will be provided to all literature with known web locations; authors can supply their own links in addition to those provided by the editorial process.

### FIGURES

Figures must be of publication quality. After acceptance, you will need to submit the original source files in vector format for all diagrams and graphs in your manuscript: vector EPS or vector PDF files are the most useful. (EPS stands for Encapsulated PostScript.)

Most drawing and graphing packages—Mathematica, Adobe Illustrator, Corel Draw, MATLAB, etc.—allow the user to save files in one of these formats. Make sure that what you're saving is vector graphics and not a bitmap. If you need help, please write to [graphics@msp.org](mailto:graphics@msp.org) with as many details as you can about how your graphics were generated.

Please also include the original data for any plots. This is particularly important if you are unable to save Excel-generated plots in vector format. Saving them as bitmaps is not useful; please send the Excel (.xls) spreadsheets instead. Bundle your figure files into a single archive (using zip, tar, rar or other format of your choice) and upload on the link you been given at acceptance time.

Each figure should be captioned and numbered so that it can float. Small figures occupying no more than three lines of vertical space can be kept in the text (“the curve looks like this:”). It is acceptable to submit a manuscript with all figures at the end, if their placement is specified in the text by means of comments such as “Place Figure 1 here”. The same considerations apply to tables.

### WHITE SPACE

Forced line breaks or page breaks should not be inserted in the document. There is no point in your trying to optimize line and page breaks in the original manuscript. The manuscript will be reformatted to use the journal's preferred fonts and layout.

### PROOFS

Page proofs will be made available to authors (or to the designated corresponding author) at a Web site in PDF format. Failure to acknowledge the receipt of proofs or to return corrections within the requested deadline may cause publication to be postponed.

